UCGE Reports

Number 20338

**Department of Geomatics Engineering**

Spatial Characterization of Multipath GNSS Channel
**(URL: http://www.geomatics.ucalgary.ca/graduatetheses)**

**by**

**Mohammed Hatef Keshvadi**

September 2011

SCHULICH
School of Engineering    UNIVERSITY OF CALGARY

UNIVERSITY OF CALGARY

# SPATIAL CHARACTERIZATION OF MULTIPATH

# GNSS CHANNEL

by

Mohammad Hatef Keshvadi

A THESIS

SUBMITTED TO THE FACULTY OF GRADUATE STUDIES

IN PARTIAL FULFILMENT OF THE REQUIREMENTS FOR THE

DEGREE OF MASTER OF SCIENCE

DEPARTMENT OF GEOMATICS ENGINEERING

CALGARY, ALBERTA

SEPTEMBER, 2011

**Abstract**

In addition to conventional applications of Global Navigation Satellite Systems (GNSS), an intense effort is focused on increasing receiver signal detection and tracking capabilities in shaded areas. While many solutions have been proposed to enhance the performance of receivers to overcome these effects, it is still vital to characterize the GNSS channel under multipath. The main focus of the research presented herein is to measure different characteristics of the multipath GNSS channel, including the fading model, signal level variations, angle of arrival (AoA) and correlation coefficient. This is done through the implementation of synthetic array techniques that have been used in other applications such as radar and wireless telecommunications for decades.

A primary use of antenna arrays is to estimate the AoA of incoming signals and measure the angular spread (AS) of the channel. Another application for wireless navigation, called beamforming, is to mitigate the multipath and other RF interference by steering the beam towards the desired signal direction. Therefore, assessing the performance of beamforming under multipath conditions is another key objective of this research. To characterize the multipath GNSS channel in real world situations, large GPS data sets were collected under different conditions. The measurement results show the close relationship between the AS, the fading model and the achieved array gain as a performance measure of beamforming.

## Acknowledgements

**Dedication**

To my parents, Mitra and Ahmad, who taught me the value of knowledge, to my patient

wife, Afrand, for her love and support and to my brother Soroush.

# Table of Contents

# List of Tables

## List of Figures and Illustrations

xiii

**List of Symbols, Abbreviations and Nomenclature**

| Symbol | Definition |
|---|---|
| $a$ | Signal amplitude |
| $\mathbf{a}$ | Unit vector along LoS |
| $A$ | Complex channel response |
| $AF$ | Array factor |
| $AG$ | Array gain |
| $AS$ | Angular spread |
| $b$ | Beamforming output |
| $c$ | Speed of Light |
| $c_i[\ ]$ | Delayed PRN code |
| $\tilde{C}$ | Carrier Power |
| $\mathbf{C_s}$ | Samples correlation matrix |
| $CN(.,.)$ | Circularly normal distribution |
| $D[.]$ | Data-bit |
| $\hat{e}_T$ | Normalized polarization phase vector |
| $f$ | Frequency |
| $f_d$ | Doppler frequency |
| $f_{IF}$ | Intermediate frequency |
| $f_{Rx}$ | Received frequency |
| $f_S$ | Sampling frequency |
| $f_{Tx}$ | Transmission frequency |
| $h$ | Filter time response |
| $I$ | In-phase component |
| $I_0$ | Modified Bessel function of $0^{th}$ order and the $1^{st}$ kind |
| $J_0$ | Bessel function of $0^{th}$ order and the $1^{st}$ kind |
| $k_0$ | The normalized distance with respect to the wavelength |
| $K$ | Total number of array samples, Number of satellites in view |
| $\mathbf{k}$ | Wave number vector |
| $m$ | Time index of discrete samples |
| $M$ | Number of elements in an array |
| $n$ | Time index of discrete samples |
| $N(.,.)$ | Normal (Gaussian) distribution |
| $N_0$ | Noise level |
| $\mathbf{p}$ | Position vector of array elements |
| $p$ | Probability density function |
| $\boldsymbol{p}$ | Joint probability density function |
| $P$ | Probability Density Function |
| $Q$ | Quadrature component |
| $r$ | Pre-correlation signal |

| | |
|---|---|
| $\mathbf{R}$ | Covariance matrix of array response vector |
| $R$ | Radius of UCA |
| $\tilde{R}$ | Auto Correlation Function |
| $R_c$ | Chipping Rate |
| $s$ | signal |
| $s_I$ | In-phase component of signal |
| $s_l$ | Low-pass representation of signal |
| $s_Q$ | Quadraphase component of signal |
| $S$ | Post-correlation signal |
| $\hat{\mathbf{S}}_{\mathbf{K}}$ | Total samples matrix |
| $t$ | time |
| T | Time |
| $T_c$ | Chipping Time |
| $T_{coh}$ | Coherent Integration Time |
| $T_S$ | Sampling time |
| $v$ | velocity |
| $\mathbf{v}$ | Array manifold vector, steering vector |
| $\mathbf{V}$ | Noise subspace eigenvector |
| $w$ | Weighting function |
| $\mathbf{w}$ | Complex gain vector |
| $x$ | Arbitrary variable |
| $\hat{x}'$ | Unit vector along Transmitter cross dipole |
| $\hat{y}'$ | Unit vector along Transmitter cross dipole |
| Y | Element gain pattern |
| | |
| $\alpha$ | Polarization state |
| $\beta$ | Polarization state |
| $\beta_i$ | Array gain pattern phase factor |
| $\delta$ | Impulse input |
| $\phi$ | Azimuth angle |
| $\varphi$ | Post-correlation phase of the signal |
| $\gamma$ | Angular distance |
| $\dot{\gamma}$ | Antenna/UCA rotation rate |
| $\eta$ | noise |
| $\lambda$ | wavelength |
| $\lambda$ | eigenvector |
| $\theta$ | Polar angle |
| $\tilde{\theta}$ | Elevation angle |
| $\theta_s$ | Angle spread along elevation |
| $\tau$ | Delay between signals |
| $\omega$ | Angular velocity |
| $\Psi$ | Power Spectral Density |

| | |
|---|---|
| $\psi$ | Carrier phase |
| $\Omega$ | Antenna/UCA rotation rate |

| | |
|---|---|
| **ACF** | Autocorrelation Function |
| **AIC** | Akaike Information criterion |
| **AG** | Array Gain |
| **AoA** | Angle of Arrival |
| **AS** | Angular Spread |
| **AWGN** | Additive White Gaussian Noise |
| **Az** | Azimuth |
| **BS** | Beam Scan |
| **CAF** | Cross Ambiguity Function |
| **CDMA** | Code Division Multiple Access |
| **DLL** | Delay Lock Loop |
| **DS-SS** | Direct Sequence Spread Spectrum |
| **EEEL** | Energy, Environment Experimental Learning building |
| **El** | Elevation |
| **ES** | Earth Science building |
| **ESPRIT** | Estimation of Signal Parameters via Rotational Invariance Techniques |
| **FLL** | Frequency Lock Loop |
| **GNSS** | Global Navigation Satellite system |
| **GPS** | Global Positioning System |
| **HSGPS** | High-Sensitivity GPS |
| **ICT** | Information and Communication Technology building |
| **INS** | Inertial Navigation System |
| **IMU** | Inertial Measurement Unit |
| **LoS** | Line of Sight |
| **MVDR** | Minimum Variance Distortionless Response |
| **MPC** | MultiPath Components |
| **MUSIC** | Multiple Signal Classification |
| **NI** | National Instruments |
| **NLoS** | None-Line of sight |
| **PDF** | Probability Density function |
| **PLL** | Phase Lock Loop |
| **PRN** | Pseudo-Random Noise |
| **RHCP** | Right Hand Circularly Polarized |
| **SNR** | Signal to Noise Ratio |
| **SV** | Space Vehicle |
| **ToA** | Time of Arrival |
| **MVDR** | Minimum Variance Distortionless Response |
| **UCA** | Uniform circular Array |
| **U of C** | University of Calgary |
| **UWB** | Ultra-Wide Band |

**Chapter One: Introduction**

Since 1978 when the first prototype satellite of the GPS constellation was launched into space, GNSS receivers have evolved drastically to become so accurate that they provide the user's position within the metre level accuracy, and also they have become so light, compact and low cost that they are being integrated into common hand held devices such as cell phones, personal music players and digital cameras.

Beyond conventional applications of GNSS systems, intense attention has been paid to expanding GNSS signal detection and tracking indoors, in urban canyons and other shaded areas where GNSS signals are extremely weak. Examples of indoor navigation applications for GNSS include locating distress calls from victims of medical emergencies, crime detection, and during natural disasters such as earthquakes. Of course other applications include commercial purposes such as smart advertisement as well as security and intelligence usages.

A typical GNSS receiver must be able to track the code, frequency and phase of a signal that has undergone many degrading effects such as those caused by atmospheric delays and solar radiation, satellite orbital and clock errors as well as the receiver's clock bias (e.g. O'Driscoll & Borio 2009, Ward et al 2006). These effects degrade GPS signals and various methods have been introduced to cancel or reduce them (e.g. Lachapelle 2009, Misra & Enge 2006).

## 1.1 Indoor GNSS signal acquisition and processing challenges

The typical L1 C/A GPS Signal to Noise Ratio (SNR) in open sky conditions with a bandwidth of 2 MHz (the main bandwidth of GPS L1 C/A code) is in the neighbourhood of -19 dB (Misra & Enge 2006). A more common way to quantify the

signal power in GNSS signal processing literature is by using the Carrier to Noise Ratio ($C/N_0$), which is based on a 1 Hz bandwidth and, therefore, the mean value of $C/N_0$ for normal outdoor environments is around 44 dB-Hz. While the GPS signal at such strength can be tracked using conventional receivers, in urban or indoor areas diffraction, reflection and refraction and attenuation by obstacles and structural materials result in signal degradation. Many researchers have investigated signal attenuation for various frequency bands, however Klukas et al (2004) focused on the GPS L1 signal and measured that the corresponding attenuation of a single layer of obstruction depending on its material can be as high as 30 dBs and as the amount of material increases, attenuation further increases.

Besides signal attenuation, in indoor or multipath environments, the Line of Sight (LoS) signal component might be very weak or even unavailable and incoming None LoS (NLoS) signals arriving with different Times of Arrival (ToA) and from different and varying Angles of Arrival (AoA) where the temporal and spatial variations of AoA introduces Angle Spread (AS). Furthermore, under NLoS conditions a mixture of signals with different phases and delays arrive at the receiver and these interference reduce the SNR of the received signal and distort the correlation peaks of the GNSS signal, which affects the performance of the discriminators in delay lock loops and frequency lock loops. Also, AS introduces a Doppler spread that lowers the velocity estimation accuracy in Doppler based velocity estimation algorithms. Another observed effect of multipath fading due to multiple random NLoS components is rapid fluctuations in the amplitude of the received signal (Blaunstein & Andersen 2002).

**1.2 Beamforming advantages**

In recent years, multiple receive antennas or antenna arrays have been devised to enhance signal detection and parameter estimation performance via beamforming or diversity systems. By adjusting the delay of the received signal of each element, the beam of the arrays' gain pattern can be steered towards desired targets.

Firstly, arrays can be used to detect the AoA of incoming signals and can therefore be used to estimate the AoA profile and AS of various multipath environments. This information can be used in context aware receivers to alter the receiver's strategy upon entering multipath areas in order to enhance position estimation and navigation solution accuracy.

Secondly, by taking advantage of arrays and array processing methods such as beamforming as a spatial filter, the beam of the signal can be steered towards the LoS direction when available to mitigate multipath components and other interfering signals. This results in increasing the SNR of the signal entering the receiver. Both the AoA information and higher SNR enable receivers to estimate code and frequency more reliably than traditional methods (Broumandan 2009). However, implementing a physical array in many GNSS applications is not feasible due to bulky hardware, required complex multichannel receivers and sophisticated array calibration processes. Antenna arrays can be synthesized by moving a single antenna element or a few antenna elements and capturing signal samples in a timely fashion. This motion can be on a predefined or arbitrary path; however, the position where each sample was taken must be known perfectly. Another advantage of synthetic arrays with respect to physical arrays is their

motion dependent aperture, which allows the adjustment of array performance metrics simply by changing the motion domain of the elements.

## 1.3 Background

Estimation and characterization of GNSS AoA in multipath conditions and applying beamforming to mitigate multipath using arrays are successors of two major research topics: array processing and AoA finding. The following sections review related literature in these fields.

### 1.3.1  Array Processing

The idea of using antenna arrays originally comes from radar systems and has also been in use in wireless communication in the past decades. In communication systems, by using multiple spatially separate antennas, signals that come from different directions to different antennas can be combined, providing diversity gain in the process and alleviating the effects of fading. The main idea behind array processing schemes is that by adjusting the delay of the received signals according to the geometry of the array, the main lobe of the array's gain pattern can be steered towards any desired direction, which is called beamforming. Jong & Herben (1999) used a Uniform Circular Array (UCA) to investigate the contribution of multipath in wireless mobile channel. Jong (2001) later used a rotating arm with constant angular velocity to generate a synthetic UCA.

Broumandan et al (2007) introduced the synthetic array idea to GNSS by proposing an algorithm to estimate the direction of incoming interfering signals. Also Pany & Eissfeller (2008) employed this idea by using a circular synthetic array to mitigate carrier and code to find the AoA of GPS signals for outdoor conditions.

Broumandan et al (2008) employed a rotational synthetic array via MUltiple SIgnal Classification (MUSIC) method to implement a high resolution AoA finding. Soloviev et al (2009) utilized the linear motion of a linear array to form a rectangular synthetic array. In other words they used a combination of physical and synthetic array antennas to form high resolution radar using the GPS network via an FFT based method. Lin et al (2009) compared the performance of various AoA findings and beamforming methods. The methods they used include Beamscan, Capon and MUSIC algorithms to find the AoA of incoming signals. Also, the implemented beamforming methods to amplify GNSS signal reception in outdoor environments include the Delay-and-Sum, MVDR/MPDR and LCMV/LCMP beamformers.

Finally, Broumandan et al (2011a) have compared the signal acquisition performance of a synthetic array under random motion indoors with a static antenna in terms of processing gain.

It must be noted that to use the synthetic array concept, the relative position of the antenna must be known precisely at the centimetre level (Lin et al 2009). To achieve this Broumandan et al (2007) used an INS to locate the GNSS antenna at each time step, while Lin et al (2009) and Pany & Eissefeller (2008) utilized precise rotational tables to synthesize the array.

### 1.3.2 AoA Finding and Modeling

AoA estimation was first employed in the radar and sonar industries (Van Trees 2002) and was then taken to other areas and has recently been introduced to GNSS. Besides the novel experiments in the field of GNSS, other applications of AoA finding

include telecommunication systems, wireless internet broadcasting (Wong et al 2008) and Ultra Wide Band (UWB) positioning (Akgul & Pahlavan 2010).

For the case of telecommunication systems, Turin et al (1972) proposed the very first model for urban canyons; thereafter, Saleh & Valenzuela (1987) proposed the first statistical model for Time of Arrival (ToA) of signals in indoors based on the impulse response of the environment. Tang & Sobol (1995) studied various other aspects of the indoor propagation channel, including the propagation through buildings as well as the effects of motion for implementation in personal communication systems. Ganesh & Pahlavan (1993) also studied variations in the indoor channel due to movement dynamics while Todd et al (1992) employed a multiple antenna system to evaluate antenna diversity performance.

Finally, the work most closely related to the current research was done by Spencer (1996, 2000). The previous ToA based models for indoor propagation were completed by introducing a distribution for AoA. They used a narrow beam directional antenna to collect data and proposed a Laplacian distribution for the AoA of arriving signals in indoor environments. Also in the field of indoor navigation, Akgul & Pahlavan (2010) have employed simulations, based on the work of Turin (1972), Saleh & Valenzuela (1987) and Spencer (2000), to propose a new statistical AoA model for indoor UWB navigation.

Other efforts in this field include those of O'Driscoll et al (2007) who investigated the effect of antenna orientation on GNSS signals reception. They mounted six antennas on six sides of a cube and compared the performance of signal acquisition of each antenna under multipath conditions. A more convenient way to estimate AoA is via

array processing techniques. For example, Schmidt (1986) introduced the Multiple Signal Classification (MUSIC) algorithm and Roy & Kailath (1989) devised Estimation of Signal Parameters via Rotational Invariance Techniques (ESPRIT) as two major high resolution AoA finding methods. Later, Zolotowski & Mathews (1993) introduced a closed form 2D angle estimation using a UCA through ESPRIT.

## 1.4 Limitations of Previous Work

As mentioned earlier, while an extensive effort has been made to improve GNSS navigation in outdoor environments, in the past few years indoor navigation using GNSS still remains an interesting research topic. Besides the generally lower SNR indoors, which is caused by signal attenuation, NLoS signals imply rapid fluctuations on the received power level, while the LoS signal might be very weak or even unavailable. The NLoS signals also degrade the receiver performance by affecting the frequency lock loop and delay lock loop discriminators (Broumandan et al 2008). Besides SNR, due to multipath fading, the received frequency and code corruption also becomes a function of time even if the receiver's position remains stationary (Broumandan 2009) and consequently all these phenomena lead to loss of lock or even failure in the receivers' operation (Ward et al 2006). Even under mild multipath conditions, the multipath signals that impinge on the receiver's antenna may imply false pseudoranges and degrade the navigation performance. Therefore, other methods should also be employed to improve signal acquisition and tracking.

To alleviate the aforementioned effects in stand alone receivers, several methods have been devised to track weak GNSS signals known as High-Sensitivity GPS (HSGPS). These methods also include increasing the integration time in order to improve

signal reception sensitivity (e.g. Van Dierendonk et al 1992, Braasch 2001, Kazemi & O'Driscoll 2008). However, for standalone receivers, the maximum coherent integration time is limited by the data navigation length of 20 ms; Also Broumandan et al (2011b) have shown that the coherent integration performance is limited by the motion of the receiver and AS of the environment.

As mentioned previously, Akgul & Pahlavan (2010), Spencer (1996, 2000) and other researchers have provided statistical models for the AoA of telecommunication and UWB signals in indoor environments. Unfortunately, these models are not reliable in the case of GNSS navigation since they are dealing with much more powerful signals and their frequency range is completely different from that of this research.

Furthermore, one of the goals of this research is to mitigate the unwanted Multipath Components (MPC) via beamforming. Using a directional antenna is another way to mitigate the effects of multipath since it filters out the out-of-beam signals. As used in Spencer (1996, 2000), a directional antenna might be a feasible solution for telecommunication purposes where there is only one signal source with a known direction and the user prefers to reject all other incoming signals other than Line of Sight (LoS). However, for the case of GNSS navigation the user should be able to track the signals that are transmitted from several satellites that are spread widely in the sky. Therefore, the use of an array first, helps the user to find the direction of incoming signals, and second, provides a means of focusing on multiple sources and steering the nulls of the array's pattern gain towards the unwanted signal sources. Besides this feature, since in indoor conditions the signal at a certain point may not be present or may be too poor to provide the receiver with sufficient data, an array can be used to collect

and process signals from various points of space which is another major benefit of employing arrays.

While Lin et al (2009), Soloviev et al (2009), Pany & Eissfeller (2008) and Broumandan et al (2007) have exploited various aspects of employing synthetic arrays in outdoor environments, the potential applications of synthetic arrays for indoor conditions are still interesting topics. The most fundamental part of these applications includes the effect of forming the beam towards the GNSS satellites and assessing the further increase in signal SNR. However this may only be efficient in mild multipath and fading environments due to the limitations of the AoA finding methods and also the behaviour of the signal in harsh multipath conditions.

## 1.5 Research Novelties

Many researchers have addressed the problem of AoA in indoor conditions for many applications but unfortunately not many have addressed the AoA profile and AS for the case of the indoor GNSS channel. The main goal of this research is to characterize the AoA distribution of GNSS multipath channels in various indoor environments using a UCA. Another goal is to explore the capabilities and limitations of the AoA estimation and beamforming methods in multipath environments since array performance decreases as AS increases (Broumandan 2009, Freidlander & Scherzer 2006). Besides AoA estimation, the peak of the array's gain pattern can be steered toward desired directions. This can be used to mitigate the multipath components and other interference to increase the SNR of the incoming signal and remove the multipath errors. Therefore, another goal of this research is to assess the signal improvement qualities via beamforming in terms of array gain. Besides AoA profile and AS estimation, and beamforming performance

assessment under multipath, the governing fading channel model, the signal correlation coefficient and the signal level spatial variations in terms of $C / N_0$ are also analyzed in different fading channels. The following sections elaborate on the main goals mentioned above. Besides these parameters, many influential effects on AoA estimation via UCA are also analyzed both theoretically and practically. These effects include the phase wrap-up introduced in rotating antennas and the effect of the antenna gain pattern.

As will be discussed in more details in Chapter 4 and Chapter 5, the phase wrap-up phenomenon (rotational Doppler) introduces an additional phase shift in rotating antennas that are receiving circularly polarized signals (e.g. Wu et al 1993, Tetewsky & Mullen 1996). This effect was known to the GPS based mapping society (Tetewsky & Mullen 1996) and in the current research it was observed in practical components through experimental measurements. Therefore, modifications to current mathematical formulas of the Doppler shift of mobile antennas are proposed to accurately compensate for this additional component.

As mentioned earlier, the gain pattern of the antenna element itself affects the array gain pattern and this may have a significant influence on the measured AS. This effect is addressed mathematically through simulations and practically in Chapter 3, Chapter 4 and Chapter 5, by considering different GPS antennas with different gain patterns.

The AoA characterization of the GNSS multipath channel is the main topic of this thesis. Therefore, a brief introduction on AoA and AS characterization and beamforming is included below.

### *1.5.1 AoA and AS characterization*

The AoA information can be used as an input for array steering methods to form the beam towards desired signals and steer the nulls of the array towards unwanted interference such as multipath and jamming. The main method of AoA estimation in this research is based on the Beamscan technique that simply searches the entire field of view for signal hotspots. This method does not need any side information such as the number of incoming signals and, if calibrated correctly, provides satisfactory results in mild to moderate conditions. To form a more precise AoA distribution instead of only recording and studying the highest peak of each sample, a supplementary code has been developed that captures the measured AoA spectrum from beamscan, detects its peaks' location and level according to a certain threshold and stores the results. The output of this code will be used in quantizing the distribution of AoA and AS in various environments with different multipath levels. The distribution of AoA in multipath conditions determines if a distinct significant source of GNSS signals exists for the indoors or if the signals come from various angles and the governing pattern is the sum of rings of scatterer. Besides these, many factors such as array beamwidth and gain pattern along the gain pattern of the employed antenna element should be accounted for. Other issues regarding the indoor GNSS channel that will be considered along AoA distribution include the fading channel model (Rayleigh vs. Rician), the correlation coefficient between the samples and the channel coherence time, since these parameters determine the fading characteristics of the channel which dominates the array performance.

*1.5.2 Beamforming*

As mentioned earlier, beamforming is an effective tool to cancel multipath and other interference (e.g. Pany & Eissefeller 2008, Soloviev et al 2008, Broumandan et al 2007) and its result (when performed correctly under open sky conditions) can be identical to coherent integration while benefitting from both temporal and spatial signal samples (Soloviev et al 2008, Broumandan 2009). A major advantage of beamforming with a synthetic array over coherent integration with a single static antenna is the advantage of collected samples in various locations that provides the capability of steering the array main beam and nulls towards desired and unwanted signals respectively, in Rician fading channels. This capability increases the SNR and is measured in terms of Array Gain in decibels. Freidlander & Scherzer (2004) and Broumandan (2009) have shown that AG decreases as AS increases under multipath conditions for linear arrays. This loss needs to be characterized both in theory and in real applications for circular arrays as well. Therefore, in terms of assessing the beamforming performance, such parameters as array gain and ToA improvement will be assessed. Delay and Sum (A.K.A as the conventional beamformer) is the proposed beamforming method in this research.

To sum up, the main topic of this research will be to attempt to characterise the GNSS signals in indoor environments using a UCA. In addition to these and as a part of the research, the limitations of the AoA finding methods and capabilities of beamforming methods will be investigated.

**1.6 Methodology**

The main focus of the research will be on employing AoA estimation methods to determine the AoA of GNSS signals in different multipath environments and to investigate whether a dominant source of signal exists or not. Furthermore, it will focus on removing multipath using beamforming in mild multipath.

In the first step, AoA estimation methods will be used to characterize the multipath channel of GNSS signals. The major AoA method that is going to be employed is Beamscan (Allen & Ghavami 2005) and will be applied to GPS data that are collected in different multipath conditions. The first proposed data collection will be under open sky conditions to calibrate and verify the performance of the developed code.

The data collection equipment to be used includes a very precise rotating table. The antenna will be mounted on a lever arm and the aforementioned table will rotate the antenna at a specific angular pace. Also, by knowing the initial direction of the arm (e.g. north) and the position of the array centre, the antenna trajectory will be known accurately to implement beamforming algorithms. This antenna, called the rover antenna, will be connected to an NI RF-Front end to capture the received signal on the GPS L1 frequency. Also, another antenna, called the reference antenna, will be placed in the outdoors in the vicinity of the data collection site and will be connected to the front-end. The main idea behind the reference-rover architecture is to synchronize the time delay between the synthetic array samples to be discussed in Chapters 3 and 4.

The assembly will then be taken into various multipath environments including open sky conditions with low/no multipath, urban canyon with mild multipath and fading, a wooden structured residential building and an office environment on the University of

Calgary campus, to evaluate the multipath characteristics of each environment. The collected data will then undergo a computer processing stage.

The computer processing stage will consist of two pre-processing and post-processing levels. The pre-processing stage will be done via GSNRx-rr (Satyanarayana et al 2010) which is an extension of GSNRx™, a GNSS software navigation receiver developed by PLAN group (O'Driscoll et al 2009) that produces the complex correlation peaks of the signals received by the rover antenna. These complex peaks will then be plugged into the post-processing stage. The post-processing stage will consist of computer programs that have been developed in MATLAB® to perform AoA finding.

The mean difference between the detected signal peak and the Line of Sight (LoS) direction of the corresponding satellite will be studied and will be called the "mean AoA estimation error". The temporal changes of the "mean AoA estimation error" as well as the variance of detected signal peaks for each condition will be investigated and analyzed. Also the, temporal and spatial variations of weaker peaks will be considered since the peaks' powers tend to change over time for high attenuation and/or dense multipath environments. The output of this step will be employed to investigate how the AoA of the signals varies over time in multipath conditions and to assign a suitable model for the GNSS indoor channel.

Furthermore, based on the above results, the effort will be focused on amplifying the GNSS signals by employing the Delay and Sum method. Finally, to assess the performance of beamforming, the array gain concept, which is the ratio between the signal powers of the inputs and outputs, will be computed in terms of dBs. This quantity will be compared against the computed theoretical values for each scenario.

A side attempt is also made to develop a software simulator that has the ability to simulate the complex signal that is received by an arbitrary array, which is the result of impinging various signals from various directions with different signal powers. This simulator will provide the ability to perform statistical analysis based on the proposed models to verify the AoA finding methods and beamforming algorithms capabilities in theory and practice. Using this simulator, the effects of phase wrap-up and antenna gain pattern on the AoA estimation performance have been assessed.

## 1.7 Thesis Outline

In Chapter 2 the fundamentals of the GNSS signal structure are briefly reviewed. The basics of GNSS signal processing are then discussed. This is necessary to understand the concepts that are introduced in later sections. After reviewing the GNSS signal structure and processing, the GNSS multipath channel is introduced. Signal envelope models, AoA and AS definition and models are then discussed.

Chapter 3 addresses the related topics of the array processing techniques. Firstly, the signal model in physical arrays is discussed. Afterwards, the signal model in the synthetic arrays is introduced and this is linked to the signal model in the physical arrays. In consequent sections, the beamforming and AoA estimation methods are described. Afterwards the concept of the array gain is presented and the effects of the array geometry, size, number of the elements and elements' gain pattern on the array gain pattern are discussed.

Chapter 4 discusses issues related to the implementation of synthetic UCAs. The first issue addressed is the phase wrap-up effect. This effect is addressed both

mathematically and through simulations. The effects of several factors such as satellite-receiver geometry are analyzed.

Another issue covered is the antenna gain pattern effect on AoA estimation accuracy and AS measurements. This issue is briefly addressed in Chapter 3, however a more in depth analysis is presented in Chapter 4. This analysis includes comparing the effect of three antenna elements, namely the NovAtel GPS 701/702 GGL series, the Ublox M-335 (that are used in real world signal measurements in Chapter 5) and a hypothetical isotropic antenna element. This analysis provides an understating of how each antenna performs under multipath and transforms the true AS pattern.

The third issue addressed in Chapter 4 covers the gain degradation due to the reflector angular spread and the circular motion of the synthetic array. Broumandan et al (2011b) address this issue for linear motion. This discussion follows the aforementioned work and adapts it to the circular motion and also addresses the array gain loss instead of the loss in the processing gain in coherent integration.

Finally, in Chapter 5 GPS signals collected in real multipath scenarios are analyzed by the mentioned methods. The real world environments include open sky conditions on the top of a building on the U of C campus, an area in the U of C campus that resembles urban canyon environments, a residential wooden structure and a lab environment that is associated with harsh fading and multipath conditions. The main measured parameters include AoA, AS, AG, correlation coefficient, signal level variations and the channel fading model. However, the dataset collected in the open sky condition is contaminated with the phase wrap-up phenomena. Therefore, this effect is wiped-off based on the analysis that was contained in Chapter 4, and the phase wrap-up

effect on the AoA estimation accuracy and the accuracy of the proposed formulas to estimate the phase wrap in practice are also demonstrated and included in this section.

In addition, the effect of the antenna element gain pattern in practical scenarios is considered in the data set collected in the wooden house and the laboratory environment. In these data sets, both the Ublox and NovAtel antennas (that were mentioned earlier) are used and the resulting measured parameters are compared against each other.

Finally, in Chapter Six concluding points are presented and recommendations for future work are presented. The structure of this thesis is outlined in Figure 1.1.
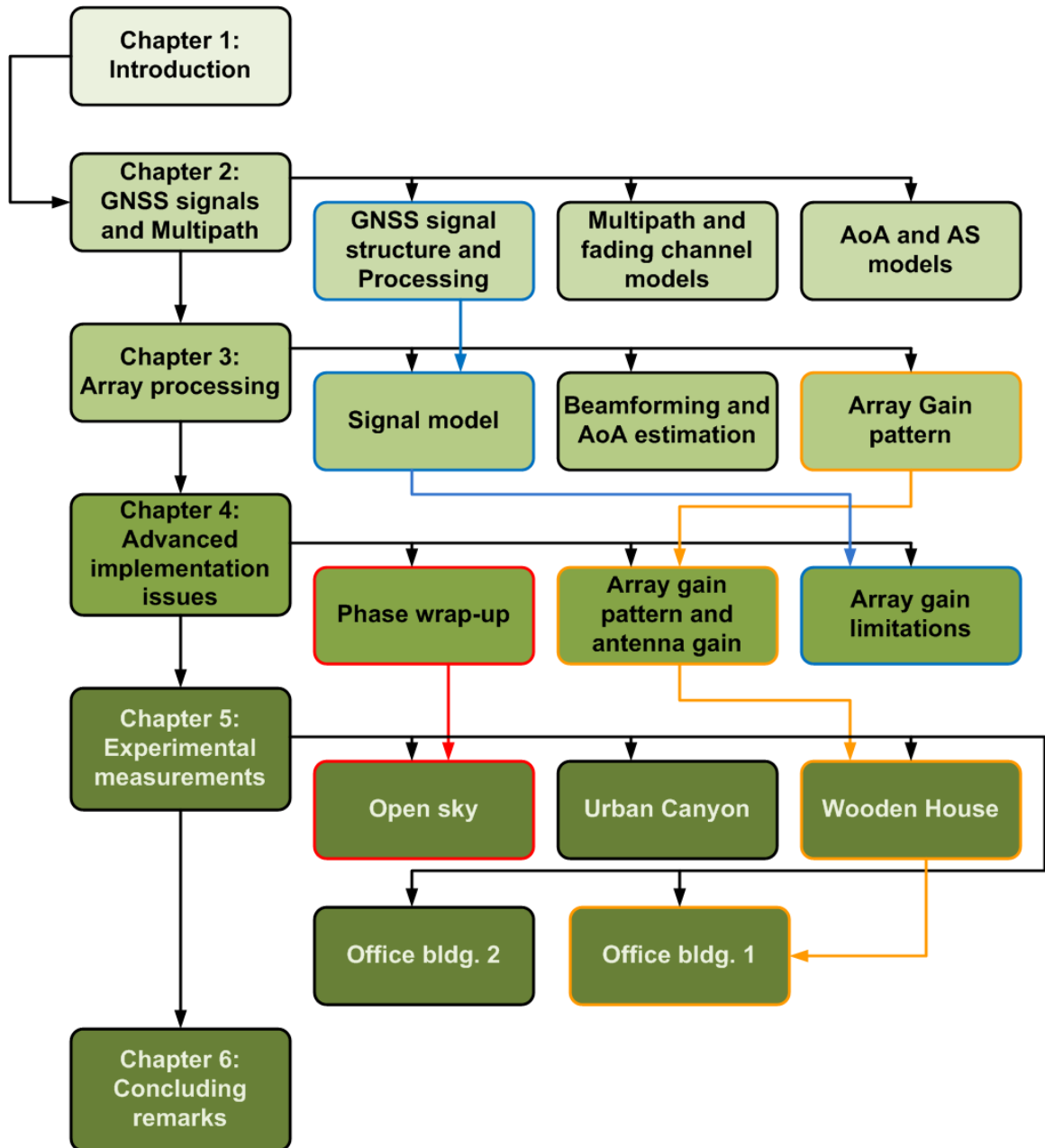
**Figure 1-1: Thesis structure**

**Chapter Two: GNSS Signal Model under Multipath Channel**

## 2.1 Overview

This chapter is mainly focused on GNSS signals structure, the multipath effect, GPS signals characteristics under multipath conditions and the basis of GNSS signal processing. The main motivation to include this material was first to provide some necessary background information and second, to illustrate the connection between GNSS navigation and array processing. The chapter is structured as follows: The fundamentals of GPS signal structure are discussed in Section 2.2. Section 2.3 presents a brief and concise review of GPS signal processing up to generation of the complex correlation peaks that are fed into the array processing techniques. Section 2.4 and Section 2.5 illustrate the multipath phenomena, multipath signal channels and scatterer models. Section 2.6 and 2.7 present the signal envelope models, namely the Rician and Rayleigh channel models, along with the definition of AoA and Angular Spread (AS).

## 2.2 GPS Signal Characteristics

GPS satellites broadcast Right Hand Circularly Polarized (RHCP) electromagnetic waves over a common frequency band (e.g. Ward et al 2006a, Misra & Enge 2006). Direct Sequence Spread-Spectrum (DS-SS) is a digital signalling scheme implemented in various positioning systems including GPS (Ward et al 2006a). In this particular coding scheme, two layers of data are modulated on the carrier and are known as the data and the spreading waveforms. In positioning systems, the data waveform is a sequence of binary bits, also known as the navigation data bits. The length of each navigation data bit for the case of the GPS L1 civilian code is 20 ms. The spreading waveform also modulates the GPS signals by a "Binary Phase Shift Keying" (BPSK)

scheme with a considerably higher frequency and with a specific (and often repetitive) structure. The finite sequence of bits that is used to generate a spreading waveform is known as Pseudo-Random Noise (PRN) and is completely known to the intended receivers. These layers of modulating and spreading are illustrated in Figure 2-1.
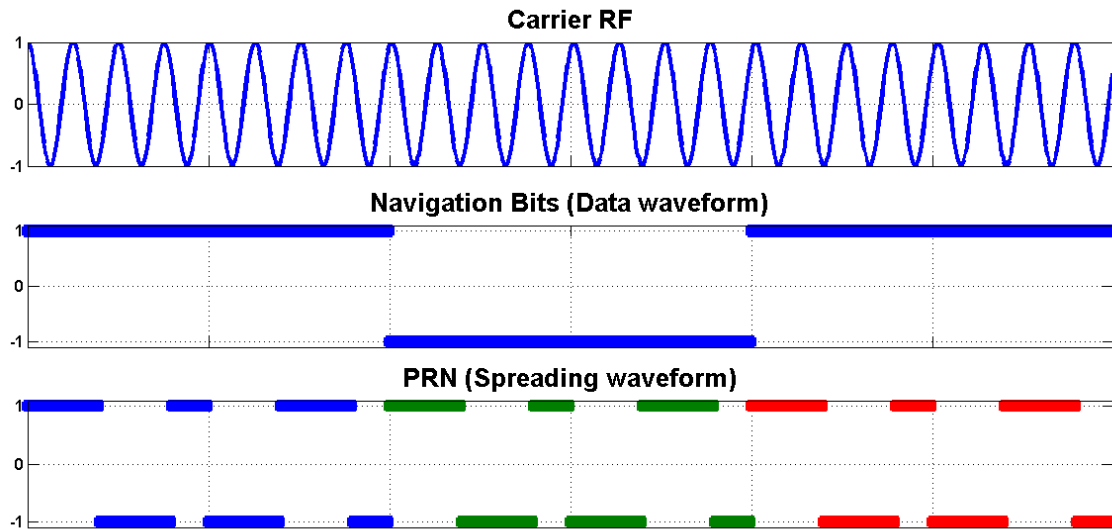


**Figure 2-1: Carrier RF, navigation bits and PRN concepts**

In the DS-SS systems, the overall code, which is generated from the product of the PRN sequence and the Navigation bits (which is either -1 or +1), determines the phase of the carrier. In other words, if the value of the sequence is "+1", the phase of the transmitted RF-carrier will be "0". On the other hand, if the sequence value is "-1", the modulation phase will be "180" (Ward et al 2006a). This modulation concept is shown in Figure 2-2. The smallest part of the PRN code is called a chip and its length in time is called a chip period, $T_c$. The generation rate of the chips is called the chipping rate, $R_c$ and the time parameter that is used to measure the relative length of a PRN code and its compound chips is called the code-phase (Ward et al 2006).
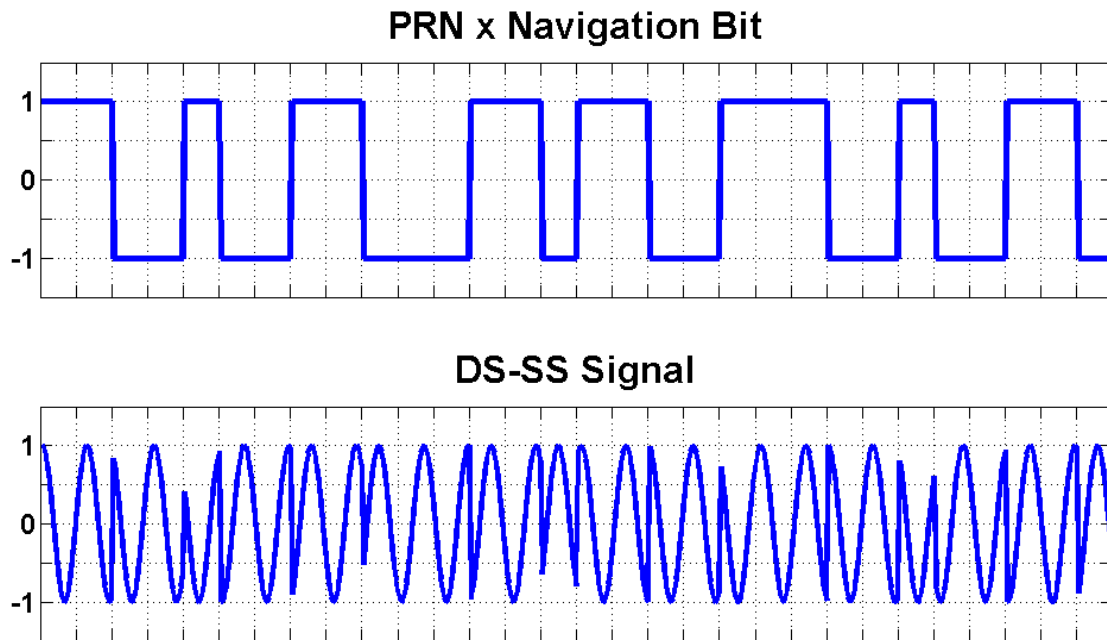
**Figure 2-2: DS-SS modulation**

A major benefit of using DS-SS is that, by assigning a unique code to each source, a single common frequency band can be used for transmission of signals from all GPS satellites. This particular type of channel sharing using multiple codes on a single frequency is called Code Division Multiple Access (CDMA). Another benefit is that DS-SS signals are somehow robust against narrowband interference.

In GPS, the cross-correlation between the assigned PRNs and the satellites is almost zero. Also the auto-correlation value of each PRN is almost negligible except at the zero lag. These characteristics of the PRN codes enable GPS receivers to find the exact instance when the signal arrives at the receiver using the auto-correlation peak of each PRN. Therefore, the estimated correlation peak can be considered as the propagation delay between the satellite and the receiver, if the receiver and transmitter are

synchronized. This is the foundation of the Time of Arrival (ToA) estimation technique. This estimation process is performed via a code acquisition procedure or simply an *acquisition* in which the receiver locally generates a replica PRN code and correlates it in time domain with the received signal to detect the maximum correlation peak. This code matching scheme to acquire the PRN codes is illustrated in Figure 2-3.

The transmitted signal from the satellite can be represented by its complex envelope or the low-pass representation, defined by

$$s_l(t) = s_I(t) + js_Q(t) \tag{2-1}$$

where $s_I(t)$ and $s_Q(t)$ are the in-phase and quadraphase components of the real signal $s(t)$. The autocorrelation function (ACF) of $s_l(t)$ can be defined as

$$\tilde{R}(\tau) = \lim_{T \to \infty} \frac{1}{2T} \int_{-T}^{T} s_l(t)^* s_l(t+\tau) dt \tag{2-2}$$

where * denotes the complex conjugate operation.

The power distribution over different frequencies of a signal is called Power Spectral Density (PSD) and can be derived from the Fourier transform of its ACF as

$$\Psi(f) = \int_{-\infty}^{+\infty} \tilde{R}(\tau) e^{-2j\pi f\tau} d\tau. \tag{2-3}$$
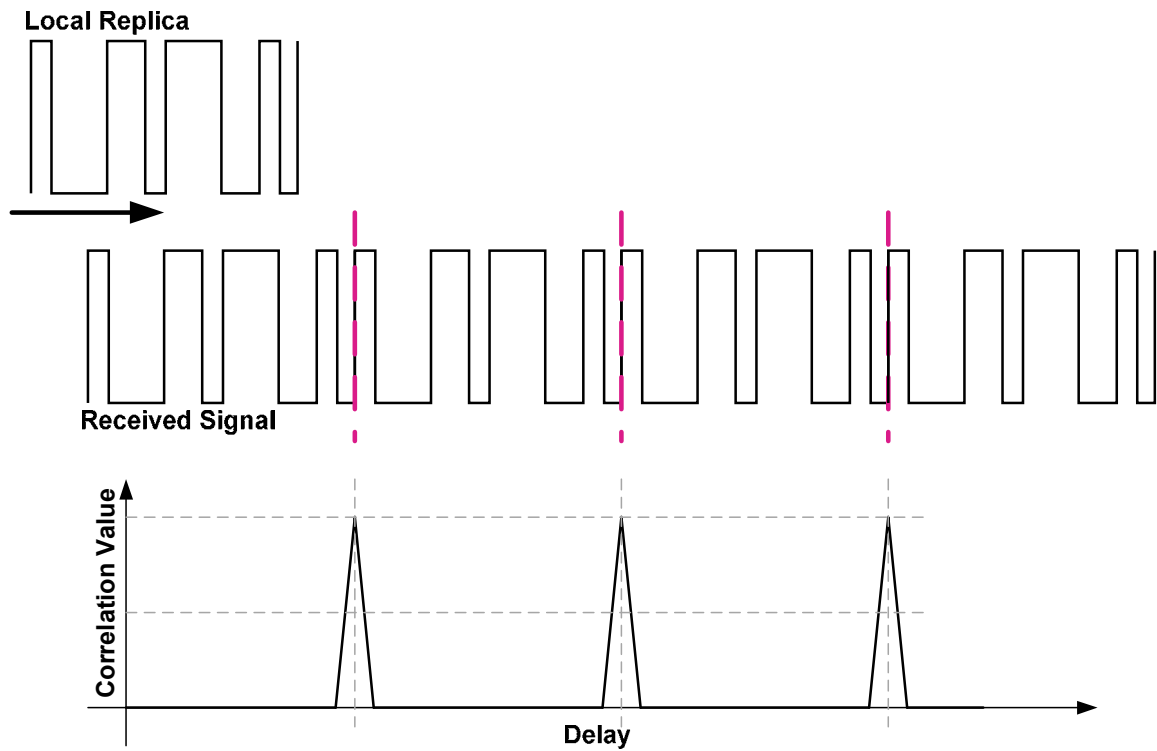
**Figure 2-3: Correlation process and ToA estimation**

The GPS PRN codes can be modeled as random binary codes where the probability of both "+1" and "-1" outcomes are equal (Ward et al 2006a). The ACF of such a sequence is plotted in the first part of Figure 2-4. The PSD of this sequence is also plotted in second part of Figure 2-4 which is proven to have a sinc pattern. In Figure 2-4 (a, b), $A$ represents the amplitude of the binary code. To conclude this section, the structure of the civilian GPS signals is summarized in Table 2-1.
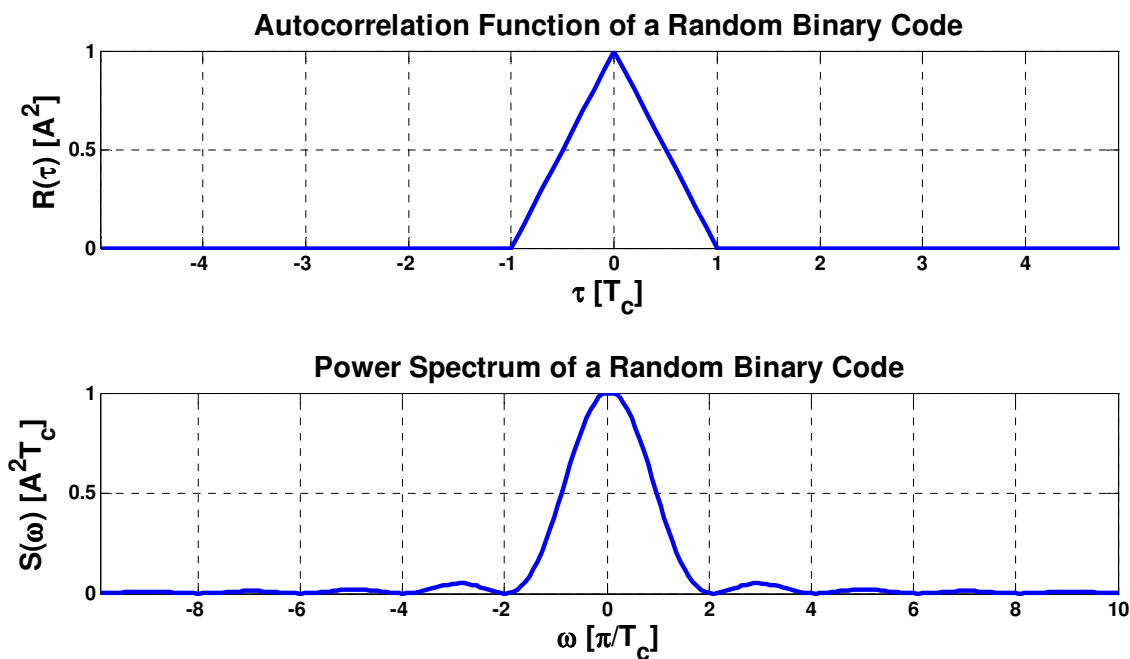
**Figure 2-4: ACF and PSD of a random binary code**

**Table 2-1: GPS C/A signals structure**

| Signal Designation | L1 C/A | L2 C | L5 |
|---|---|---|---|
| Carrier Frequency (MHz) | 1575.42 (154x10.23 MHz) | 1272.60 (120x10.23 MHz) | 1176.45 (115 x 10.23 MHz) |
| PRN code chipping rate (Mchips/s) | 1.023 | 1.023 | 10.23 |
| Nav. Message data rate (bits/s) | 50 | 25 | 50 |
| Bandwidth (MHz) | 2.046 | 2.046 | 20.46 |

It must be noted that the received signal frequency is not exactly the designated carrier frequency and has offsets due to the Doppler phenomenon induced by the relative motion between the receiver and the satellite and the receiver oscillator instability. Therefore, the receiver must search in both the code (time) and frequency domains within a specified range of frequencies that is determined based on each specific application to detect the correlation peak. The received frequency is calculated as

$$f_{Rx} = f_{Tx}\left(1 - \frac{v_{Rx-SV}}{c}\right)$$

<div align="right">(2-4)</div>

where $f_{Rx}$ and $f_{Tx}$ denote the received and transmitting frequencies, $v_{Rx-SV}$ is the absolute range rate between the receiver and the satellite and $c$ is the speed at which electromagnetic waves propagate ($c \approx 299792458.0 \ m/s$).

## 2.3 Processing of GPS signals

The details of the GPS receiver processing strategies are not the main topic of this research and require separate consideration. However, to have an idea of how the RF GPS signals are taken from the receiver's antenna to the digital domain and prepared for synthetic array processing, a short review of the basic operations of GPS software receivers is presented below.

The frequency of the received GPS signals is normally too high for efficient processing (O'Driscoll & Borio 2009); therefore it is down-converted to an Intermediate Frequency (IF). A high level block-diagram of a GNSS receiver process is depicted in Figure 2-5 (Ward et al 2006b) where the process of down-conversion using frequency mixing is illustrated (Broumandan 2009). The output of the frequency mixers is entered into a Low Pass Filter (LPF) to reject the high frequency components while preserving the baseband signals. Afterwards, the signal is fed into the receiver block and the in-phase and quadraphase components are converted from the analog to the digital domain. Then, they are sampled and entered into a brute-force search algorithm that tries to find the matching delay and frequency of the corresponding PRN in a 2D uncertainty space. The search process and the 2D uncertainty space are shown in Figure 2-6.
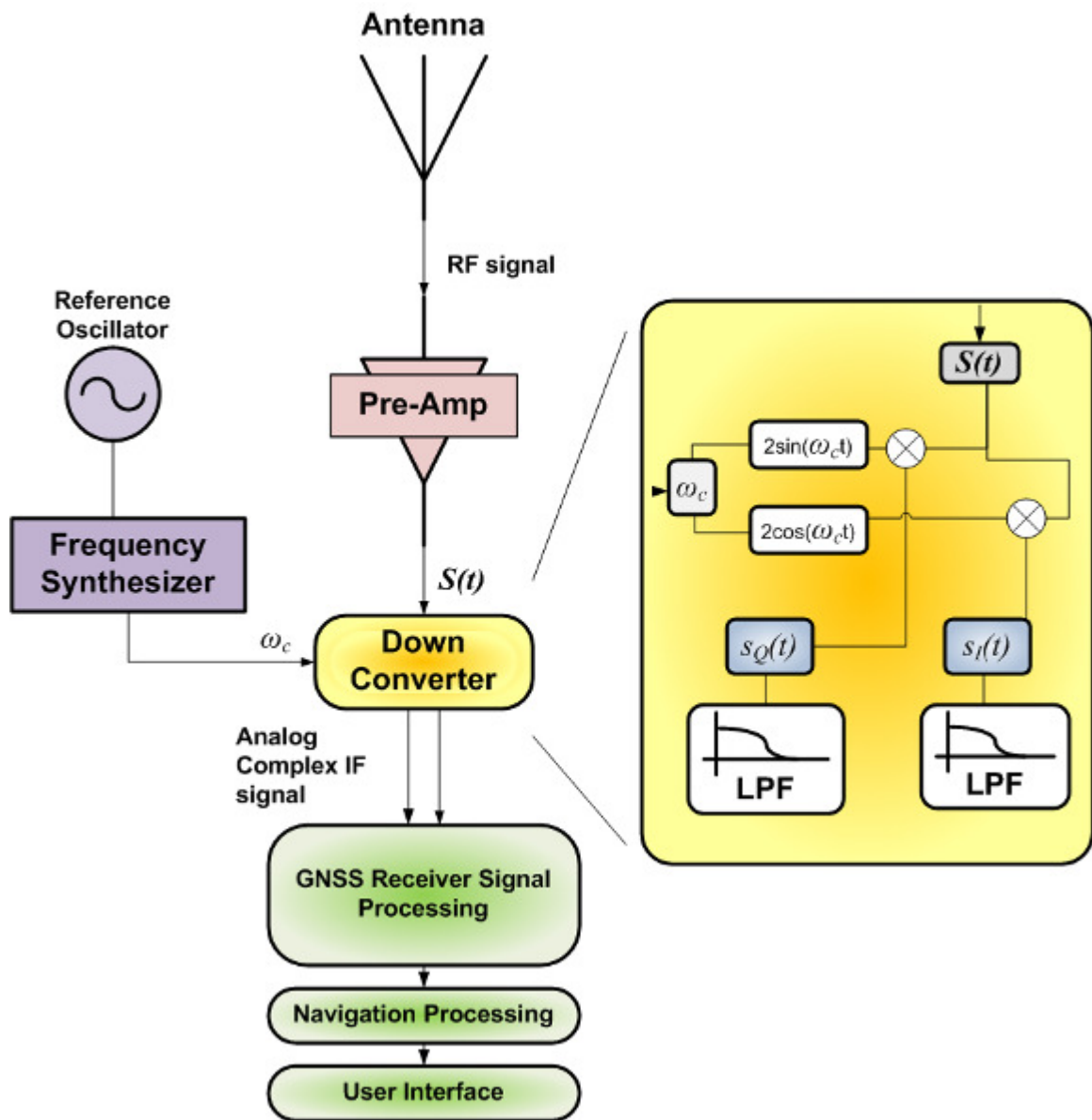
**Figure 2-5: Block diagram of a GNSS receiver process**
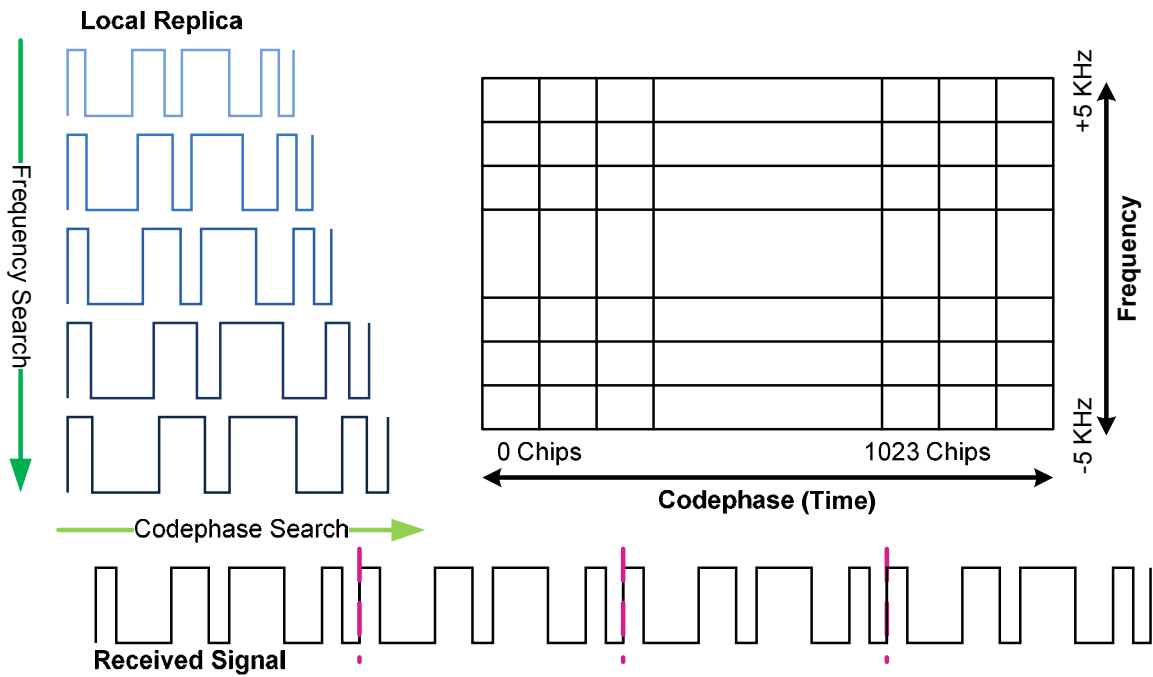
**Figure 2-6: 2D code and frequency search**

The received signal at the receiver processing stage can be modeled by

$$r[n] = s\left[n \middle| \tilde{C}_i \quad \psi_i \quad \tau_i \quad f_d\right] + \eta[n] \tag{2-5}$$

which is a function of carrier power $\tilde{C}_i$, phase of the carrier $\psi_i$, time delay of the signal (code delay) $\tau_i$ and the carrier Doppler $f_d$ .

The subscript $i$ represents the PRN index in the $i^{\text{th}}$ channel of the receiver, $[n]$ is the index number of the sample in time and $\eta$ is the noise component, which is assumed to be Additive White Gaussian (AWG). While the basics of searching for the code phase and the carrier frequency are shown in Figure 2-6, the mathematical structure of this process, known as the correlator or matched filter, is formulated as (O'Driscoll & Borio 2009)

$$S\left(\hat{f}_d,\hat{\tau}_i\right)=\left|r[n]\times e^{-j2\pi(f_{IF}+\hat{f}_d)nT_S}\times c_i\left[n\left(1+\frac{\hat{f}_d}{f_{IF}}\right)-\hat{\tau}_i f_S\right]\right|^2 \tag{2-6}$$

In Equation (2-6), $f_{IF}$ is the intermediate frequency, $f_S, T_S$ are the sampling

frequency and period, respectively, and $c_i[\bullet]$ is the delayed PRN code. $S\left(\hat{f}_d,\hat{\tau}_i\right)$ is the

correlator output, called the Cross Ambiguity Function (CAF). The maximum value of

the CAF is called the correlation peak. If the value of the correlation peak satisfies certain

detection criteria, the process will be denoted as a correct detection and the corresponding

Doppler frequency and code delay of the correlation peak will be chosen as the estimated

signal parameters. A sample of the CAF and its correlation peak are shown in Figure 2-7.
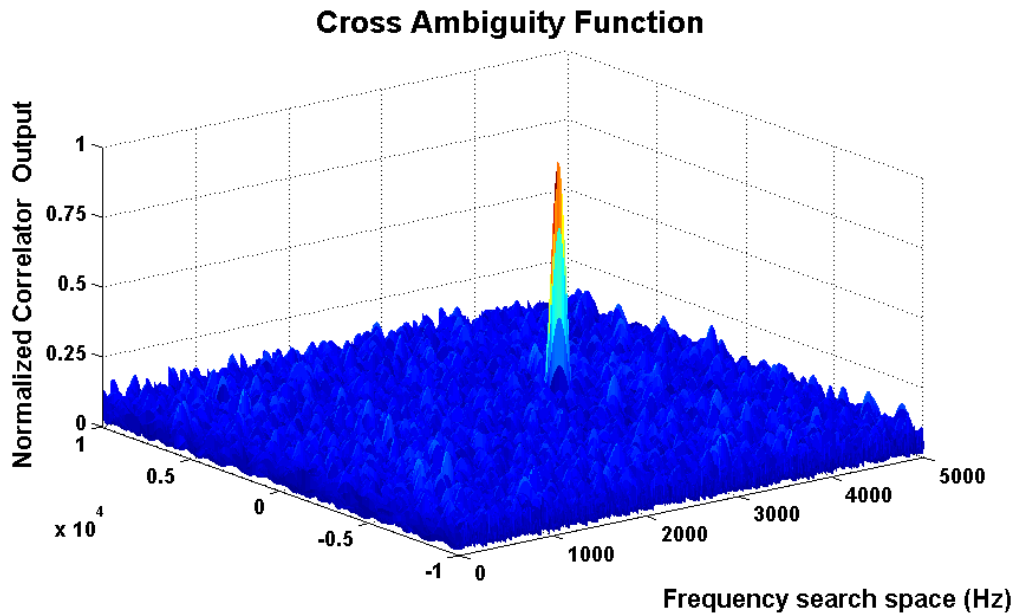


**Figure 2-7: 2D code and frequency search cross ambiguity function and correlation peak**

As mentioned earlier, the chipping rate of the GPS L1 C/A signal is 1.023 MHz, and the length of the PRN codes is 1023 chips. The process, described by Equation (2-6), de-spreads the signal along one PRN code length. By coherently (i.e. considering the phase information of each CAF) adding consecutive CAFs after the despreading process, the SNR increases and a better estimate of frequency and delay can be obtained. This process is called coherent integration and its length is denoted by $T_{coh}$. In contrast, if the phase information is not used and only the absolute values of the CAFs are added together, the process will be called non-coherent integration. The increase in the SNR level via coherent integration is called "Processing Gain". Normally, in most of the outdoor scenarios, the coherent integration time can be increased up to 20 ms, which is equivalent to the length of a navigation bit. The maximum length of the coherent integration time is limited by the navigation bit length (20 ms) and also by the receiver oscillator stability. For indoor cases, by joint estimation or by aiding the receiver process with the navigation data bits, the maximum value of the coherent integration time can be further increased (O'Driscoll & Borio 2009). Finally, upon estimation of the code delay and the Doppler frequency, the maximum output of the correlator (complex correlation peak) is used as the signal entering the array processing algorithms.

## 2.4 GNSS multipath channel

A microwave propagation channel from a satellite source to a receiver located indoors is characterized by a channel gain factor that typically varies randomly with the spatial location and the orientation of the receiver. Also, even if the receiver antenna position and orientation remain unchanged, the motion of the GPS satellites and changes in the surrounding environment can affect the channel gain factor. The spatial changes in

the channel gain typically arise from three different sources: Path loss, shadowing or slow fading and fast fading.

The path loss is caused by the electromagnetic wave's propagation loss in space and therefore it is not considered as a fading effect. Shadowing or slow fading (large scale fading) is imposed over path loss and is caused by blockage of the signal. The shadowing effect reduces the mean level of the signal and causes slow random variations in the received signal amplitude. The spatial scale of such slow variations reaches up to several metres in distance. The third type of fading, known as fast fading or small scale fading, emerges from the mutual interference of several multipath components with slight delays reflected from different obstacles. Such fading causes rapid fluctuations in the received signal power and in the spatial scale, the signal statistics may change even by a fraction of a wavelength. Figure 2-8 illustrates the multipath fading phenomenon. Figure 2-9 shows the effect of fast fading and slow fading on the received signal amplitude (Blauntstein & Andersen 2002).

Under multipath conditions, the signal entering the receiver will consist of several delayed and attenuated replicas of the transmitted signal. Besides delay and attenuation, multipath signals arrive at the receiver with different frequencies as a result of the Doppler spread. The Doppler spread is introduced since the Doppler shift in the received signal frequency depends on the direction of arrival of the received signal and on the orientation and movement of the receiver. Therefore, it is of interest to consider the effect of the fading channel on different frequency components as both the delay spread and Doppler spread exacerbate the performance of the signal acquisition process described in Section 2.3 (Broumandan et al 2011a).
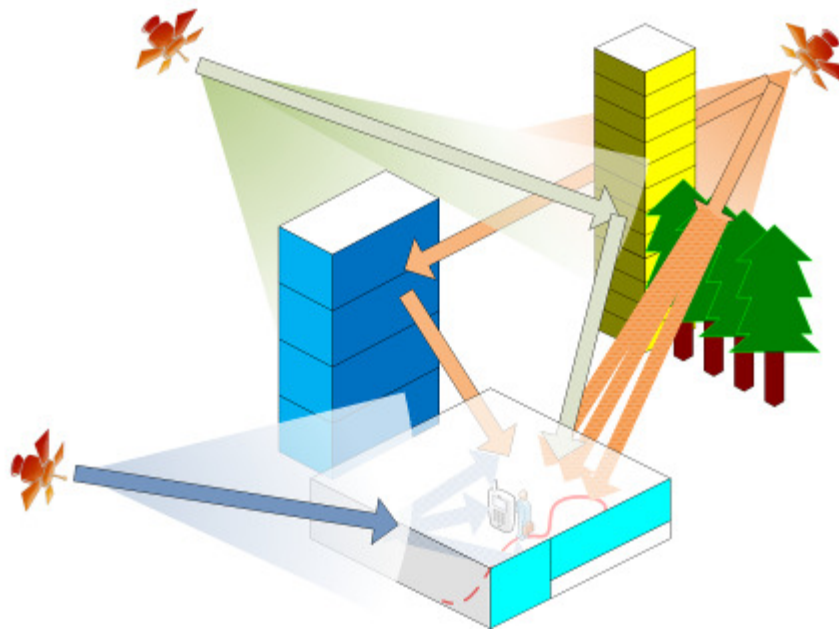
**Figure 2-8: Schematic representation of multipath components in GNSS channel**
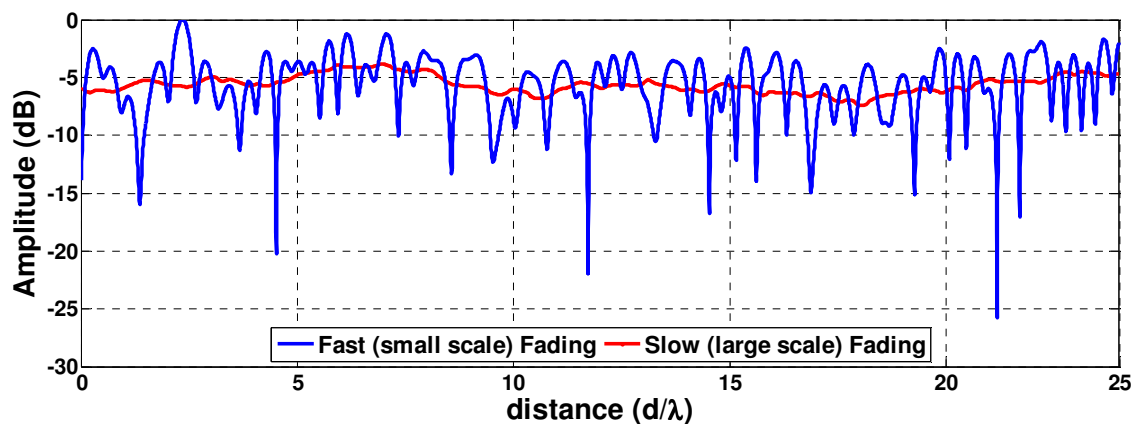


**Figure 2-9: Signal amplitude variations due to different types of fading**

In Broumandan (2009), it is shown that the indoor GPS channel undergoes flat fading (as opposed to frequency selective fading). In this case, the bandwidth of the channel (the reciprocal of the time duration that the channel response can be assumed constant) is greater than the bandwidth of the transmitted signal. In other words, the channel will attenuate the frequency content of the signal equally. If the bandwidth of the

channel is smaller than the bandwidth of the signal, the received signal will endure frequency selective fading (Rappaport 2002).

## 2.5 Multipath models

As mentioned in Section 2.4, as the antenna moves in a multipath environment, the gain of the received signal changes. The signal model based on the narrowband signal assumption can be written as

$$s\left(t,\mathbf{p}\left(t\right)\right)=A\left(\mathbf{p}\left(t\right)\right)s_0\left(t\right) \tag{2-7}$$

where $\mathbf{p}\left(t\right)$ associates the phase centre location of the antenna to a position vector in space. In Equation (2-14), $A\left(\mathbf{p}\left(t\right)\right)$ is the channel response to the incident signal at the antenna position. The received signal at the receiver is corrupted by a white Gaussian noise with a level of $N_0$. Since it is assumed that the noise components decorrelate temporally more severely than spatially, the dependency of noise on the position has been omitted and hence, the received signal in the receiver can be stated as

$$r\left(t\right)=A\left(\mathbf{p}\left(t\right)\right)s_0\left(t\right)+\eta\left(t\right). \tag{2-8}$$

As mentioned in Section 2.3, the receiver accumulates the received signal with the duration of $T_{coh}$. Assuming that the antenna motion is smooth and the receiver's displacement during $T_{coh}$ is much smaller than the carrier wavelength, $A\left(\mathbf{p}\left(t\right)\right)$ can be assumed constant during each coherent integration period, which means

$A(\mathbf{p}(t))\big|_{t_m<t<t_{m+1}} = A(\mathbf{p}(t_m))$, where $t_m$ is the starting epoch of coherent integration.

$A(\mathbf{p}(t_m))$ can be characterized based on the antenna trajectory and the multipath model. These models include the ring of scatterers and the sphere of scatterers and the spatial variations of $A(\mathbf{p}(t_m))$ with respect to $A(\mathbf{p}(t_0))$, and can be studied via the correlation coefficient function. The higher the correlation coefficient between two samples, the smaller the difference and the more similarity between the two samples.

The correlation coefficient of the GNSS signal based on the ring of scatterer model can be formulated by assuming a zero-mean circularly normal distributed channel gain as $A_0 \sim CN(0,\sigma_A{}^2)$. In this model, the AoA is assumed to be spread over azimuth uniformly as $\phi \sim 1/2\pi$, $0 < \phi < 2\pi$.

In an array the signal arrives at the elements with different delays. This time delay between elements can be expressed in terms of "element distance" and the AoA of the incoming signal as $\Delta\tau = \Delta p \cos\phi \sin\tilde{\theta}$. The signal correlation coefficient between two signal samples collected at points $m$ and $n$ of the trajectory with the distance of $\Delta p$ can be computed as (Broumandan 2009)

$$[\mathbf{C}_s]_{m,n} = E\{s(t,\mathbf{p}_0), s^*(t,\mathbf{p}_n)\} \tag{2-9}$$

where $s(t,\mathbf{p}_m)$ is the integral of a infinitesimal signal patch described by

$$ds(t,\mathbf{p}_n) = ds_0(t,\tilde{\theta},\phi)\exp\left(-jk_0\mathbf{a}^T(\tilde{\theta},\phi)\mathbf{p}_n\right), \quad k_0 = 2\pi R/\lambda \quad \text{and} \quad (.)^* \text{denotes the}$$

complex conjugation operation. Also, due to symmetry, Equation (2-9) can be rewritten in terms of the distance between array elements ($|\mathbf{p}_n - \mathbf{p}_0| = |\Delta p|$) as

$$\left[\mathbf{C}_s(|\Delta p|)\right]_{m,n} = \frac{\sigma_A^2}{2\pi} \int_0^{2\pi} e^{\left(-jk_0|\Delta p|\cos\phi_n\sin\tilde{\theta}\right)} d\phi_n = \sigma_A^2 J_0\left((2\pi/\lambda)\Delta p\right). \tag{2-10}$$

In Equation (2-10), $J_0(.)$ represents the Bessel function of the zero$^{\text{th}}$ order and the first kind and the argument in the brackets is only a function of distance between two elements normalized by the wavelength of the carrier.

A more complex case can be studied where, instead of only the azimuth plane, the signal is uniformly spread over a sphere. For this case Van Trees (2002) describes the total signal received in the antenna as

$$s(t,\mathbf{p}) = \int_0^\pi \int_0^{2\pi} \frac{\sin\theta}{4\pi} ds_0(t,\theta,\phi)e^{-j\tau(2\pi/\lambda)} d\theta. \tag{2-11}$$

The correlation between the outputs of the antenna at two spatially distributed points can be explained by

$$C(\Delta p) = E\left\{ds_0(t,\theta_1,\phi_1)ds_0^*(t,\theta_2,\phi_2)\right\} = \frac{4\pi\sigma_A^2}{\sin\theta}\delta(\theta_2-\theta_1)\delta(\phi_2-\phi_1). \tag{2-12}$$

$C(\Delta p)$ can further be manipulated to yield (Broumandan 2009)

$$C(\Delta p) = \frac{\sin\left((2\pi/\lambda)\Delta p\right)}{(2\pi/\lambda)\Delta p}. \tag{2-13}$$

Figure 2-10 shows the absolute values of the correlation coefficient corresponding to the two discussed scatterer models.
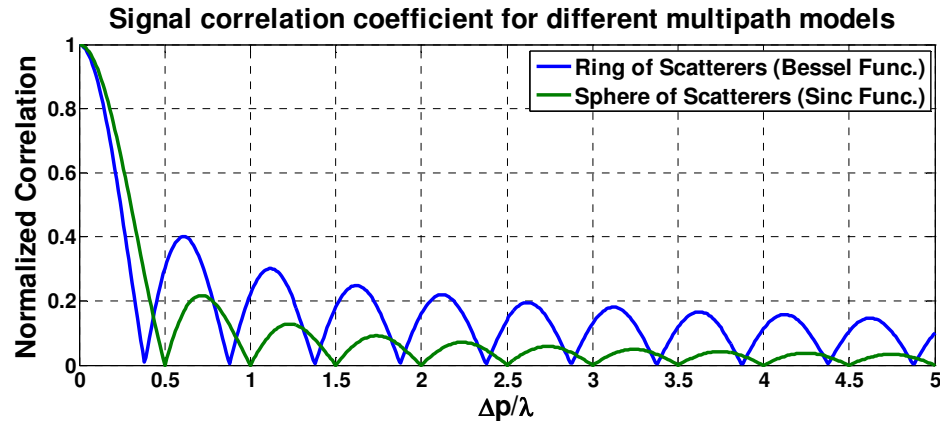
**Figure 2-10: Comparison of correlation functions under different scatterer models**

As can be seen in Figure 2-10, under the assumption of multiple incoming plane waves, the signals decorrelate at half a wavelength.

## 2.6 Signal envelope models

A microwave propagation channel can be modeled by considering its random complex gain, which possesses a circular Gaussian distribution. The following sections describe such distribution models.

### 2.6.1 Rayleigh distribution

The Rayleigh distribution is commonly used to describe the envelope of the magnitude of two orthogonal components of a complex signal in wireless fading channels where the LoS component is either very weak or unavailable (Blauntstein & Andersen 2002). It is the mathematical form to represent the PDF of $x = \sqrt{I^2 + Q^2}$, where $I$ and $Q$ are described with an independent zero mean Gaussian distribution that implicates that both have a variance of $\sigma^2$. It must be noted that the I and Q are the in-phase and quadrature-phase components of the signal. The PDF of such a distribution is described as

$$p(x) = \begin{cases} \dfrac{x}{\sigma^2} e^{\left(-\frac{x^2}{2\sigma^2}\right)} & \textit{for } x > 0 \\[2em] 0 & \textit{for } x < 0 \end{cases} \qquad\qquad \textbf{(2-14)}$$

The maximum value of a Rayleigh PDF is $e^{-1/2}/\sigma$ and occurs at $x = \sigma$. Also, by taking the first moment of the Rayleigh PDF, its mean value can be found from Papoulis & Pillai (2002) as

$$\mu_x = E\{x\} = \int_0^\infty xp(x)dx = \sqrt{\frac{\pi\sigma^2}{2}} \approx 1.25\sigma \qquad\qquad \textbf{(2-15)}$$

Also Blauntstein & Andersen (2002) show that the variance of a random variable described by the Rayleigh PDF is determined from $\sigma^2(x) = \sigma^2(2 - \pi/2)$. The Root Mean Square (rms) value of a Rayleigh PDF is $\sqrt{2}\sigma$.

### 2.6.2 Rician distribution

In many wireless channels both the LoS and NLoS signal components coexist. Unlike the Rayleigh fading channel, in this case the two quadrature components of the received signal are no longer zero mean and, therefore, the Rician distribution is used to explain the signal envelope in such a channel. The Rician distribution is derived mathematically as the PDF of $x = \sqrt{I^2 + Q^2}$, where $I \sim N(\mu_1, \sigma^2)$ and $Q \sim N(\mu_2, \sigma^2)$. The PDF of $x$ is expressed as

$$(2\text{-}16)$$

$$p(x) = \begin{cases} \dfrac{x}{\sigma^2} e^{\left(-\frac{x^2+\mu^2}{2\sigma^2}\right)} I_0\left(\dfrac{\mu x}{\sigma^2}\right) & for\ x > 0 \\ 0 & for\ x < 0 \end{cases}$$

where $\mu = \sqrt{\mu_1^2 + \mu_2^2}$ and $I_0(.)$ is the modified Bessel function of the first kind and zero$^{th}$ order, formulated as (Kay 1998)

$$I_0(y) = \frac{1}{2\pi}\int_0^{2\pi} e^{(y\cos x)} dx .$$ **(2-17)**

Figure 2-11 shows such distribution for different values of $\sigma$ and $\mu$. To quantize the effect of the LoS and Multipath components on the received signal envelope, the K-factor is defined for the Rician distribution as the relative power of the LoS signal to that of the multipath components as

$$(2\text{-}18)$$

$$K = \frac{LoS\ signal\ power}{Multipath\ components\ power} = \frac{\mu^2}{2\sigma^2} .$$

Investigating the plots in Figure 2-11 reveals that high K-factor envelopes resemble a Gaussian distribution while the signal envelopes with the lower K-factor approach a Rayleigh distribution.

## 2.7 Angle of arrival and angular spread

As mentioned earlier, the diffraction and reflection phenomena cause multiple signals to arrive at the receiver from different angles. The first part of this section describes the definitions of AoA and angle spread along key assumptions. The second

part describes several distributions that have been used in the literature to model the angular spread profile.
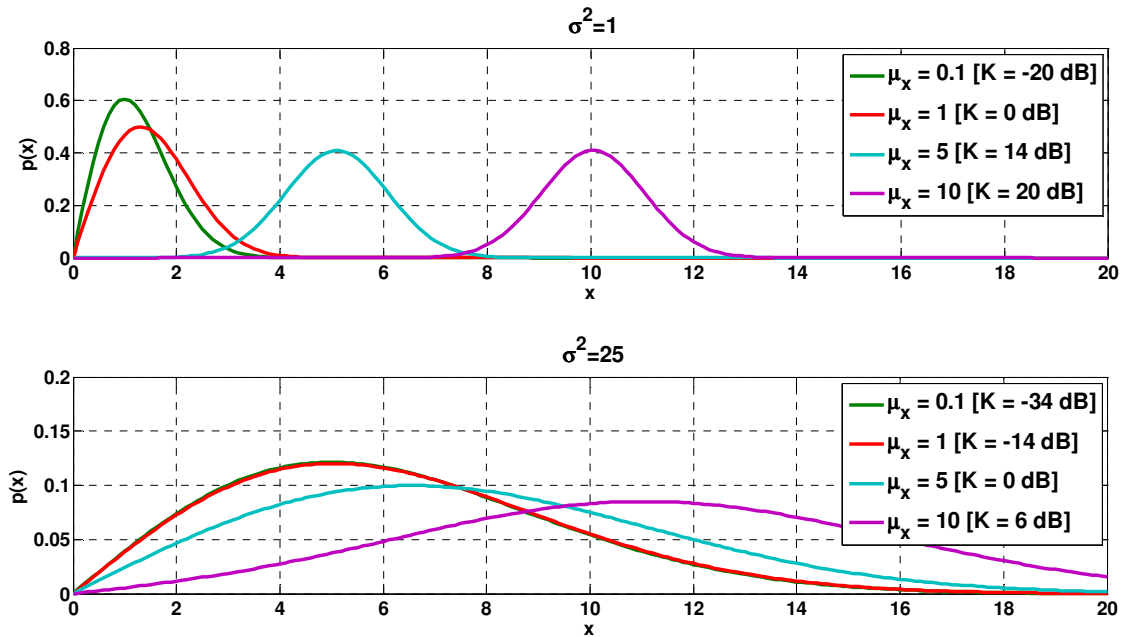


**Figure 2-11: Rician distribution**

### 2.7.1 AoA and AS definitions and assumption

As shown in Figure 2-12, the mean elevation of arrival and azimuth of arrival are shown with bold yellow arrows. Also Angular Spread (AS) is defined as the angular distance (along azimuth of elevation) where signal hotspots are spread. In other words, AS is equal to the maximum angle (azimuth or elevation) of the arriving signal minus the minimum one. However, depending on the source's SNR, the type of obstacles and the surrounding environment, the AoA may have different distribution patterns. Moreover, azimuth of arrival and elevation of arrival can be assumed to be independent of each other since they are functions of the satellite-receiver geometry and GPS satellites are widely spread in the sky. Also Yong & Thompson (2005) state the distribution of AoA

along azimuth and elevation can be considered as independent of each other and, therefore, the joint PDF of AS can be simplified to

$$p(\theta,\phi) = p(\theta)\,p(\phi) \tag{2-19}$$

where $\theta$ and $\varphi$ denote polar and azimuth angles respectively. At this step, to evaluate the mathematical foundation of the array performance and the signal characteristics under multipath, it is assumed that the signal is arriving with a mean value of $\theta_0$ and $\phi_0$ and is uniformly distributed between the maximum and minimum values of $\theta_0 \pm \theta_S / 2$ and $\phi_0 \pm \phi_S / 2$ respectively, as shown in Figure 2-12.
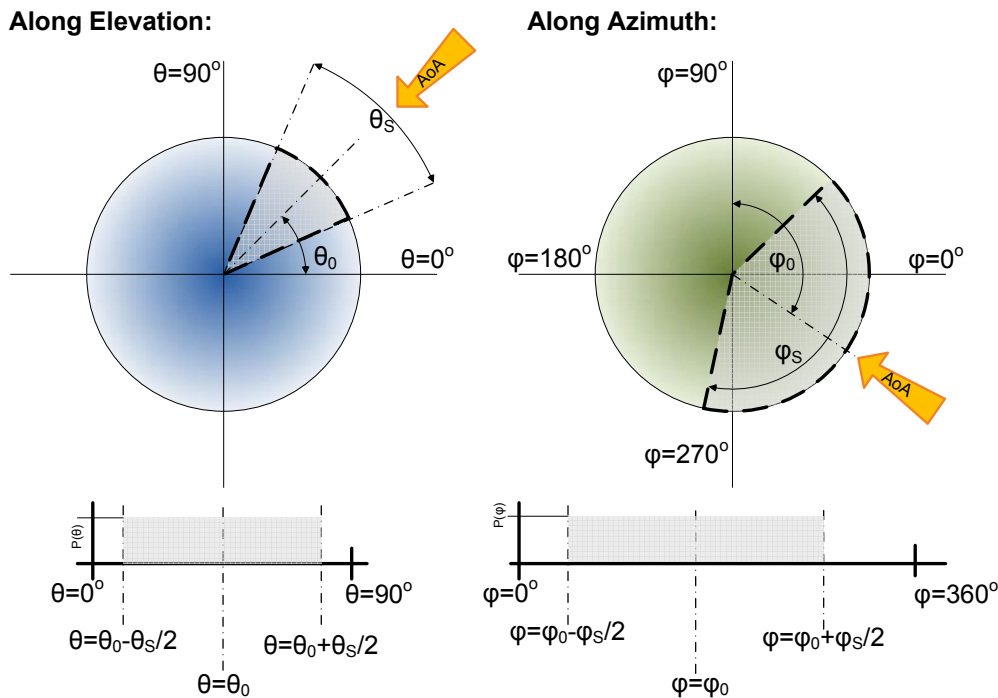
**Figure 2-12: Schematic representation of AoA and AS along elevation and azimuth**

It must be noted that in the case of Uniform Planar Arrays, due to the symmetry characteristics of the array, the mean azimuth of arrival ($\phi_0$) does not affect the array performance (In contradiction with linear or non-symmetric arrays in which the array performance and resolution changes with mean azimuth of arrival). However, mean

elevation of arrival ($\theta_0$), azimuth spread and elevation spread affect the performance of the system via spatial the correlation function between the elements (Broumandan 2009, Freidlander & Sherzer 2006, Yong & Thompson 2005).

### *2.7.2 Angular Spread models*

Many researchers have proposed different models for AoA and Angular Spread (AS) to describe the distribution (or PDF) of AoAs. AoA measurements by Spencer (1996, 2000) and Akgul & Pahlavan (2010) for an indoor communication channel within the frequency range of 7 GHz revealed that the AS has a Laplacian distribution. Another common angular spread profile (Zhou et al 2004, Yong & Thompson 2005) includes Uniform and Gaussian PDFs. Beside these well known models, Parsons (2000) and Bluantstein & Andersen (2002) have cited another model, namely the Clark model, which is formulated via normalized sine and cosine functions. A comparison of these distributions with identical variance is shown in Figure 2-13. Table 2-2 summarizes the mathematical and statistical properties of these models. By comparing the profile of Aulin's model with uniform distribution, one can easily infer that these models are almost identical to each other. When dealing with the Clark and Aulin models, extra caution in using proper and consistent angle units must be applied.

### 2.8 Summary

In this Chapter, a brief review of GPS signal structure, relevant topics on GPS signal processing and an overview of the multipath phenomenon were presented. In addition, the effect of the multipath models (ring or sphere of scatterer) on the correlation coefficient of the array samples was derived and illustrated. Consequently, the signal envelope models and their mathematical representation were presented. AoA and angular

spread concepts were introduced and the mathematical formulations of several AoA profiles were discussed. The angular spread will affect the performance of array (Andersen & Pedersen 2002) and the type or PDF of AS will be considered in deriving mathematical equations of deriving signals' correlation coefficients in Chapter 4.
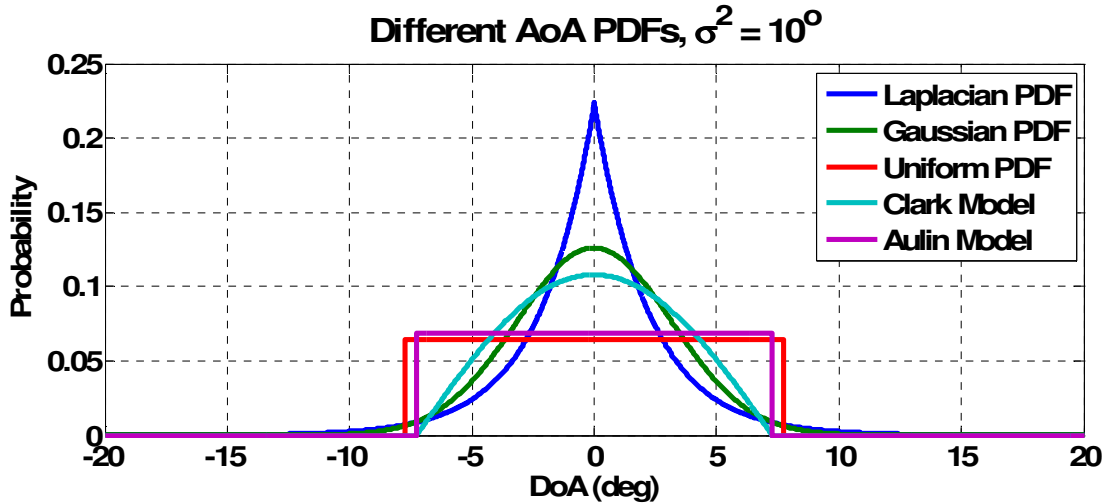


**Figure 2-13: Common angular spread models**

**Table 2-2: Comparison of different angular spread models**

| Distribution model | Mathematical representation | Variance | Mean |
|---|---|---|---|
| Uniform distribution | $p(\theta) = \begin{cases} \dfrac{1}{2\theta_s} & \theta_0 - \theta_s < \theta < \theta_0 + \theta_s \\ 0 & else \end{cases}$ | $\sigma_\theta^2 = \dfrac{\theta_s}{3}$ | $\theta_0$ |
| Gaussian distribution | $p(\theta) = \dfrac{1}{\sqrt{2\pi\sigma^2}} e^{\left(-\frac{(\theta-\theta_0)^2}{2\sigma^2}\right)}$ | $\sigma_\theta^2 = \sigma^2$ | $\theta_0$ |
| Laplacian distribution | $p(\theta) = \dfrac{1}{2b} e^{\left(-\frac{|\theta-\theta_0|}{b}\right)}$ | $\sigma_\theta^2 = 2b^2$ | $\theta_0$ |
| Clark's model | $p(\theta) = \begin{cases} \dfrac{\pi}{4\theta_s}\cos\left(\dfrac{\pi}{2}\times\dfrac{\theta}{\theta_s}\right) & \theta_0 - \theta_s < \theta < \theta_0 + \theta_s \\ 0 & else \end{cases}$ | $\sigma_\theta^2 = 2\theta_s^2\left(\dfrac{\pi^2-8}{\pi^2}\right)$ | $\theta_0$ |
| Aulin's model | $p(\theta) = \begin{cases} \dfrac{\cos\theta}{\sin\theta_s} & \theta_0 - \theta_s < \theta < \theta_0 + \theta_s \\ 0 & else \end{cases}$ | $\sigma_\theta^2 \approx \dfrac{\theta_s}{3}$ | $\theta_0$ |

**Chapter Three: Array Processing Methods**

This Chapter deals with the fundamentals of array processing techniques and their applications to GNSS. The complex signal model adopted for the array processing is presented. The complex signal in this case is the correlation peaks at the output of the software receiver. Then, in Section 3.2, similarities and differences between the signal model in the physical and synthetic arrays along with the model of a moving GNSS antenna are discussed and the methods to apply the physical array processing techniques to the synthetic arrays are presented. Sections 3.3 and 3.4 discuss the AoA estimation and beamforming methods in detail, while briefly illustrating the connection between beamforming and coherent integration. Section 3.5 introduces the concepts of Array Gain and Array Gain pattern. In addition, the effects of different array parameters such as the number of elements, array geometry and the antenna element gain pattern on the overall array gain pattern are described. The detailed mathematical formulation will be derived in Chapter 4, where the phase wrap-up phenomenon in synthetic uniform circular arrays is discussed.

**3.1 Signal model in physical arrays**

In this section a quick review of antenna arrays and their corresponding signal models are presented. The received signal in a physical array can be modeled by

$$\mathbf{s}(t, \mathbf{p}) = \begin{bmatrix} s(t, \mathbf{p_0}) & s(t, \mathbf{p_1}) & \dots & s(t, \mathbf{p_{M-1}}) \end{bmatrix}^T \tag{3-1}$$

where $s$ is the prompt correlator output for each element at time $t$ (Lin et al 2009) and $\mathbf{p_i}$ denotes the position of each element of the array. If the incoming signal is a plane wave coming from direction $\mathbf{a}$ and $s(t)$ is the received signal at the origin of the array, then the

received signal at each element of the array defined by Equation (3-1) will be simplified

to

$$\mathbf{s}(t,\mathbf{p}) = \begin{bmatrix} s(t-\tau_0) & s(t-\tau_1) & \dots & s(t-\tau_{M-1}) \end{bmatrix}^T \tag{3-2}$$

where $\tau_i$ is the phase delay associated with each element of the array and can be

represented by

$$\tau_i = \mathbf{a}^T \mathbf{p}_i \big/ c \tag{3-3}$$

where $\mathbf{a}$ is the unit vector in the direction of incoming signals (defined in Figure 3-1) and

$$\mathbf{a} = \begin{bmatrix} -\sin\tilde{\theta}\cos\phi & -\sin\tilde{\theta}\sin\phi & \cos\tilde{\theta} \end{bmatrix}^T \tag{3-4}$$

where $\tilde{\theta}$ and $\phi$ are the elevation and azimuth angles of the arriving signal respectively,

while $\mathbf{p}_i$ is the 3x1 position vector of each element in a local coordinate system with

respect to the reference point of the array as shown in Figure 3-1.
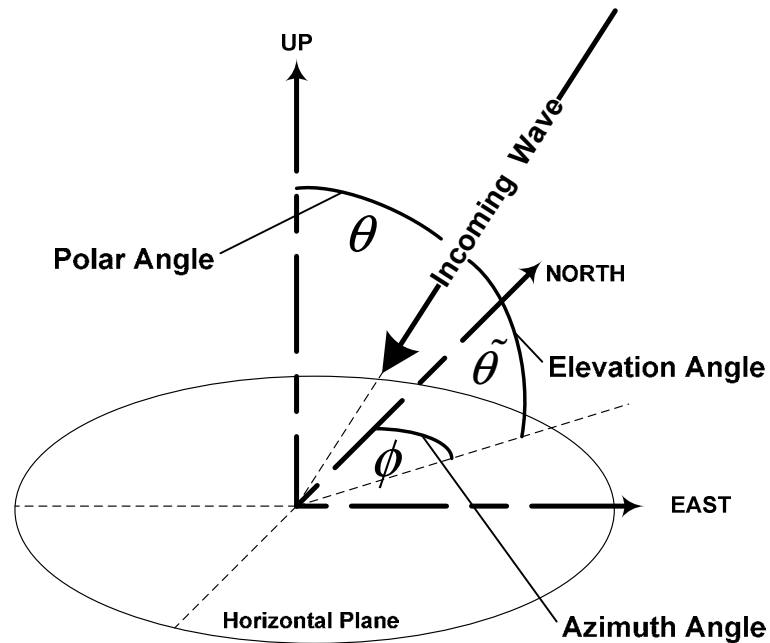


**Figure 3-1 Polar coordinates, AoA, azimuth and elevation angles definitions**

Furthermore, the wave number vector, which represents the phase change of the signal per unit length of distance, can be defined by Van Trees (2002) as

$$\mathbf{k} = \left( \omega / c \right) \mathbf{a} = \left( 2\pi / \lambda \right) \mathbf{a}$$
(3-5)

The term $\omega \tau_i$ can be introduced, which for the case of UCA where $\mathbf{p}_i = \left( R \sin \gamma_i \quad R \cos \gamma_i \quad 0 \right)$, is

$$\omega \tau_i = \mathbf{k} \mathbf{p}_i = \frac{2\pi R}{\lambda} \sin \tilde{\theta} \cos \left( \phi - \gamma_i \right)$$
(3-6)

In Equation (3-6), $\gamma_i$ is the angular distance of the $i^{th}$ element with respect to the element that is aligned to the north, expressed as $\gamma_i = 2\pi i / M$ where $i$ varies from 0 to *M-1*. This term defines the relative delay between array elements with respect to a signal that is coming from a specific direction of $(\tilde{\theta}, \phi)$. Based on this relative delay, the array manifold vector or the steering vector can be defined for the case of a UCA as (Zoltowski & Mathews 1993)

$$\mathbf{v} = e^{\left( \frac{2\pi jR}{\lambda} \sin \tilde{\theta} \cos(\phi - \gamma_0) \quad \frac{2\pi jR}{\lambda} \sin \tilde{\theta} \cos(\phi - \gamma_1) \quad \cdots \quad \frac{2\pi jR}{\lambda} \sin \tilde{\theta} \cos(\phi - \gamma_{N-1}) \right)}$$
(3-7)

An array manifold vector is an important parameter in array processing and the majority of AoA finding and beamforming methods employ this parameter as a measure of the geometrical properties of the array versus the designated target.

## 3.2 GNSS signal model in synthetic arrays

In a synthetic array scenario, instead of using several antenna elements, discrete samples are generated by integrating the signal at different times in a moving antenna.

Let $\mathbf{p}[m]$, $m \in [0:M-1]$ denote the position vector of the phase center of the moving GNSS antenna as a function of discrete-time samples, $m$, relative to a three dimensional rectangular coordinate system. The complex baseband signal representation of the antenna output received signal is denoted as $r[m]$ and is described in Section 2.3. The signal component of $r[m]$ emanating from the $k$-th satellite is denoted as $s_k\left[m, p[m]\right]$ and is a function of $m$ and the changing antenna position $p[m]$. The received signal is corrupted with additive noise, which has an equivalent complex baseband representation denoted by $\eta[m]$. It is assumed that $\eta[m]$ is a complex normal random process, independent of the signal and has a power spectral density (PSD) with a level of $N_o$. The representation of $r[m]$ in each snapshot can then be expressed as

$$r[m] = S[m] + \eta[m], \quad m = 0,...,M-1 \tag{3-8}$$

where

$$S[m] = \sum_{k=1}^{K} A_k\left(\mathbf{p}[m]\right) D_k(m-\tau_k) c_k(m-\tau_k) e^{j(2\pi \Delta f_k t[m] + \psi_k)}, \quad m=0,...,M-1 \tag{3-9}$$

.

$A_k\left(\mathbf{p}[m]\right)$ is the complex channel gain as a function of the antenna position $\mathbf{p}$ relative to a fixed local coordinate system and the rest of the structure in Equation (3-9) is described in Section 2.3 and 2.4 while $K$ is the number of satellites in view and $n[m]$ contains complex additive white Gaussian noise samples. Herein, the signal processing of individual GNSS satellites is considered. Therefore, interference from other GNSS satellites is assumed to be negligible compared to other dominant independent noise sources. Hence, in the remainder of the text for notational convenience the subscript of $k$

is ignored and the received signal is modeled as $r[m] = s[m]e^{j(2\pi\Delta ft[m]+\psi)} + \eta[m]$

where $s[m] = D(m-\tau)c(m-\tau)$ is known to the receiver.

The main topic of the current research is to characterize the AoA of GNSS signals under multipath conditions using array processing methods. Therefore, to estimate the AoA of incoming signals and investigate the performance of beamforming in fading environments using physical array formulations, it is essential to discriminate the received signal phase variation due to the receiver motion from satellite motion and clock drift. Consider a moving antenna scenario similar to that shown in Figure 3-2.
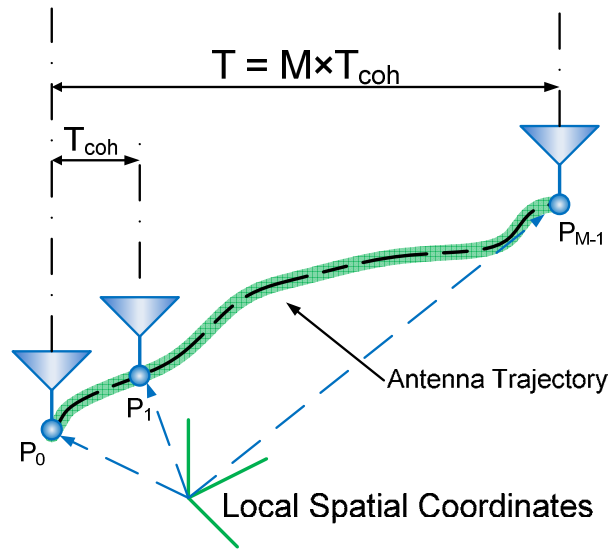


**Figure 3-2: Moving antenna trajectory during one signal snapshot**

The coordinate system of interest was shown in Figure 3-1 where $\phi$ is the azimuth angle measured from the x axis and $\theta$ is the polar angle with respect to the z axis. The m-th sample point is denoted as $\mathbf{p}_m$, which is a positional vector in the $\{\mathbf{x}, \mathbf{y}, \mathbf{z}\}$ coordinate frame. The set of $M$ element positions during each snapshot is denoted by

$$\mathbf{p} = \begin{bmatrix} \mathbf{p_0} \cdots \mathbf{p}_{M-1} \end{bmatrix}^T . \tag{3-10}$$

The signal received at $M$ spatial/temporal sampling points in each snapshot is denoted as

$$\mathbf{s}[\mathbf{t},\mathbf{p}] = \begin{bmatrix} s[t_0,\mathbf{p}_0], \dots, s[t_{M-1}, \mathbf{p}_{M-1}] \end{bmatrix}^T . \tag{3-11}$$

Consider a propagation scenario of a satellite signal in the direction of $\mathbf{a}$ which is characterized by the polar and azimuth angles. If $s[m]$ is the signal received at the origin of the coordinate system at time $m$, then Equation (3-11) reduces to

$$\mathbf{s}[m,\mathbf{p}] = \begin{bmatrix} s(m-\tau_0), \dots, s(m-\tau_{M-1}) \end{bmatrix}^T \tag{3-12}$$

where

$$\tau_m = \frac{\mathbf{a}^T \cdot \mathbf{p_m}}{c} + \tau_{other} . \tag{3-13}$$

$\mathbf{a}$ is a direction vector defined in Section 3.1 by

$$\mathbf{a} = - \begin{bmatrix} \sin(\tilde{\theta})\cos(\phi) \\ \sin(\tilde{\theta})\sin(\phi) \\ \cos(\tilde{\theta}) \end{bmatrix}, \tag{3-14}$$

$c$ is the propagation speed, $\lambda$ is the carrier wavelength and $\mathbf{t} = \begin{bmatrix} t_0 .. t_{M-1} \end{bmatrix}^T$ is a uniform time sampling vector at each snapshot. The first and second terms in Equation (3-13) consider the delay due to the antenna position $\mathbf{p}(t)$, and satellite-antenna motion and clock instability respectively. As can be seen, the first part of Equation (3-13) is common between synthetic and physical arrays and the second introduced delay is caused by the motion of the mobile antenna, the clock drift and other phase corrupting phenomena such as phase wrap-up that will be discussed in Section 4.2. It is assumed that $s[m,\mathbf{p}_m]$ is a band pass signal that for the narrowband case and reduces to

$$s[m, \mathbf{p}_m] = \sqrt{2} \, \text{Re}\left\{\tilde{s}[m]e^{j\omega_c t[m]}e^{-j\omega_c \tau_m}\right\}, \qquad m = 0, ..., M - 1. \tag{3-15}$$

In the narrowband signal model, the propagation delay due to $\tau_{other}$ is approximated by a phase shift. It can be shown that the propagation phase difference in Equation (3-15) is a function of the propagation vector, antenna position and Doppler due to antenna motion and clock drift:

$$\omega_c \tau_m = 2\pi\left(\frac{\mathbf{a}^T \mathbf{p_m}}{\lambda} + f_{sat}\tau_{other}[m]\right). \tag{3-16}$$

Thus, Equation (3-15) becomes

$$s[m, \mathbf{p}_m] = \sqrt{2} \, \text{Re}\left\{\tilde{s}[m]e^{j\omega_c t[m]}\exp\left(-j2\pi\left(\frac{\mathbf{a}^T \mathbf{p_m}}{\lambda} + f_{sat}\tau_{other}[m]\right)\right)\right\}. \tag{3-17}$$

, $\quad m = 0, ..., M - 1$

Specifically for the incident plane wave, corresponding to a propagation vector $\mathbf{a}$, the signal outputs of the antenna during the snapshot become

$$\mathbf{s}[m, \mathbf{p}] = s[m]\mathbf{v}[\mathbf{a}] \tag{3-18}$$

where $\mathbf{v}[\mathbf{a}]$ is denoted as

$$\mathbf{v}[\mathbf{a}] = \begin{bmatrix} \exp\left(-j2\pi\left(\frac{\mathbf{a}^T \mathbf{p}_0}{\lambda} + f_{sat}\tau_{other}[0]\right)\right) \\ \vdots \\ \exp\left(-j2\pi\left(\frac{\mathbf{a}^T \mathbf{p}_{M-1}}{\lambda} + f_{sat}\tau_{other}[M-1]\right)\right) \end{bmatrix}. \tag{3-19}$$

As stated before, $\tau_{other}$ emerges from different sources such as the receiver clock instability and satellite motion and these delays are not accounted for in physical array formulations. Several methods can be implemented to remove such additional delays.

Lin et al (2009) use a linear trend interpolation to wipe off these delays for short periods of time. To do so precisely, side information such as satellite ephemeris, initial position and velocity vector, and clock stability parameters are necessary to estimate the slope of the linear interpolation.

On the other hand, another option is to use the signal of a nearby static antenna that is connected to the same receiver. The signal received from this antenna provides $f_{sat}\tau_{other}[m]$ accurately for each epoch and therefore, by subtracting the static antenna signal from the signal of mobile antenna, the unwanted delays can be removed. To compare the proposed two options, one should keep in mind that $f_{sat}\tau_{other}[m]$ (especially due to clock instability) is not constant and changes with time and therefore the estimated linear trend is reliable for a few minutes. On the other hand, the second method that uses auxiliary reference signals from a static antenna brings superior accuracy and computational efficiency. However, it has limited practical usages and is almost impossible to implement in stand-alone receivers. Since the context of the current research is to develop a synthetic antenna array to characterize GNSS channels and evaluate the performance of such systems, the latter option is used. Therefore, it is assured that the errors are only due to the array system and have not emerged from poor measurements or estimation of the satellite motion or clock drift.

## 3.3 Beamforming methods

The main concept of beamforming is to create a vector of complex weights based on the array manifold vector to weight each array element, in order to steer the main lobe of the array towards a desired direction. There are many different types of beamforming

methods; however, in this research only the Delay and Sum method is employed. The main idea behind beamforming is shown in Figure 3-3.
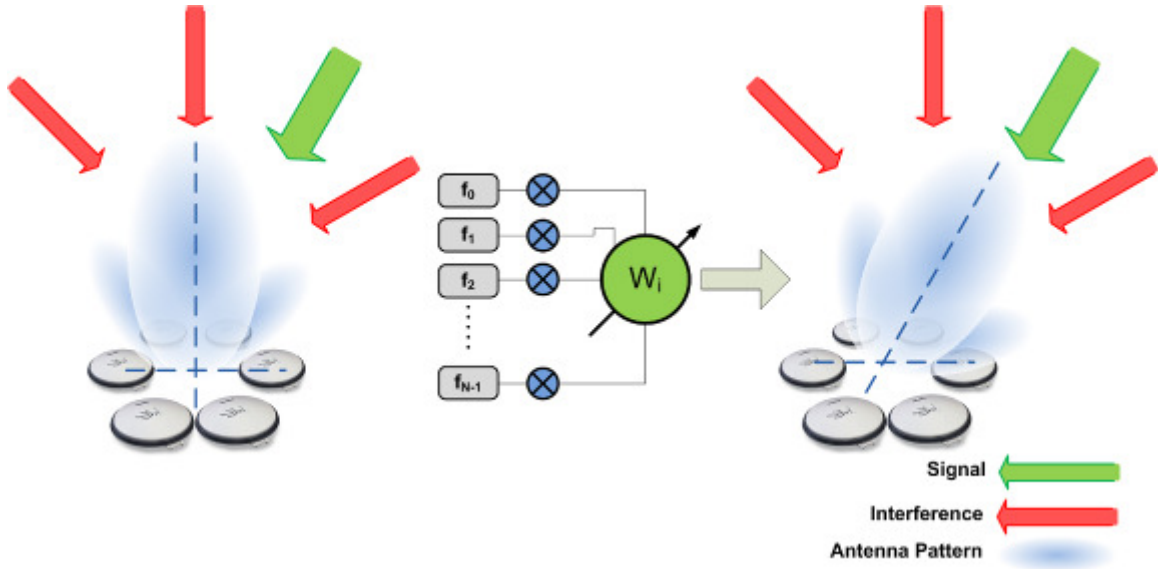


**Figure 3-3: Beamforming concept**

### *3.3.1 Delay and Sum Method*

The Delay and Sum method is the conventional concept in beamforming. The main idea behind it is to coherently add the weighted arriving signals through all elements, so that the entire array points towards a known direction. The time response of such a filter is

$$h_m(\tau) = \frac{1}{M}\delta(\tau + \tau_m).$$

(3-20)

By converting Equation (3-20) to a frequency domain and expressing the $\tau_n$ delays in terms of the desired direction and position of each element, the weighting function corresponding to the delay and sum beamformer can be written in terms of the array manifold vector (Van trees 2002) as

$$\mathbf{w}^T = \frac{1}{N}\left(\mathbf{v}(\mathbf{k})\right)^H \tag{3-21}$$

where $\mathbf{w}$ is the complex weight vector and satisfies the distortionless constraint which is

$$\left|\mathbf{w}^H \mathbf{v}\right|^2 = 1 \tag{3-22}$$

Furthermore, the expanded form of multiplying $\mathbf{w}$ from Equation (3-21) into the

received signal $r[m] = s[m]e^{j(2\pi\Delta f_D t[m]+\psi)} + n[m]$ results in

$$b[m] = v[m].r[m] = e^{\left(-j2\pi\left(\mathbf{a}^T \mathbf{p}_m / \lambda\right)\right)}\left(s[m]e^{j(2\pi\Delta f_D t[m]+\psi)} + \eta[m]\right). \tag{3-23}$$

It will be shown in Section 4.2.3 that $\Delta f_D$ is equal to $\mathbf{a}^T \mathbf{p}_m / \lambda$ and this makes

Equation (3-23) equal to Equation (3-9). In other words, beamforming and coherent

integration can be thought of as two equal methods for increasing the SNR and in fact the

processing gain concept is identical to the array gain concept. The only difference is that

the latter takes advantage of the spatial information of the antenna element position to

form the beam towards the desired direction.

## 3.4 AoA Finding

One of the main applications of antenna arrays is finding the direction of the

arriving signal. Generally, there are three major AoA estimation methods: Conventional,

subspace and maximum likelihood (Allen & Ghavami 2005).

### 3.4.1 Beamscan Method

The Beamscan method, also known as the Fourier Method (Allen & Ghavami

2005), is the classical method for finding a signal's AoA using antenna arrays. Its

fundamental concept is to scan the entire field of view (also known as the search space –

Azimuth: 0-360° and Elevation 0-90°) and measure the signal's power at each Azimuth and Elevation. The measurement for each element of the search space will be performed via the dot product of signals with an array manifold vector (Lin et al 2009, Van trees 2002, Allan & Ghavami 2005) as

$$b\left(\theta_i, \phi_j\right) = \mathbf{s(p)}^* \mathbf{v}\left(\theta_i, \phi_j\right)$$ 
(3-24)

where $b$ is the AoA spectrum, $\mathbf{s(p)}$ is the signal as captured from elements located at $\mathbf{p_0}$ to $\mathbf{p_{N-1}}$ and $\mathbf{v}\left(\theta_i, \phi_j\right)$ is the array manifold of the array along each search space element $(0 < \theta_i < \pi/2, 0 < \phi_j < 2\pi)$. By inspecting the plot of $b$ along both directions, the AoA can be found by associating the peaks of $b$ to the corresponding angles. The resolution of this method is limited by the Rayleigh resolution (Van Trees 2002). Therefore, it has a lower performance in the presence of the multipath signals.

## 3.5 Array Gain, Array Gain Pattern and Beamwidth

As for conventional antennas, each antenna array is associated with a gain, gain pattern and half-power beamwidth. One of the primary applications of arrays includes amplifying the signal and improving SNR by adding the signals coherently (Van Trees 2002). This feature is measured via Array Gain (AG), which is a critical parameter in evaluating an array performance and is defined to be the ratio between the array's output SNR to input SNR as

$$AG = \frac{SNR_{out}}{SNR_{in}}.$$ 
(3-25)

where $SNR_{in}$ is the signal spectrum-to-noise spectrum ratio at the output of each antenna element ($SNR_{in} = S_s / S_n$ where $S_s$, $S_n$ denote signal and spectrum respectively). The array gain for a zero mean complex random Gaussian is defined by Friedlander & Scherzer (2004) to be

$$AG = \mathbf{w}^H \mathbf{R} \mathbf{w} \tag{3-26}$$

where $\mathbf{R}$ is the covariance matrix of the array response vector. In the case of independent fading, $\mathbf{R}$ reduces to $\mathbf{R} = \mathbf{I}$. Generally when the signal is a LoS or the correlation between signal samples is high, $\mathbf{R}$ can be written as

$$\mathbf{R} = \mathbf{v}\mathbf{v}^H . \tag{3-27}$$

In this case, the rank of $\mathbf{R}$ reduces to one and then the maximum achievable theoretical array gain in dB scale will be

$$AG\big|_{dB} = 10\log_{10}(M) . \tag{3-28}$$

However, in the presence of multipath and Angle Spread (AS), the array gain will drop dramatically. Broumandan (2009) and Friedlander & Scherzer (2004) have quantized this loss for a uniform linear array. The covariance matrix of the array response for the case of a linear array (Broumandan 2009, Friedlander & Scherzer 2004) is

$$\mathbf{R} = \frac{1}{\theta_s} \int_{-\theta_s/2}^{\theta_s/2} P(\theta) \mathbf{v}(\theta) \mathbf{v}^H(\theta) d\theta \tag{3-29}$$

where $P(\theta)$ is the PDF of the signal along elevation. Furthermore, the array gain pattern is another key metric to evaluate the array performance. For a uniform circular array, the array factor can be found from (Van Trees 2002)

$$AF(\theta,\phi) = \sum_{0}^{N-1} w_n e^{\left[ j\frac{2\pi R}{\lambda}\sin\theta\cos(\phi-\gamma_i)+\beta_i \right]} \tag{3-30}$$

where $AF$ is called the array factor and $\beta_i$ is the phase factor with respect to the origin to align the main axis response of the array towards the known direction of $(\theta, \phi)$ or as defined in Equation (3-7). Finally, the array gain pattern can be computed from the product of $AF$ and the elements beam pattern (Van Trees 2002) as

$$\text{A}(\theta, \phi) = Y_e \cdot AF(\theta, \phi) \tag{3-31}$$

where $Y_e$ is the element's response function and it must be noted that this is based on the assumption that the array elements are identical, which is the case for synthetic antenna arrays. Equations (3-30) and (3-31) suggest that there are three parameters that govern the overall shape of the array gain pattern. The first parameter is the pattern of each element of the array; the second parameter is the relative size of the array in the sense of its aperture with respect to the signal carrier wavelength; and the third parameter is the number of elements in the array ($M$). Furthermore, the weighting function $w_m$ is another parameter and at this point the general model of uniform excitation is ($w_m = 1/M$). For instance, Figure 3-4 shows the 3D pattern along the elevation and azimuth of an array with a 36 cm radius (with 19 cm wave length of GPS L1 signals), 100 elements and isotropic element assumption. Equation (3-30) basically assumes that each element in the array has an isotropic pattern which is also more suitable for channel characterization and AoA finding in multipath environments since it has equal responses in all directions. However, in many actual cases, including GNSS applications and in the current research, an antenna with a non-isotropic pattern is employed. In GNSS applications the antennas are generally designed with hemispherical patterns in such a way as to amplify signals coming from higher elevation angles (Ward et al 2006a). The antenna used in this

research is a Novatel-GPS-701/702-GGL antenna and its pattern is shown in Figure 3-5 (NovAtel 2010). As can be seen in Figure 3-6, the output of such an antenna element and attenuation of signals from lower elevation angles may affect the estimated angle distribution and AS of the signals captured by the array.
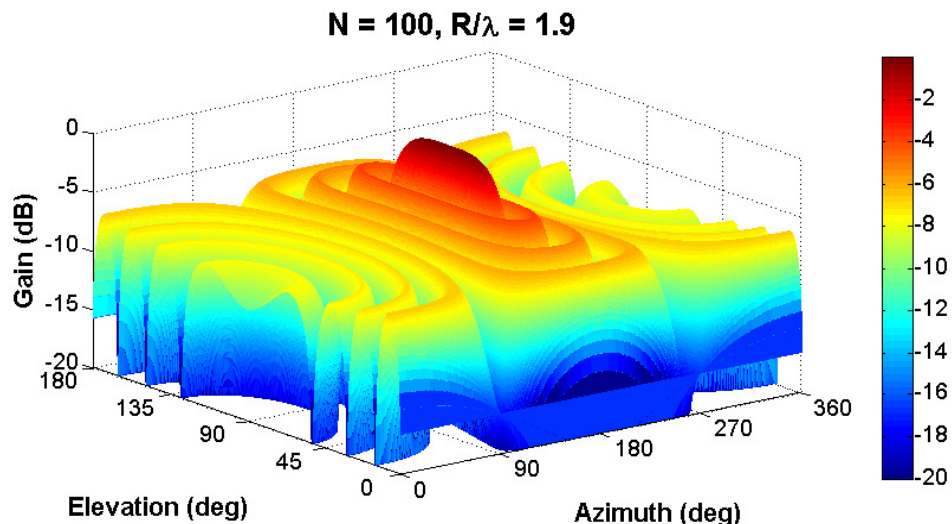


**Figure 3-4: 3D gain pattern of a UCA**
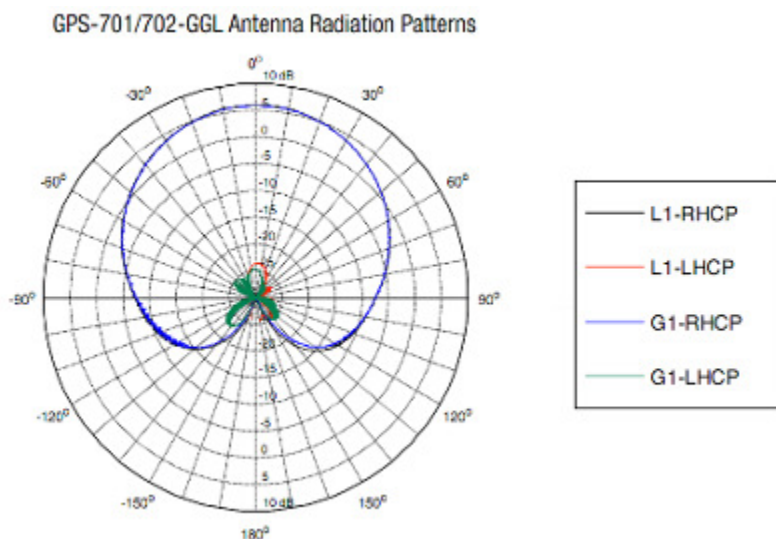


**Figure 3-5: NovAtel GPS-701 and 702 GGL series gain pattern across elevation (from http://www.novatel.com/assets/Documents/Papers/GPS-701_702-GGL.pdf, last accessed 15 March 2011)**
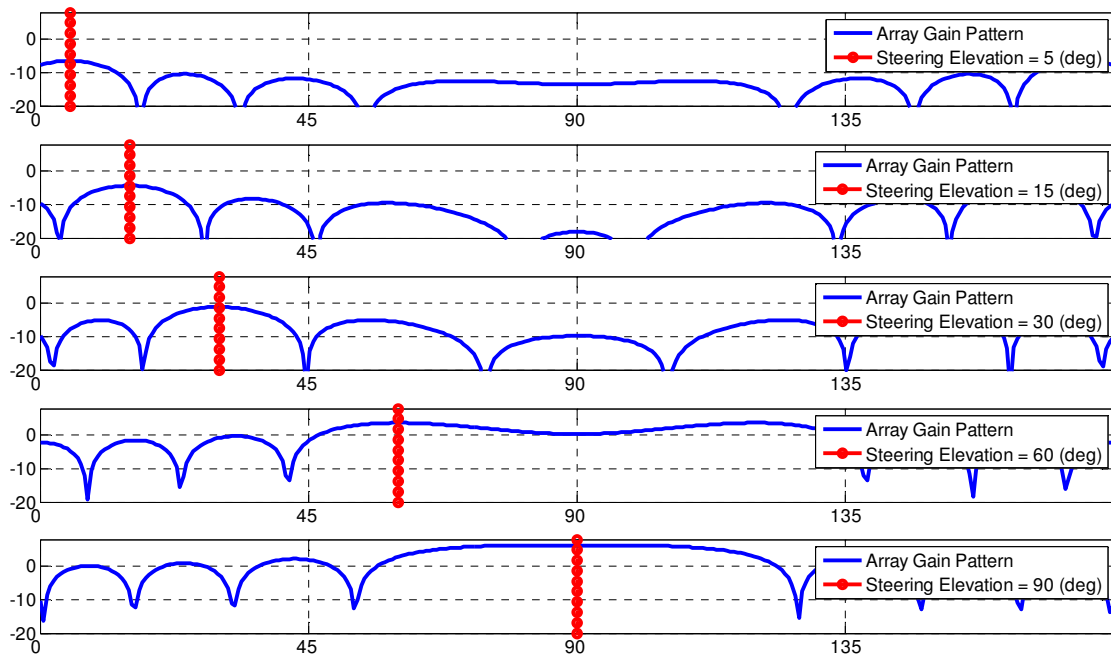
**Figure 3-6: Array gain pattern across elevation, Novatel-GPS-701/702 GGL series**

For the case of a UCA, the size of the array governs the pattern via the term $2\pi R / \lambda$. The pattern of a UCA with a certain number of elements and isotropic antenna assumption for various different radiuses is shown in Figure 3-7 where the dashed pink horizontal line shows the 3 dB threshold (Half-Power) to measure the beamwidth. It can be seen that for the same number of array elements, larger radiuses reduce beamwidth considerably and hence provide a higher resolution. As can be seen, as the distance between the elements increases, the beamwidth of the array gets narrower.
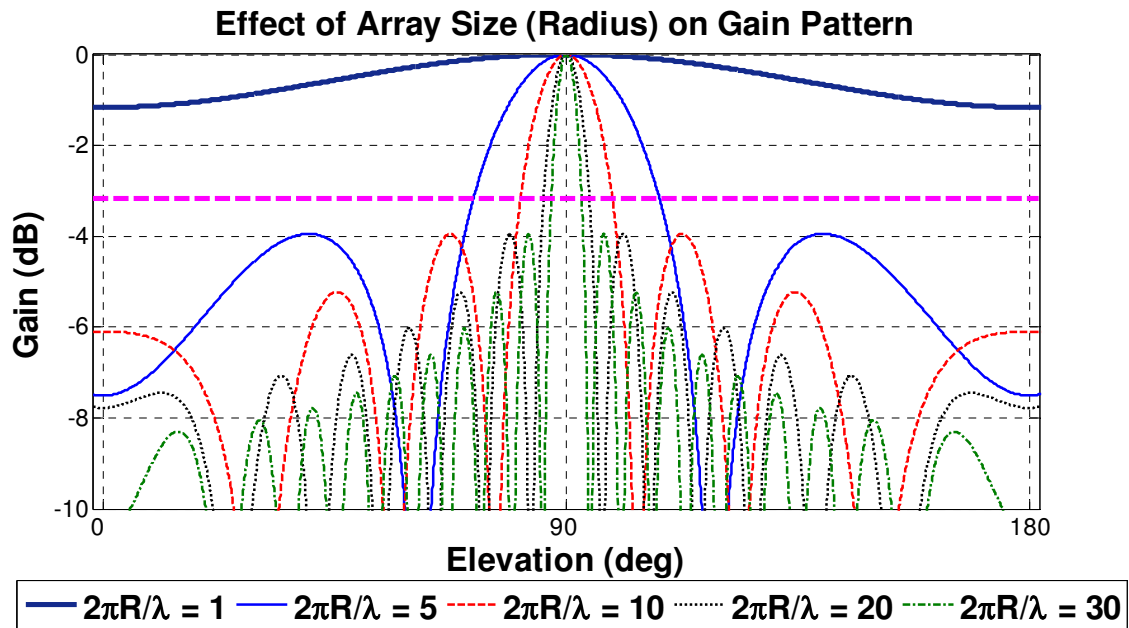
**Figure 3-7: Effect of array radius on beam pattern**

Analyzing the data for the case of a UCA with 100 elements versus various values of $2\pi R/\lambda$ ranging from 2 to 100 suggests a logarithmic trend for HPBW with respect to $2\pi R/\lambda$, which is shown in Figure 3-8. Finally, Van Trees (2002) states that, when the number of elements in a UCA is sufficiently high (e.g. greater than 20), the array gain pattern doesn't change drastically. Figure 3-9 shows this for a UCA with $2\pi R/\lambda = 10$ and various numbers of elements.

**3.6 Summary**

In this Chapter, the required fundamentals to process physical array data were discussed. Methods that can be used to apply physical array processing techniques to data collected from synthetic arrays were then presented. The next sections described the Delay and Sum and beamscan methods. Array gain and array gain pattern specifically for the case of UCAs were finally formulated.
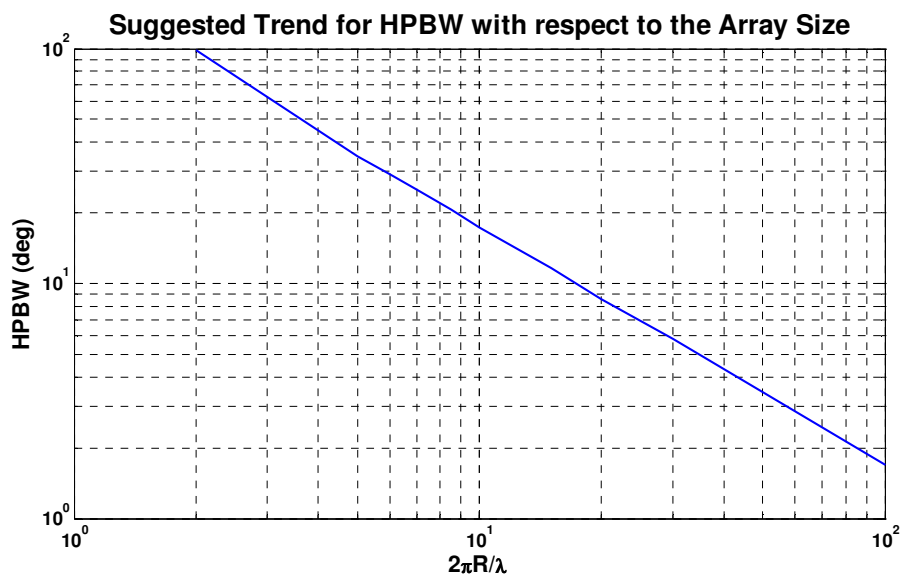
**Figure 3-8: Linear trend between the array size (radius) and half power beam width**
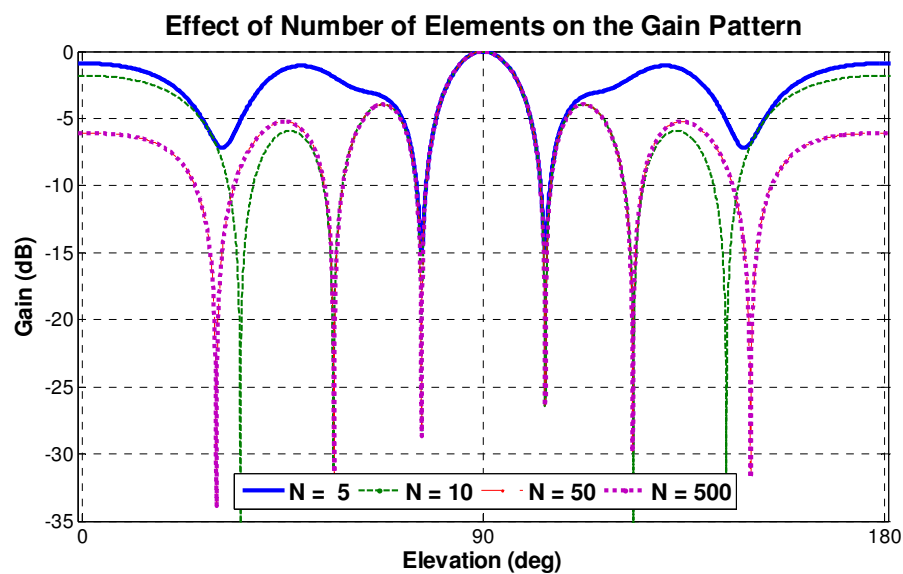


**Figure 3-9: Comparison of the gain pattern of several similar UCAs with different number of elements**

## Chapter Four: Implementation and Analysis of Synthetic Antenna Array Performance under Multipath

This Chapter covers selected advanced aspects of the implementation issues and concerns regarding synthetic array processing implementation issues that have been addressed briefly in previous sections. These include practical aspects of AoA estimation, phase wrap-up, the effect of the antenna gain pattern on the AoA profile and the array gain limitations due to multipath propagation. This chapter includes a mathematical investigation of these factors along using a data simulation analysis. First, in Section 4.1, the practical implementation of AoA and AS estimation is described. This review section helps to better understand the methodologies and results that follow in Sections 4.2, 4.3 and Chapter 5. In Section 4.2, the phase wrap-up is described in detail. The reason for including an in-depth analysis of phase wrap-up in this work is to consider its effects as an array perturbation phenomenon on the performance of AoA estimation. This section covers the basics of the signal polarization concept and its application in GNSS. Thereafter, the phase wrap-up effect for rotating antennas and for the case of a synthetic UCA is studied. In this section, the mathematical foundation to link the circular motion of the antenna to the array manifold vector employed in Chapter 3 is formulated. Finally, Section 4.2 concludes by studying this effect on array performance. Section 4.3 follows the discussion in Section 3.5 on the effect of the antenna pattern on the array gain pattern. In practice, GPS antennas are designed somehow to mitigate multipath signals arriving from low elevations. Therefore, they are designed to have lower gains at lower elevation angles. Therefore this analysis is included to address the critical effects of different antennas' gain roll-off along elevation. Three proposed antenna elements have been

employed in simulations to assess the effect of the antenna element gain pattern on the AoA profile. Finally, Section 4.4 describes the array gain under harsh multipath conditions.

## 4.1 Practical consideration of AoA estimation

This section describes the process of AoA estimation in practice. The process described here applies to both the simulated data presented in this chapter and the real GPS data that will used in the experimental tests presented in Chapter 5. The mathematical aspects of the AoA estimation are described in Equation (3-24) as

$$b\left(\theta_i,\phi_j\right)=\mathbf{s}^*\cdot\mathbf{v}\left(\theta_i,\phi_j\right) \qquad\qquad \textbf{(4-1)}$$

where $b\left(\theta_i,\phi_j\right)$ is a measure of the signal strength along the direction of $\theta_i,\phi_j$, $\mathbf{s}^*$ is the complex conjugate of the array signal and $\mathbf{v}\left(\theta_i,\phi_j\right)$ represents the array steering vector towards $\theta_i,\phi_j$. Plotting $b$ for all available angle of arrivals results in a surface that for line of sight conditions has only one single distinct peak as shown in Figure 4-1. The maximum value of this surface is considered the estimated AoA.



Single incoming signal
AoA = [45° 180°]
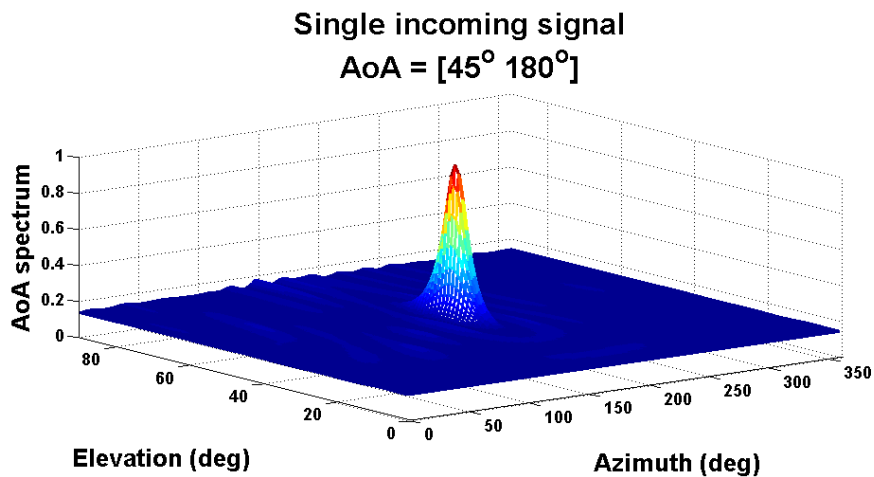
**Figure 4-1: AoA spectrum of a single ray of signal**

However, for multipath conditions, the result will not be as straightforward as LoS conditions. Each sample will have multiple peaks that are not necessarily constant with time and may alter their power from sample to sample. An example of such an AoA spectrum is shown in Figure 4-2.
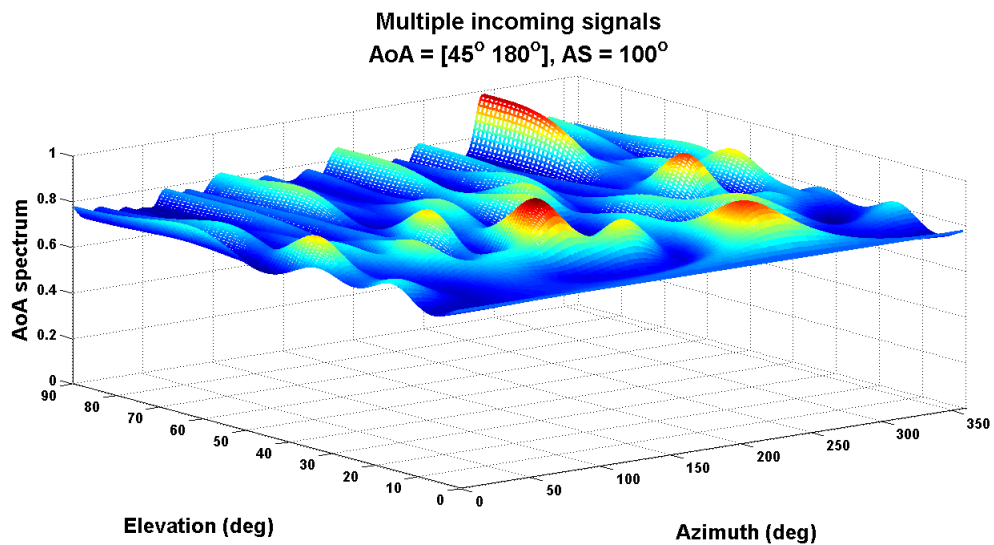


**Figure 4-2: AoA spectrum of a multiple rays of signal**

These multiple peaks may be from multipath components or might be detected from the array sidelobes. The effects of sidelobes are introduced in Section 4.3 in more detail. However, to eliminate the effect of sidelobes, a certain threshold can be considered. Therefore, the AoA spectrum is fed into an algorithm that records the azimuth, elevation and relative power of the peaks. Subsequently the peaks are filtered out after comparison to this threshold. At the next step, the selected peaks for several samples are considered all together to plot the PDF of the AoA along azimuth and elevation for further investigation.

## 4.2  Phase wrap-up

GNSS satellites provide two ranging observables to the users over Right Hand Circularly Polarized (RHCP) electromagnetic signals, namely the pseudorange and carrier phase. The broadcasted RHCP signals can be envisaged as a rotating electric field, propagating in space and can be received via RHCP antennas. At the receiver antenna side, the received signal carrier phase is equal to the instantaneous phase of the signal measured from a certain reference point on the antenna. Therefore, any axial rotations and changes in the orientation of the antenna reference point can change the received signal carrier phase and this change is called carrier phase wrap-up (AKA rotational Doppler) in the literature. A major problem with the phase wrap-up phenomenon is that it cannot be cancelled out through the "between receivers" differencing methods since this error is due to the receiver antenna and causes problems in fixing the carrier phase ambiguities (e.g. Wu et al 1993). Precise alignment of the antenna to a certain direction has been found to be a practical solution to this problem over short baselines. As can be seen in Figure 4-3, GPS antennas used for high precision applications have an indicator to fix the antenna towards a known direction such as north.

In the context of the kinematic positioning under multipath, vehicular or aviation applications or implementing synthetic array techniques in the trajectory aided navigation schemes, considering the phase wrap-up and its effect on navigation accuracy, beamforming performance and AoA finding is a must. The following sections highlight the mathematical aspects of the phase wrap-up in more depth.

**Figure 4-3: A GPS antenna with a heading indicator**

### *4.2.1 RHCP signals*

As mentioned in Section 2.2, GPS signals are electromagnetic (EM) waves that are broadcasted in the L-band and are Right-Hand Circularly Polarized (RHCP). Polarization in EM-wave propagation refers to the fixed orientation that the electric flux maintains with respect to the signal spread direction (Kraus 1988, Bisnath et al 2007). In other words, it is the direction that the tip of the electric field intensity vector traces by time. For instance, if the electric field vector lies on a plane, such as the horizontal plane, it is considered to be horizontally polarized. Horizontal and vertical polarization concepts are illustrated in Figure 4-4.

Besides the vertical or horizontal polarizations, a general case can be defined where the horizontally and vertically polarized signals with arbitrary amplitude and phase are added together to form an elliptically polarized wave. In GPS, a specific type of polarization is employed in which the EM-wave components are designed to have equal amplitudes and a $90^{\circ}$ phase difference in order to form a Right Hand Circularly Polarized

wave. In this scheme a vertical wave that is delayed $\pi / 2$ radians is added to the original horizontal component.
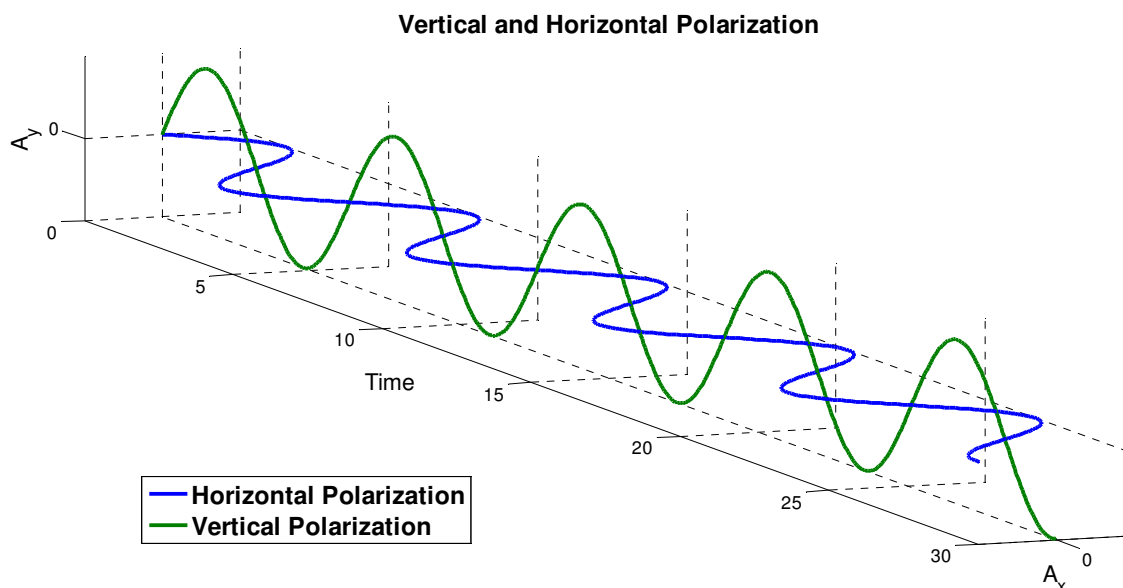


**Figure 4-4: Vertical and horizontal polarization**

The first part of Figure 4-5 illustrates the generation of RHCP waves schematically while the second part of Figure 4-5 shows the delayed component and propagation of RHCP signals in 3D space. In other words, an RHCP signal is a composite wave that has a counterclockwise rotation when observed from the receiver's point of view. One reason to employ such a technique to broadcast GNSS signals is to prevent the atmospheric effects induced by that ionosphere that alter the orientation of linearly polarized waves.

Also, unlike the linear polarized signal whose amplitude varies periodically with time, the amplitude of the circularly polarized wave has a constant value over a period of time. Circular polarization also negates the importance of the antenna orientation with respect to the orientation of the signal source.
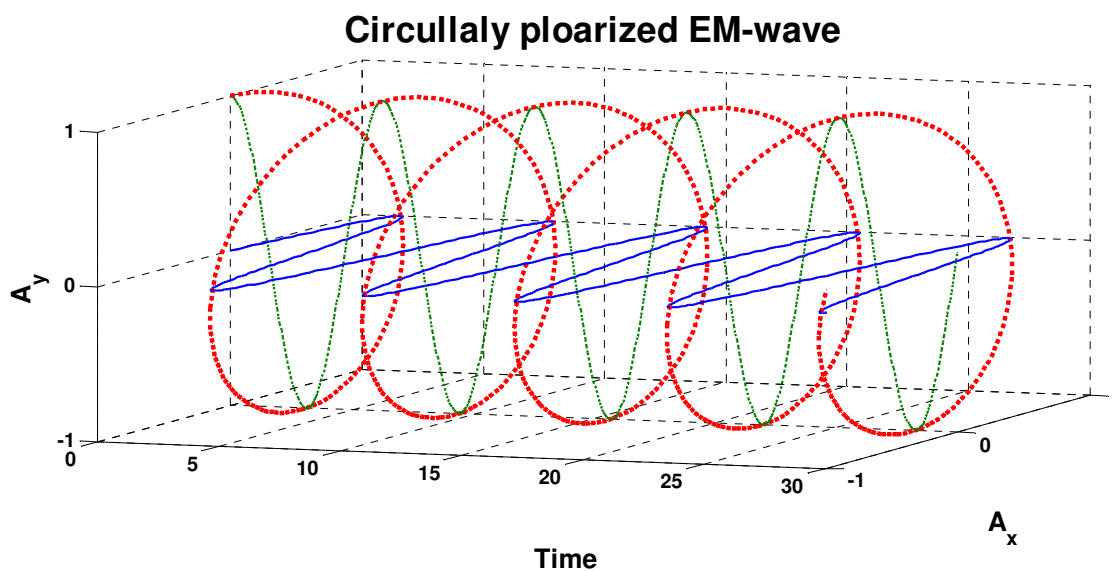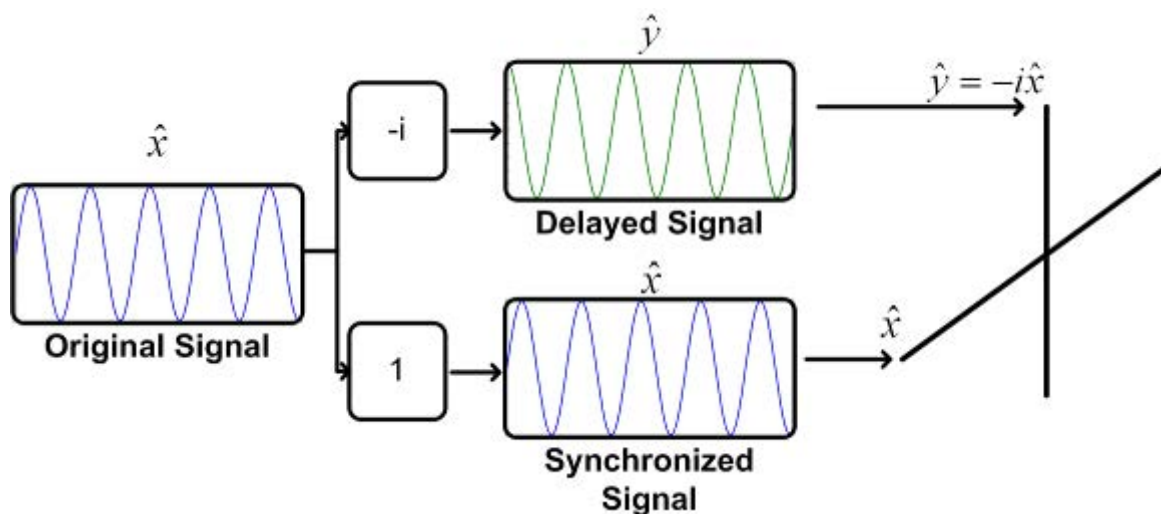
**Figure 4-5: Structure and generation of RHCP EM-waves**

Therefore, in contrast with the linear polarized antennas that need to be precisely aligned with the polarization direction, the circularly polarized antennas can receive the signal as long as they are pointed towards the RHCP signal source. This method of signal broadcasting immunes GNSS signals from attenuation effects introduced by the receiver–satellite polarization mismatch (Tetewsky & Mullen 1996).

An effect called *carrier phase wind-up* or *carrier phase wrap-up* occurs if the source and/or the receiver rotate with respect to each other. This results in an apparent shift in the received phase. In other words, the rotation of an RHCP receiver antenna can cause expansion or contraction of the GPS carrier wavelength. This phenomenon can be elaborated in the following fashion. Consider a stationary RHCP antenna that is aligned towards the propagation direction of a stationary RHCP source. The antenna can receive the rotating electric field at the same frequency as the carrier wave. However, when the antenna is rotated counterclockwise, the antenna senses EM-wave rotations less frequently than when it is stationary. This results in a change in apparent carrier frequency. Kraus (1988) refers to this frequency change as *rotational Doppler*. To explain phase wrap-up mathematically, first the key assumptions are discussed. Both the transmitter and the receiver RHCP antennas can be modeled as cross dipoles that broadcast and receive GPS signals (Tetewsky & Mullen 1996, Wu et al 1993). The dispersion effect due to the ionosphere is neglected as it does not impact the final result significantly and only adds needless complexity. In this research, the radius of rotation of the synthetic array is always less than a metre. Therefore, the elevation angle of the satellite for the centre of the array and the antenna is identical. Also, it is assumed that the horizontal plane of the synthetic array is perfectly aligned with the horizontal plane of the local level coordinate system. Therefore the rotation axis of the synthetic array is parallel to the local vertical direction. Another key assumption addresses the elevation and azimuth of the satellite as viewed from the array. Since each sample of data requires a very short time to be collected (between 5 to 20 s as will be discussed in Chapter 5), the

changes in the satellite elevation and azimuth angle are neglected and they are assumed to be fixed in the sky.

Another issue to be considered is the transmitter rotation. For the case of GNSS navigation, this rotation refers to changes in the attitude of the satellite. The first of these is a gradual, continuous change in the attitude of the satellite due to the rotation of its solar panels (Bisnath et al 2007). The second type of changes in satellite attitude emerges from faster temporal yaw manoeuvres that happen temporally when the earth blocks the sun from a satellite (Bisnath et al 2007). Satellite rotation is common between all receivers and for very precise applications these rotations can be cancelled via differencing. For the case of this research, the opted architecture addresses this common induced error and zeros it. However, to develop a mathematical foundation to analyze phase wrap-up, these rotations are neglected.

### 4.2.2 Phase wrap-up in a base mounted rotating antenna

As described in the previous section, changing the relative heading of an RHCP antenna changes the received carrier phase of the signal and continuous axial rotations change the frequency of the signal or carrier phase rate. The effect of axial misalignment or axial rotations of the receiver antenna on the received signal phase measurements has been addressed in Wu et al (1993), Tetewsky & Mullen (1996), Kim et al (2005) and Beyerle (2009). The corresponding geometry of the axial rotations of the receiver antenna is shown in Figure 4-6.

The EM-wave broadcasted by any crossed dipole antenna can be modeled as (Kim et al 2005)

$$\hat{e}_T = \cos(\alpha)\hat{x}' + \sin(\alpha)e^{j\beta}\hat{y}' . \tag{4-2}$$

In Equation (4-2), $\hat{x}'$, $\hat{y}'$ describe the unit vector along the transmitter crossed dipole, $\alpha, \beta$ describe polarization states and $\hat{e}_T$ is the normalized polarization-phase vector of the wave.
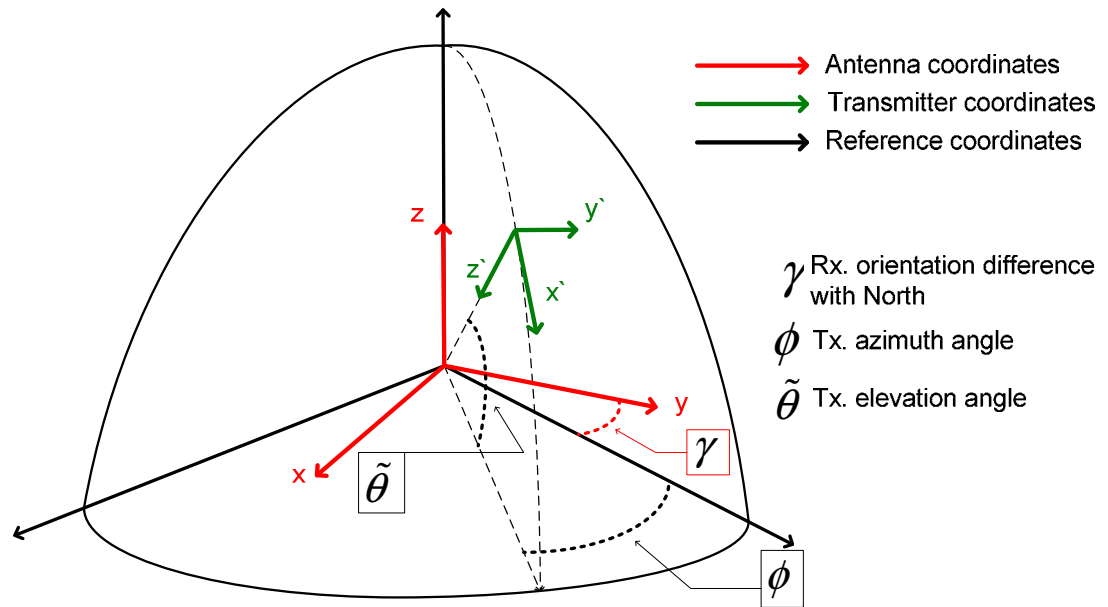


**Figure 4-6: The transmitter and the receiver geometry and rotations**

Tetewsky & Mullen (1996) have characterized the effect of the carrier phase wrap-up (from a wave described in Equation (4-2)) due to a pure fixed axial misalignment or change in the heading of the receiver antenna on the received signal. The antenna output can be found from the scalar product of the incident RHCP field with the antenna model as

$$A(\tilde{\theta},\phi_1,t)\Big|_{Rx} = e^{j(\omega_c t - \kappa r)}\Big[\big(1+\sin\tilde{\theta}\big)\big(\cos\phi_1 - j\sin\phi_1\big)\Big] = \big(1+\sin\tilde{\theta}\big)e^{j\big[\omega_c t - (\phi-\gamma) - \kappa r\big]}.$$ **(4-3)**

where $A(\tilde{\theta},\phi,t,\gamma)\Big|_{Rx}$ is the instantaneous received electrical field in the receiver antenna from a source with elevation and azimuth angle of $\tilde{\theta},\phi$ respectively. In Equation (4-3), $\gamma$ is the heading angle of antenna at time $t$ as shown in Figure 4-3 and Figure 4-6, $\omega_c$ is the carrier angular frequency, and $\phi_1 = \phi - \gamma$ while $\exp(-k_0 r)$ denotes the phase shift associated with the distance between the antenna and the transmitter and $k_0 = 2\pi/\lambda$. Equation (4-3) shows that the carrier phase wrap-up depends on $\phi_1 = \phi - \gamma$ which is the difference of the antenna heading angle and the azimuth of the GNSS satellite. The antenna rotation or any change in the antenna orientation that alters $\gamma$ causes the received phase to be changed. Equation (4-3) describes the case when only a static change has occurred on $\gamma$; when the antenna is rotated continuously, Equation (4-3) can be modified as

$$A(\tilde{\theta},\phi,\gamma,t)\Big|_{Rx} = \big(1+\sin\tilde{\theta}\big)e^{j\big[\omega_c t - \phi - \dot{\gamma}(t)t - k_0 r\big]} = \big(1+\sin\tilde{\theta}\big)e^{j\big[(\omega_c - \dot{\gamma})t - \phi - k_0 r\big]}$$ **(4-4)**

where $A(\tilde{\theta},\phi,t,\gamma)\Big|_{Rx}$ is the instantaneous received electrical field in the receiver antenna. At the part of the Equation (4-4), a general form for antenna rotation is presented and the second term is evaluated assuming a constant angular velocity of $\dot{\gamma}$ for the antenna heading. In Equation (4-4), phase wrap-up is expressed via $-(\dot{\gamma}t + \phi)$ and this equation clarifies that when a static antenna is rotated at a constant rate, the carrier frequency

appears to be shifted down (or up, depending on the rotation direction) by exactly the antenna rotation rate.

In Equation (4-4), carrier phase wrap-up can be separated from the Doppler shift since the latter depends only on the satellite-receiver range rate vector $r$. It also reveals that the phase wrap-up does not depend on the carrier frequency and is proportional to the rotation rate of the antenna. This equation also states that the azimuth of the satellite only affects the initial bias of the phase wrap-up from zero and does not change the received carrier frequency. Figure 4-7 shows the carrier phase wrap-up of an antenna that rotates with the rate of 0.63 rad/s and -0.63 rad/s, when the satellite is located at an elevation of $45°$ and an aimuth of $45°$ as well.
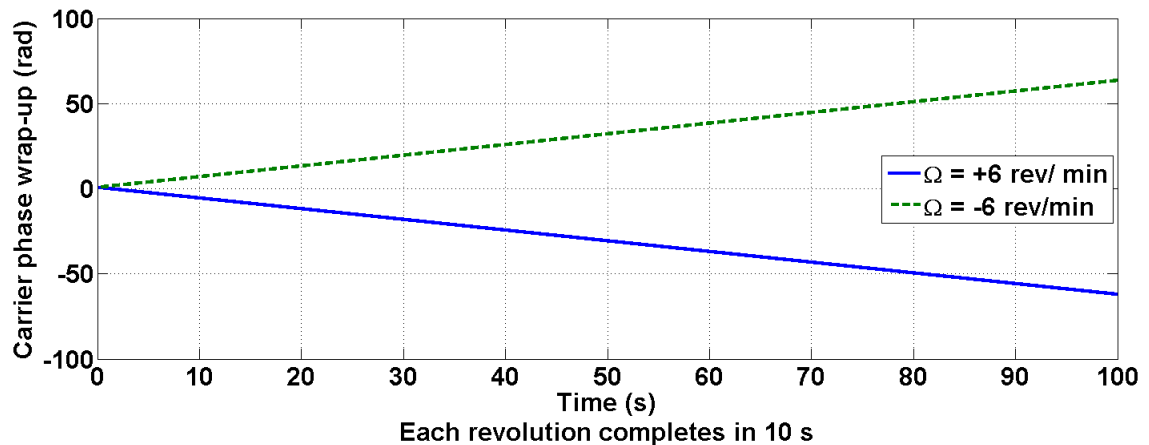


**Figure 4-7: Phase wrap-up caused by antenna rotation**

It must be noted that Figure 4-7 only shows the phase change due to a static antenna that is being rotated about the vertical axis

### 4.2.3 Phase wrap-up in an antenna mounted on a rotating lever arm

In the case of a synthetic array when the rotation axis is offset with respect to the antenna axis, a different approach is required as it is a more complex situation. As can be

seen in Figure 4-7, the received phase changes constantly with time, which is an indicator of a bias in the received frequency. This additional Doppler shift due to the phase wrap-up affects the performance of the array and perturbs the array manifold vector of the synthetic array. The antenna array performance degradation due to the antenna location perturbation is discussed extensively by Van Trees (2002). In other words, this additional Doppler can be visualised as a falsely implied linear motion added up to the antenna dynamics. This is shown in Figure 4-8.



Figure 4-8: Induced array perturbation due to phase wrap-up
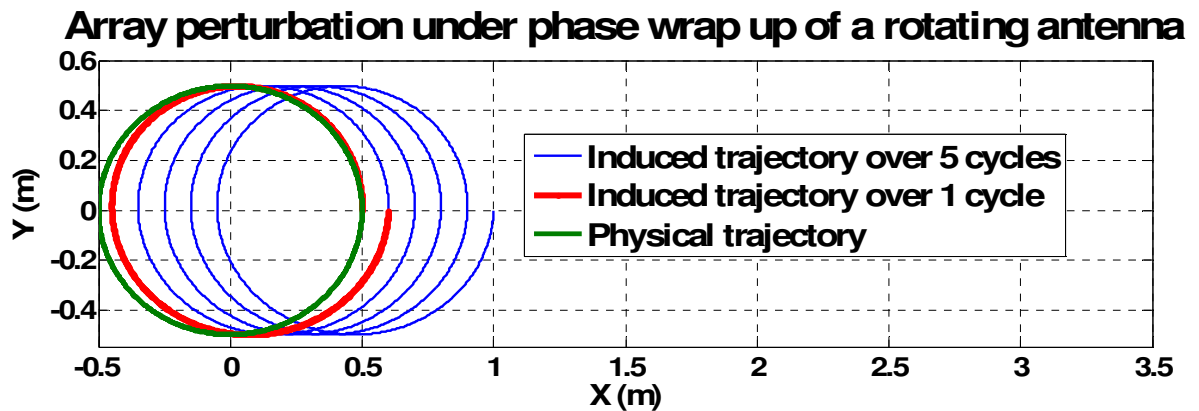
In Figure 4-8, the antenna is fixed on a rotating lever arm and therefore moves on the green trajectory. In this case due to the changes in the antenna heading angle an additional Doppler shift as discussed previously appears. This additional Doppler shift can be modeled by an extra fake linear motion in addition to the original circular motion of the antenna as shown in Figure 4-8. This phenomenon should be modeled and considered in the synthetic circular array processing. The detailed mathematical formulation used to derive the Doppler due to the antenna motion on a circular trajectory is derived in Appendix A where it is proven that the Doppler frequency due to fixing an antenna on a rotating lever arm is

$$f_d = \left[ \dot{\gamma}(t) + \frac{2\pi}{\lambda} R\dot{\gamma}(t)\cos\tilde{\theta}\sin\left(\phi - \dot{\gamma}(t).t\right) \right],$$

(4-5)

where the first term is the phase wrap-up and is introduced from the rotation of the antenna and the second term is the Doppler shift emerging from moving the antenna on a circular trajectory. It must be noted that if the rotation rate is constant or the motion is predictable, the term $\dot{\gamma}(t)$ can be used to wipe off the phase wrap-up. However, in the high dynamic cases or for vehicular applications, $\dot{\gamma}(t)$ can be extracted from a gyroscope to compensate for the antenna rotations.

From Equation (4-5), it can be concluded that the phase wrap-up does not depend on the azimuth or elevation of the satellite, but solely depends on the rotation rate of the lever arm. However, the circular motion introduced by the lever arm results in a Doppler effect that leads to the phase shifts described in Chapter 3 via the array manifold vector. This equation also shows that when the satellite is at zenith, the $\cos\tilde{\theta}$ equals zero and the results of this case are identical to the case when the antenna is rotated about its own axis. Figure 4-9 shows the effect of different parameters on phase wrap-up accumulation.

The upper part of Figure 4-9 shows the effect of the satellite's elevation angle on the received phase. It is evident that when the satellite is at lower elevation angles the translational motion of the receiver increases the amplitude of the periodical component more significantly. Also, as can be seen in the lower part of Figure 4-9, the rotation rate not only affects the slope of the ramp but also changes the amplitude motion Doppler component.
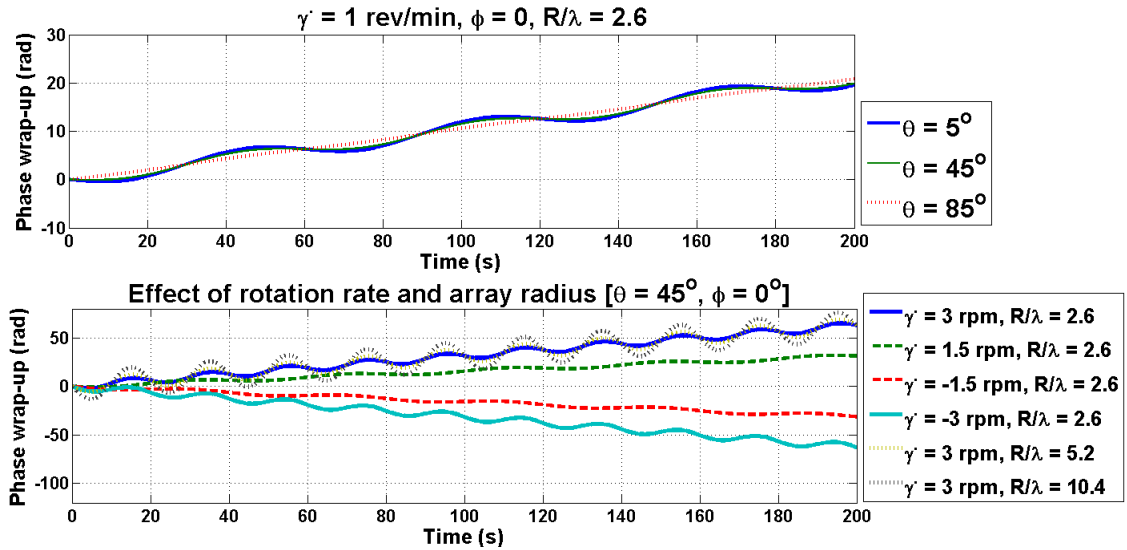
**Figure 4-9: Effect of several parameters on the phase wrap-up accumulation**

It must be noted that in Figure 4-9, the ramp term is introduced via the rotation of the antenna and is imposed by the phase wrap-up, while the sinusoidal component emerges from the circular motion of the antenna.

### *4.2.4 Effect of phase wrap-up on AoA estimation accuracy and beamforming*

As mentioned before, the antenna axial rotation introduces a shift in the received signal frequency. In the previous section the antenna phase wrap-up phenomenon was modeled and analyzed. In this section, the signal received by the synthetic array is simulated while considering the antenna rotation. Table 4-1 summarizes the technical aspects of the simulation for each elevation of arrival considered. In this simulation scheme each sample contains a vector of complex values with a length of 50. Samples are generated in such a way as to mimic the characteristics of a signal captured by a uniform circular array with a radius of 0.5 m that gives $R/\lambda = 2.6$ for the GPS L1 signal. The synthetic array is assumed to be rotating in six cases of 3, 6 and 12 rpm counter

clockwise (CCW) and 3, 6 and 12 rpm clockwise (CW). This is performed to get an understanding on how the direction and rate of rotation can affect the synthetic array performance. The studied parameters include AoA estimation accuracy and the array gain performance in dB. Also, the signals coming from seven different elevations of arrival have been considered to cover the effect of the transmitter-receiver geometry. The signal to noise ratio of this is also set to +20 dB to ensure that the only corruption arises from the phase wrap-up.

**Table 4-1: Phase wrap-up simulation technical specifications for each elevation angle**

| Case # | Parameter | Value |
|---|---|---|
| 1a – 1b | Sample duration (s) | 5 |
|  | Rotation rate (rpm) | ±12 |
|  | # of snapshots per sample | 250 |
| 2a – 2b | Sample duration (s) | 10 |
|  | Rotation rate (rpm) | ±6 |
|  | # of snapshots per sample | 500 |
| 3a – 3b | Sample duration (s) | 20 |
|  | Rotation rate (rpm) | ±3 |
|  | # of snapshots per sample | 1000 |
| Common parameters | | |
| Parameter | | Value |
| Array radius (m) | | 0.5 |
| Wavelength (m) | | 0.19 |
| $R/\lambda$ | | 2.6 |
| Simulation length (s) | | 1000 |

The first part of Figure 4-10 shows the output of more than 10,000 Monte Carlo simulations for different cases. The time length of simulation is set to 1,000 s hence resulting in 50, 100 and 200 samples for each rotation speed respectively. The coherent integration time is set to 20 ms which gives 1000, 500 and 250 snapshots per synthetic array sample. Therefore, if the beamforming is performed accurately, it will result in an

array gain equal to the number of snapshots per samples. In other words, for each case the expected array gain is 250, 500 and 1000 or in decibel units: 24 dB, 27 dB and 30 dB. Since each case results in a different AG, and one of the goals is to compare the loss of AG for each rotation speed, the ratio of achieved array gain to the expected array gain is shown in the first part of Figure 4-10 . In other words, the values shown in the first part of Figure 4-10 are the amplified signal levels after beamforming that are normalized by the number of elements in the array.
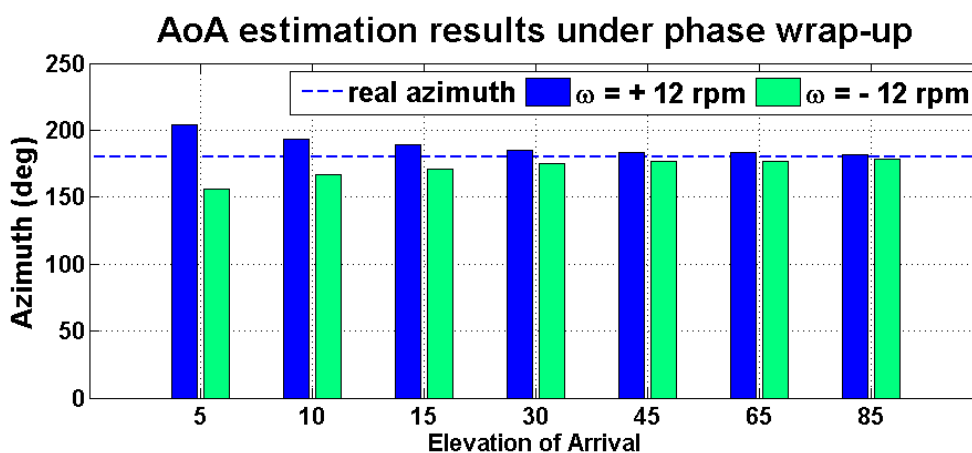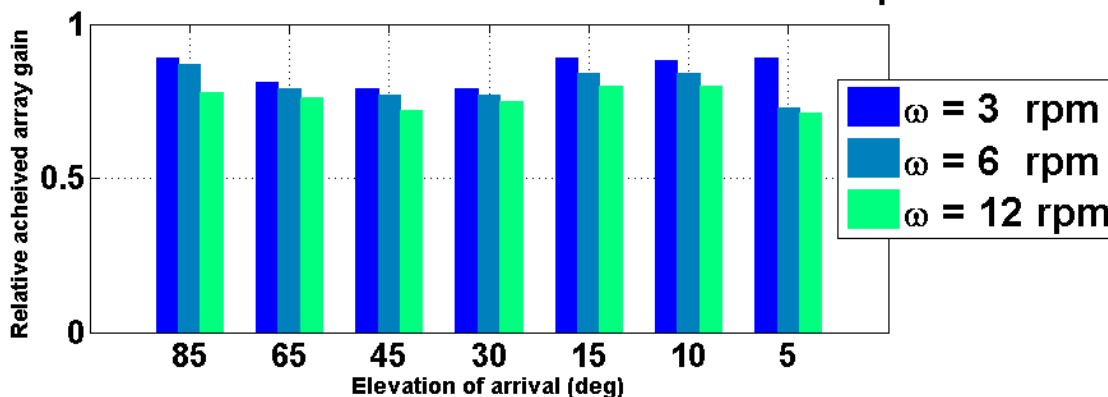


**Figure 4-10: Effect of phase wrap-up on array performance**

According to the first part of Figure 4-10, it is evident that under phase wrap-up perturbation, higher rotation speeds result in higher gain degradation and also, the

signal's elevation of arrival and the direction of rotation does not have any significant effect on this gain reduction.

In addition, the effect of this phenomenon on AoA estimation along the azimuth is interesting. As can be seen in the second part of Figure 4-10, phase wrap-up causes systematic errors of more than 20 degrees in the AoA estimation along the azimuth. The direction of array rotation also affects the sign of this error and it seems that clockwise and counter clockwise rotation rates of equal values lead to positive and negative azimuth estimation errors of equal values, respectively.

For low resolution arrays (arrays with small $R/\lambda$ and consequently wide beam-widths) and low accuracy applications, it seems that the AoA estimation error along elevation can be neglected.

Finally, Kim et al (2005) have presented methods to eliminate this effect via single and double differencing approaches for static cases. The mathematical equations presented herein can also help to remove the destructive errors corresponding to this effect and to restore corrupted data with phase wrap-up via post-compensation of induced frequency shift. However, throughout this research the synthetic array mechanization has been modified in an attempt to avoid phase wrap-up in the first place for most of the collected data sets. In Chapter 5, a brief discussion of the practical aspects of the phase wrap-up as well as the utilized mechanism to avoid this issue is presented.

## 4.3 Effect of the antenna pattern on the AoA estimation profile

The effect of the antenna pattern on the array gain pattern was discussed briefly in Section 3.5. This section describes the effect on the AoA estimation profile in more depth

as a major parameter in channel characterization. As stated in Section 3.5 and Equation (3-30) and Equation (3-31), the antenna gain pattern itself has a major impact on the gain pattern of the array. This is done through the changes in the peak to side-lobe ratio of the array gain pattern. For instance, if the peak to side-lobe ratio of a particular array is 6 dB along elevation, an antenna element with a gain roll-off of 13 dB affects the gain pattern of the array differently when steering towards lower or higher elevation angles. Throughout the experimental parts of this research, two antenna elements have been used with two different patterns. Therefore, in the simulation-based analysis that is presented in this section, these antennae are considered and compared to each other and also against the hypothetical case of an isotropic antenna. The examined antenna patterns are a NovAtel GPS 701/702 GGL series, a Ublox M-335 and a hypothetical isotropic antenna. Table 4-2 summarizes some of the most relevant technical aspects of the first two antennas and Figure 4-11 shows the respective antenna patterns.

**Table 4-2: Antenna element characteristics**

| Antenna manufacturer and model | Gain at zenith | Gain Roll-off |
|---|---|---|
| NovAtel GPS 701/702 GG | +5 dBic | 13 dB |
| Ublox M-335 | +4 dBic | 2.5 dB |
| Hypothetical isotropic antenna | 0 | 0 |

Two multipath environments are studied here via simulations. The first case addresses the situation where a LoS signal that is coming from a moderate elevation angle is corrupted with multipath interference coming from low to high elevation angles. The second scenario corresponds to the case where a high elevation LoS signal is corrupted by several lower elevation multipath signals. The main motivation behind these

scenarios is to gain an understanding of how antenna gain pattern affects the AoA estimation performance.
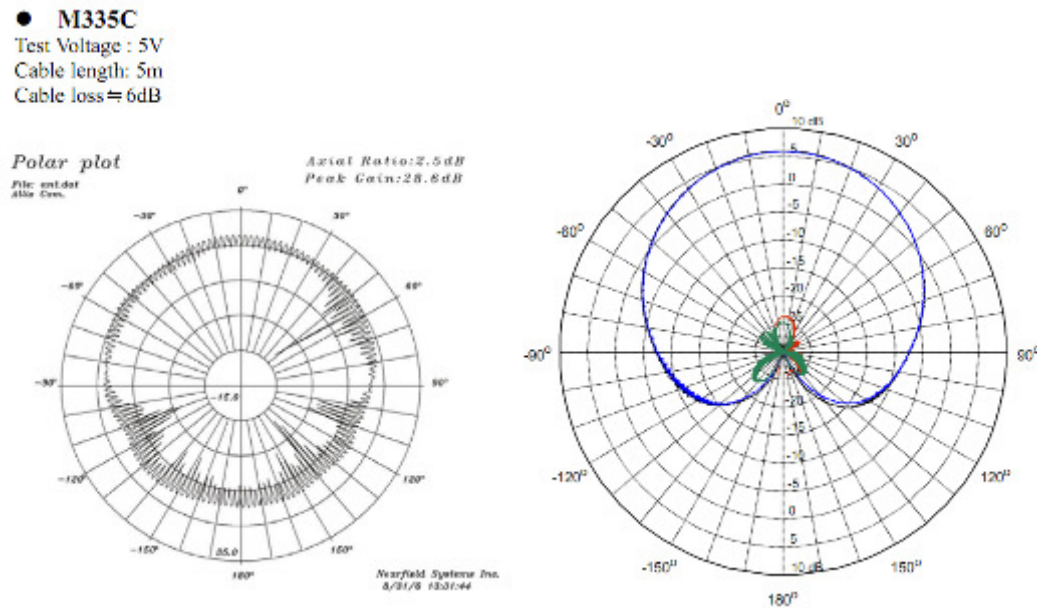


**Figure 4-11: Antenna gain pattern of a) Ublox and b) NovAtel**

Two multipath environments are studied here via simulations. The first case addresses the situation where a LoS signal that is coming from a moderate elevation angle is corrupted with multipath interference coming from low to high elevation angles. The second scenario corresponds to the case where a high elevation LoS signal is corrupted by several lower elevation multipath signals. The main motivation behind these scenarios is to gain an understanding of how antenna gain pattern affects the AoA estimation performance.

4.3.1.1 Mid-elevation LoS with multipath

To assess the effect of the antenna element pattern on the AoA estimation performance a simulation approach was chosen. The simulated samples are mainly made up from a LoS signal coming from an elevation of $45^{o}$ and an azimuth of $180^{o}$. Five other multipath components coming from elevation angles of $5^{o}$, $25^{o}$, $45^{o}$, $65^{o}$ and $85^{o}$ and with a uniform distribution in azimuth are also added. In this simulation scenario, multipath components are considered to be 3 dB weaker than the LoS signal. Afterwards the LoS and multipath components undergo the antenna patterns that were discussed in the previous sections. Consequently, the signals are processed via the beamscan method and the resulting pattern is fed into a function that detects multiple peaks with respect to a certain threshold. As indicated at the beginning of this section and in Section3.5, the typical gain difference between the peak and sidelobes of arrays used in this research is in the neighbourhood of 6 dB (not considering the effect of antenna pattern on the array gain pattern). Hence herein, any threshold of 5 dB or less eliminates the signals detected by sidelobes as described in Section 4.1. An example of beamscan output and the detected peaks (with a 3 dB threshold) for each antenna element is shown in Figure 4-12.

Figure 4-12 (d) shows the AoA of the simulated LoS signal along with the AoA of multipath signals and their relative signal levels. The output of 1000 Monte-Carlo simulations for this scenario along the elevation angle is shown in Figure 4-12 a-c for different antennas. In these figures, blue circles show the detected peaks of each sample (an example of these peaks is shown in Figure 4-12 a-c with a 3 dB threshold).
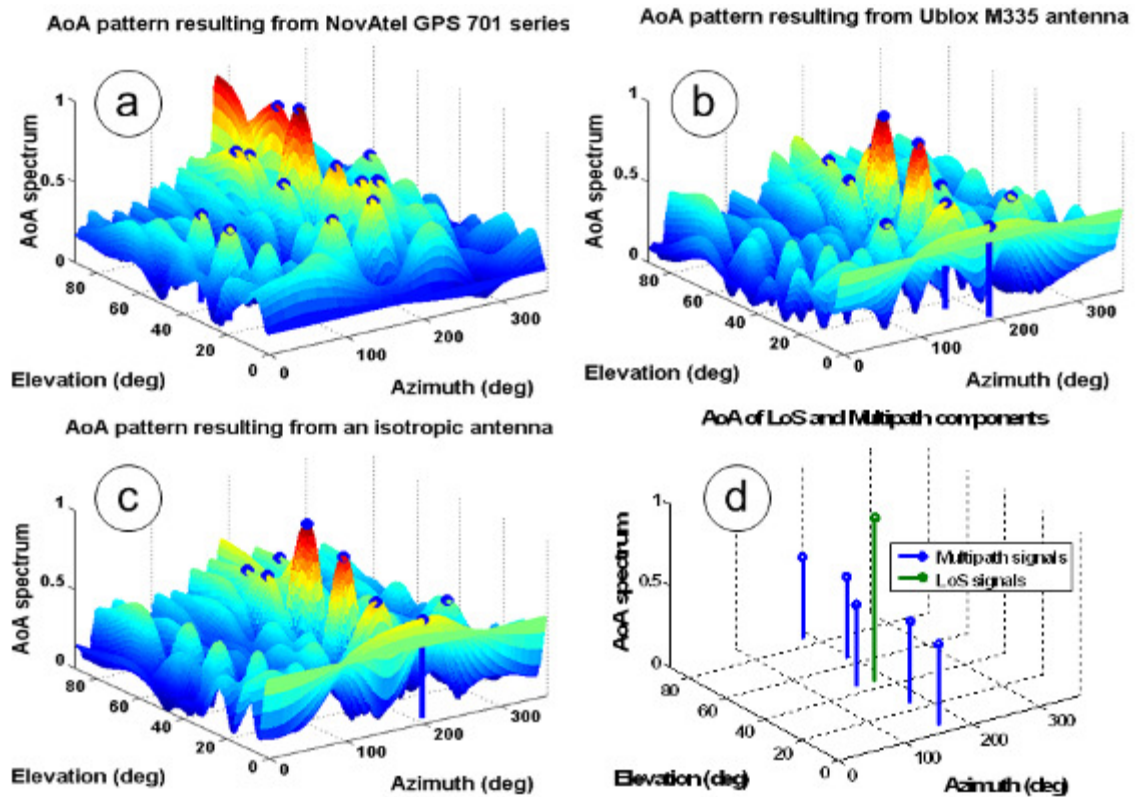
**Figure 4-12: a-c) Samples of beamscan outputs for different antennas and detected peaks, d) True AoA of LoS and multipath signals**

The solid black line represents the probability density function resulting from the detected peaks. The dashed green and red lines show the elevation angle and the relative power of the LoS and the multipath signals respectively after being received by each antenna. The signal levels are normalized in such a way as to equal their sum of power to one.

The detected AoA distributions with the same conditions are shown with solid black lines in Figure 4-13.
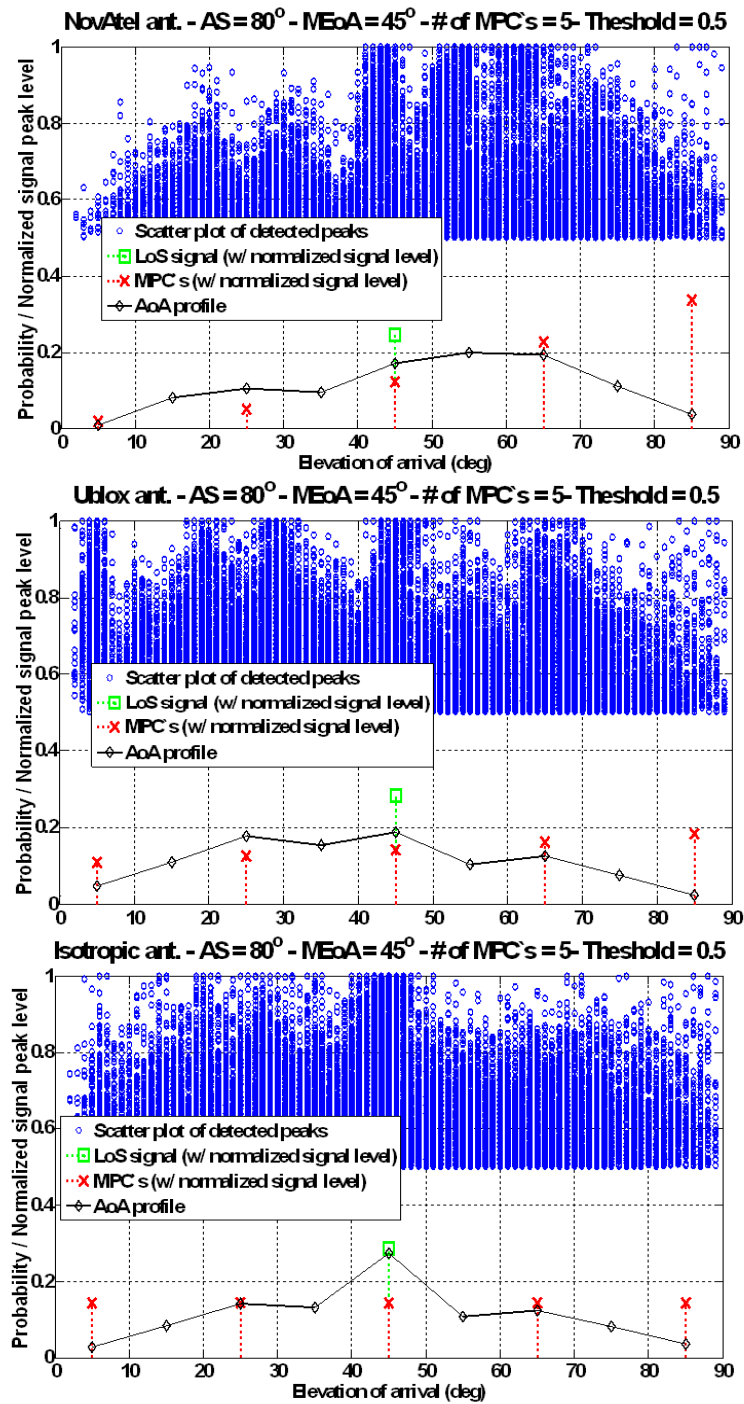
**Figure 4-13: Elevation of LoS and multipath signals with relative power levels and output of beamscan and estimated AoA profile with different antennas. a) NovAtel, b) Ublox, c) Isotropic**

It is evident that for the case of mid to low LoS signals with uniform distribution of multipath components, the most accurate result is achieved through the use of an isotropic antenna element while the Ublox and NovAtel antenna both have equal performance.

4.3.1.2 High-elevation LoS with multipath

The previous simulation focused on the low elevation LoS signals. Another possible scenario can include a major LoS component from a high elevation source and many other multipath signals coming from the lower elevation angles. To assess the effect of the antenna gain pattern on the AoA estimation performance under such scenarios, a new set of simulations was run. The simulated samples are mainly made up from an LoS signal coming from an elevation of $80^o$ and azimuth of $180^o$. Five other multipath components are also added to this signal that come from elevation angles of $35^o$, $45^o$, $55^o$, $65^o$ and $75^o$ and uniformly random azimuth angles from $140^o$ to $220^o$. The rest of the simulation scenario is similar to the previous case. The peak detection threshold is considered to be 3 dB, and signals undergo through the antenna gain pattern before being processed. A sample of AoA pattern is shown in Figure 4-14, along with the real AoA of LoS and multipath signals. Figure 4-14 (d) shows the simulated LoS signal and its relative AoA and level with respect to the multipath components. The output of 1,000 Monte-Carlo simulations using this scenario along with elevation angle is shown in Figure 4-15 a-c for different antennas, using a 3 dB threshold.

AoA pattern resulting from NovAtel GPS 701 series

AoA pattern resulting from Ublox M335 antenna

AoA pattern resulting from an isotropic antenna

AoA of LoS and Multipath components
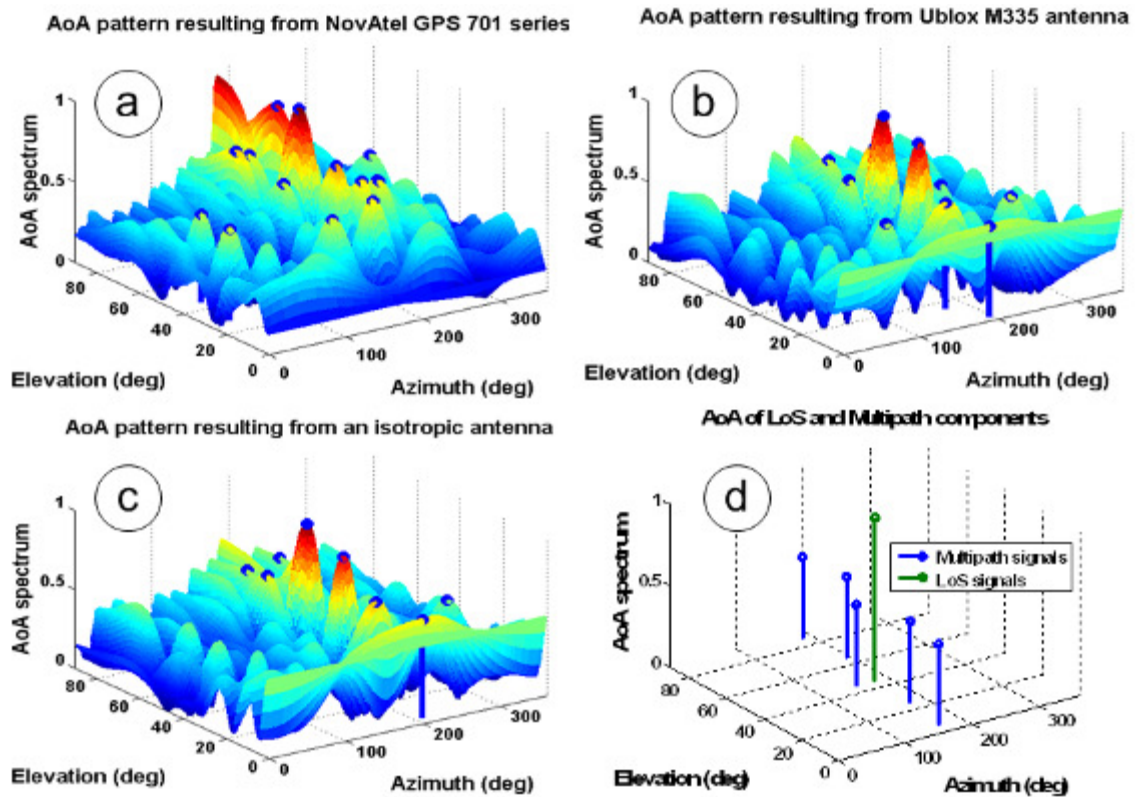
**Figure 4-14: a-c) Samples of beamscan output for different antennas and detected peaks, d) True AoA of LoS and multipath signals**

Also Figure 4-15 d-f shows the AoA profile and detected peaks resulting from another 1,000 Monte-Carlo simulations with a 1.5 dB threshold. According to Figure 4-15 (d), the NovAtel antenna outperforms the other two in low elevation multipath rejection. Also according to Figure 4-15 (d) to (f), it seems that depending on the scenario, increasing the peak detection threshold results in a more accurate AoA characterization. It was also seen that both the NovAtel and Ublox antennas have almost equal performance. However, the latter case showed that for an high elevation LoS, the NovAtel antenna gives far more accurate results.
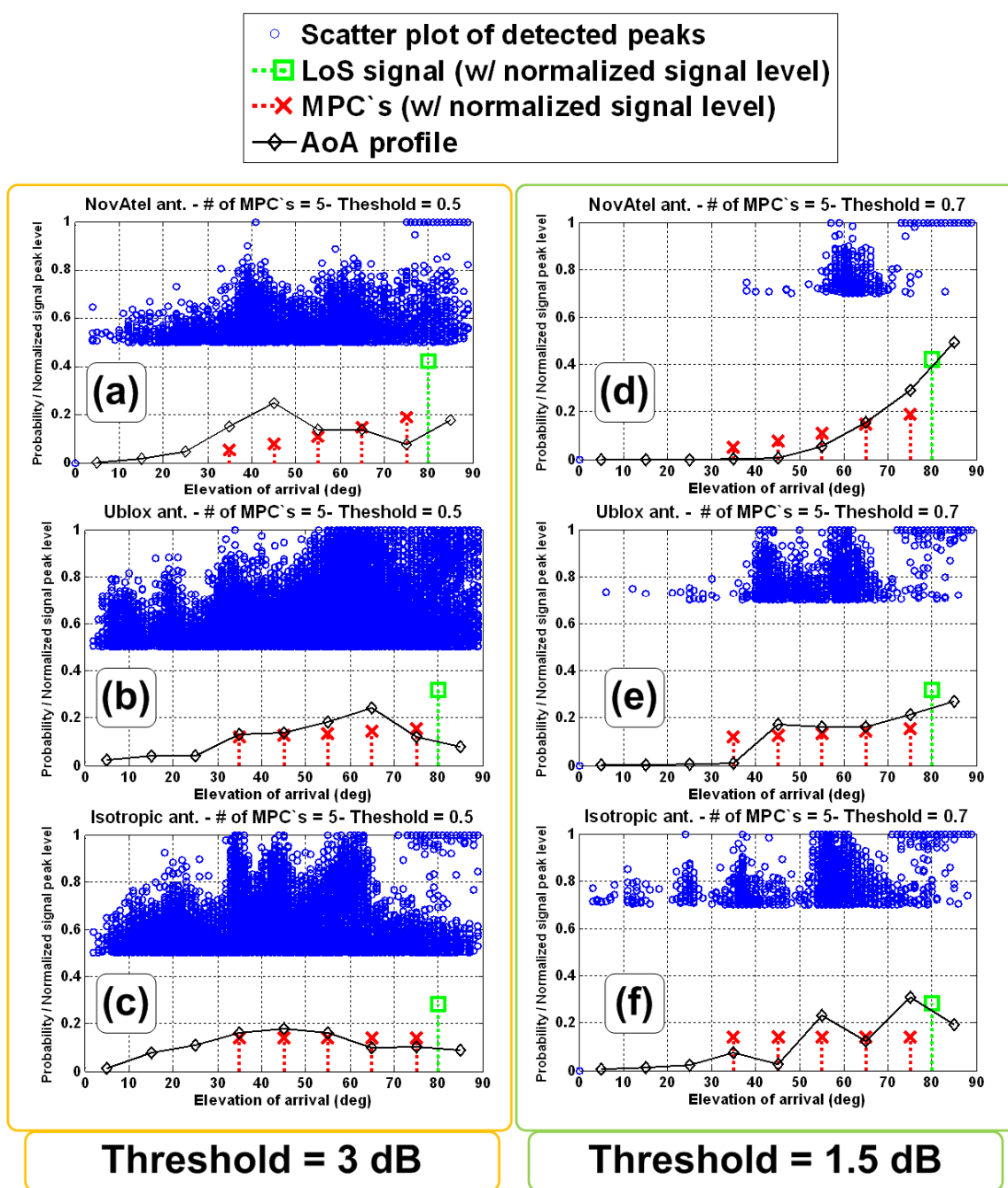
**Figure 4-15: Elevation of LoS and Multipath signals with relative power levels and output of beamscan and estimated AoA profile for different antennas and thresholds. a) NovAtel- 3 dB, b) Ublox- 3dB, c) Isotropic- 3 dB d) NovAtel- 1.5 dB, e) Ublox- 1.5dB, f) Isotropic- 1.5 dB**

**4.4 Array gain limitations due to multipath**

To increase the SNR of the received signal, many conventional receiver architectures rely on increasing the coherent integration time as described in Section 2.3. Broumandan et al (2011b) have shown that the processing gain of a mobile receiver that is obtained via coherent integration has a saturation limit under multipath conditions. This means that, unlike LoS conditions where increasing the coherent integration time increases the processing gain of the receiver, under multipath condition, an upper limit for the coherent integration gain exists. This boundary, which is associated with the processing gain, depends on the scatterer angular spread and the dynamics of the mobile receiver. This section characterizes the array gain limitation in multipath environments.

*4.4.1 Array gain under multipath conditions*

The transmitted signal received by an array is corrupted with the channel noise that can be modeled by its equivalent baseband model $w(t)$, which is assumed to be white with the power spectral density of $N_0$. The signal $r(t)$, which is collected by the receiver through the synthetic antenna array, can be expressed as

$$r(t) = A(\mathbf{p}(t))s_0(t) + w(t) \tag{4-6}$$

where $A(\mathbf{p}(t))$ is the channel gain as described in Section 2.5 and 2.6, $s_0(t)$ is the signal component as described in Section 2.3 and $w(t)$ is the noise component. Before entering the beamforming process, $r(t)$ has undergone the following processes: the signal is captured by the receiver, correlated with the locally generated replica and then coherently

integrated for $T_{coh}$. Through beamforming, the outputs of each snapshot are added together by using the phase information and the delay introduced due to the spatial distance of each element from the centre of the array. If the array is made up of a total number of $M$ individual antennas, the beamforming output from only the consecutive $m$ elements of the array is equal to

$$
\begin{aligned}
x &= \frac{1}{mT_{coh}} \int_0^{mT_{coh}} r(t)s_0(t)^* dt \\
&= \frac{1}{mT_{coh}} \int_0^{mT_{coh}} [A(\mathbf{p}(t))s_0(t) + w(t)]s_0(t)^* dt \\
&= \frac{1}{mT_{coh}} \left( \int_0^{mT_{coh}} A(\mathbf{p}(t))s_0(t)s_0(t)^* dt + \int_0^{mT_{coh}} w(t)s_0(t)^* dt \right)
\end{aligned}
$$

(4-7)

It must be noted that the components of the array manifold vector are considered in the local replica of the signal ($s_0(t) = s_i(t)v_i$). One may choose to impose the components of the array manifold vector out of the integration process. The channel noise term in Equation (4-7) is a zero mean circularly Gaussian random variable with variance $\sigma_w^2$ which can be calculated by

$$
\begin{aligned}
\sigma_w^2 &= \left( \frac{1}{mT_{coh}} \right)^2 \times \int_0^{mT_{coh}} \int_0^{mT_{coh}} E\{w(t)w^*(t')\}s_0(t)s_0(t')^* dtdt' \\
&= N_0 \left( \frac{1}{mT_{coh}} \right)^2 \times \int_0^{mT_{coh}} \int_0^{mT_{coh}} mT_{coh}s_0(t)s_0(t')^* dtdt' \\
&\approx \frac{N_0}{mT_{coh}}
\end{aligned}
$$

(4-8)

To derive Equation ((4-8) the narrowband property of GNSS signals was exploited $\left( B \gg \left(1/MT_{coh}\right) \right)$ and also the assumption that the GNSS signals possess the nominal power of unity as

$$\int_0^{mT_{coh}} \int_0^{mT_{coh}} s_0(t)s_0(t')^* dtdt' \approx mT_{coh} .$$ (4-9)

Finally, to derive the array gain, the variance of the signal component of $x$ (which is also a zero mean CN random signal) in Equation ((4-9) must be derived. $\sigma_s^2$ can be expressed as

$$\sigma_s^2 = \left(\frac{1}{mT_{coh}}\right)^2 \int_0^{mT_{coh}} \int_0^{mT_{coh}} E\{A(\mathbf{p}(t))A^*(\mathbf{p}(t'))\}dtdt'$$ (4-10)

where it is assumed that $|s_0(t)|^2 \approx 1$. Since the term $E\{A(\mathbf{p}(t))A^*(\mathbf{p}(t'))\}$ is related to the normalized spatial correlation $(C_n)$ of the channel as

$$C_n(\mathbf{p}(m_1 T_{coh}) - \mathbf{p}(m_2 T_{coh})) = \frac{1}{\sigma_A^2} E\{A(\mathbf{p}(t))A^*(\mathbf{p}(t'))\}$$ (4-11)

therefore, for the case of a synthetic uniform circular array rotating at the constant angular velocity of the $\omega$, Equation ((4-11) can be rewritten as

$$\sigma_s^2 = \frac{\sigma_A^2}{(mT_{coh})^2} \int_0^{mT_{coh}} \int_0^{mT_{coh}} C_n(\omega(t-t'))dtdt' .$$ (4-12)

This Equation can be simplified by introducing the new dimensionless variable $q = (t-t')/mT_{coh}$, which yields

$$\sigma_s^2 = 2\sigma_A^2 \int_0^1 (1-q) C_n(q\omega mT_{coh})dq .$$ (4-13)

In Equation ((4-13) the term $\omega mT_{coh}$ expresses the distance between two arrat elements. For instance, setting $m$ to unity will represent the spatial (angular) distance between two consecutive elements that are taken at two certain snapshots, separated with a constant interval of $T_{coh}$. Therefore, increasing $\omega$ increases the distance between the

two elements and increasing $m$ means considering a longer portion of antenna motion. By

considering $\Omega(\omega m T_{coh}) = 2\int_0^1 (1-q) C_n (q\omega m T_{coh}) dq$, the signal variance can be written as

$$\sigma_s^2 = 2\sigma_A^2 \int_0^1 (1-q) C_n (q\omega m T_{coh}) dq \qquad \text{(4-14)}$$

$$= \sigma_A^2 \Omega(\omega m T_{coh})$$

For the case of a stationary antenna, $\omega = 0$ and therefore, $\Omega(\omega m T_{coh}) = 1$. Now

the only required parameter to evaluate the signal variance is the normalized correlation

coefficient, which is defined as follows (Van Trees 2002) for a uniform distribution along

azimuth with a density function of $S(\phi)$:

$$C_n (\omega m T_{coh}) = \frac{\int_{-\Phi}^{+\Phi} S(\phi) e^{(2\pi j \omega m T_{coh} \sin\phi)} d\phi}{\int_{-\Phi}^{+\Phi} S(\phi') d\phi'} \qquad \text{(4-15)}$$

where $\Phi$ denotes the limits of angular spread. For the case of the sphere of scatterers, $C_n$

should be re-written as (Broumandan 2009)

$$C_n (\omega m T_{coh}) = \frac{\int_0^{\Theta} \int_{-\Phi}^{+\Phi} S(\phi,\theta) \sin\theta\, e^{(2\pi j \omega m T_{coh} \sin\theta \cos(\phi - \omega m T_{coh}))} d\phi d\theta}{\int_0^{\Theta} \int_{-\Phi}^{+\Phi} S(\phi,\theta) \sin\theta\, d\phi d\theta} \qquad \text{(4-16)}$$

Without loss of generality and to simplify computations in the case of the ring of

scatterers model where $S(\phi)$ can be assumed to be uniformly distributed over $-\Phi$ to

$+\Phi$, $\sigma_s^2$ can be computed. For instance, shows $C_n (\omega m T_{coh})$ for different angular

spreads with uniform distribution and rotation speeds for $m = 1$, $T_{coh} = 200\,ms$.
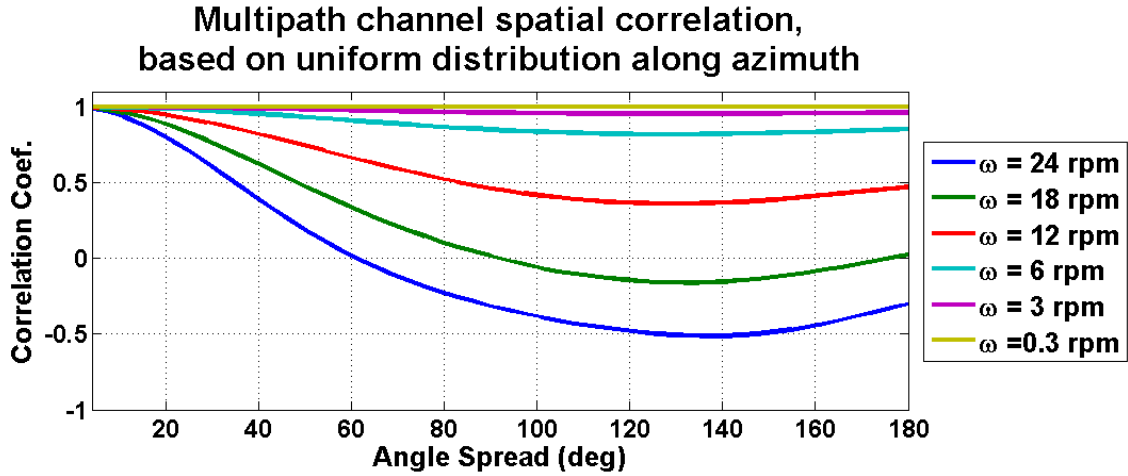
**Figure 4-16: Normalized correlation coefficients.**

To compute the array gain as the performance measure of beamforming, the signal $x$ can be normalized by the standard deviation of the additive channel noise to obtain an output average SNR with respect to the interval of $mT_{coh}$ as (Broumandan et al 2011b):

$$\rho_t = \frac{\sigma_s^2}{\sigma_w^2} = \frac{\sigma_A^2 \Omega(\omega m T_{coh})}{N_0 / mT_{coh}} \tag{4-17}$$

which for the case of a stationary antenna, $\rho_t = T\sigma_A^2 / N_0$ .

### 4.4.2 Array Gain degradation under multipath

Broumandan et al (2011b) propose the concept of Gain Degradation (GD) to assess the performance of the coherent integration. To quantify GD, the achieved processing gain through coherent integration for the mobile antenna is compared against the achieved processing gain through the same coherent integration length of a static antenna. The same concept can be adapted to a synthetic UCA. Therefore, the array gain can be compared against the output SNR of long coherent integrations with the equal

duration of $mT_{coh}$ for a static antenna. It must be noted that $mT_{coh}$ is a sector of the UCA

and this definition of GD can be written as

$$GD = \frac{SNR\big|_{beamforming}^{UCA}}{SNR\big|_{coherent\ integration}^{Static}} = \frac{\rho_t^{UCA}}{\rho_t^{Static}} = \frac{\rho_t^{Static}\Omega(\omega mT_{coh})}{\rho_t^{Static}} = \Omega(\omega mT_{coh}).$$ (4-18)

Hence, by studying $\Omega(\omega mT_{coh})$, one can completely characterize the

beamforming performance in the presence of multipath and angular spread. In the

following section, GD is studied under the uniform distribution of AoA along azimuth

angle assumption. Figure 4-17 shows the effect of AS (with uniform distribution) on GD

for a certain $mT_{coh}$. Figure 4-18 shows the GD for different distances on array elements

($mT_{coh}$) for two different angular spreads. The following approach helps to interpret the

plots shown in Figure 4-18. Consider a synthetic UCA under harsh multipath. Each

element of the UCA is generated from $20\,ms$ of coherent integration of the mobile

receiver data and the multipath is characterized with a ring of scatterer profile with AS of

$22^{o}$ (as shown in the first part of Figure 4-18). It must be noted that, according to

assumptions made in Equations (3-10) and (3-11), during the coherent integration period,

the receiver antenna is assumed to be static. If the rotation speed of the Synthetic UCA is

$1\,rad/\sec \approx 9.5\,rpm$, the expected array gain from beamforming with 10 elements

$mT_{coh} = 200\,ms$ is 10 (or $AG = 10 \times \log_{10}(10) = 10\,dB$).
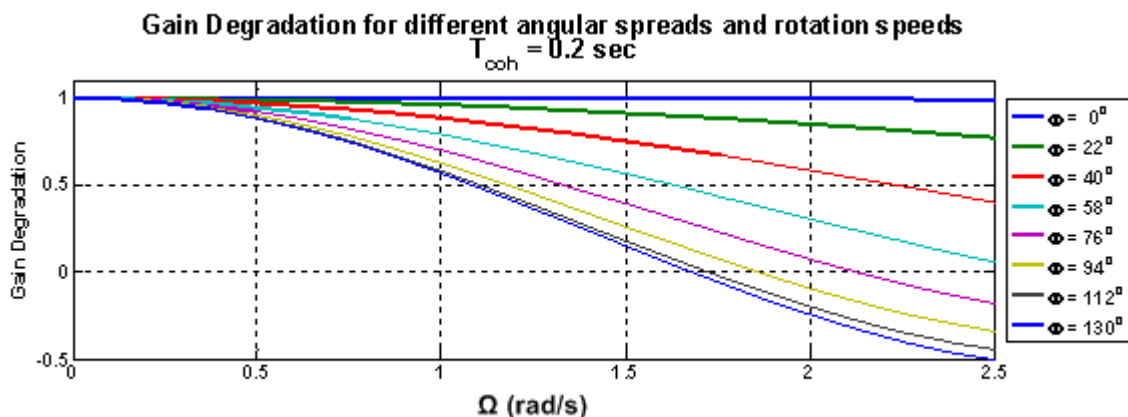
**Figure 4-17: Gain degradation under different AS and rotation speeds.**
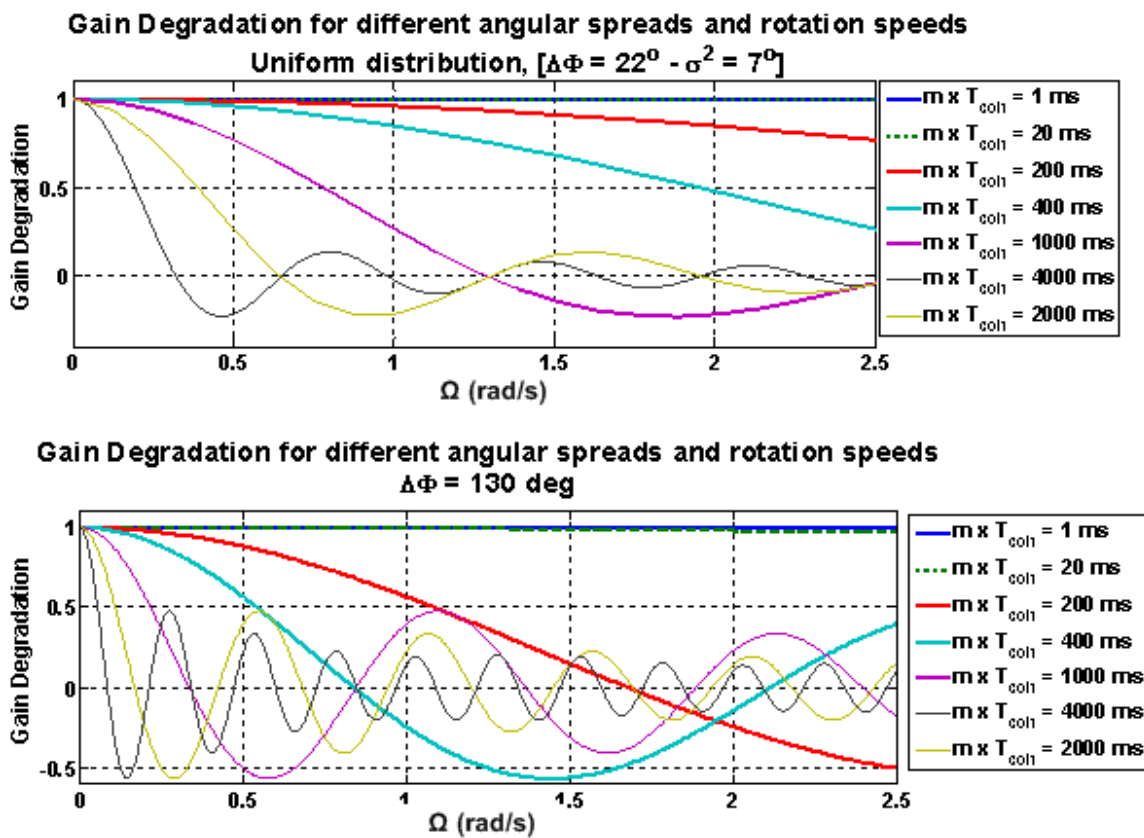




**Figure 4-18: Gain degradation for different distances between array elements and rotation speeds under two different uniform AS**

However, due to multipath, the associated GD is equal to 0.96 and therefore, the maximum achievable array gain is limited to 9.6 ( $AG = 10 \times \log_{10}(9.6) = 9.8\,dB$ ). By increasing the rotation speed of the array to $2\,rad\,/\sec \approx 19\,rpm$ under the same AS conditions, the GD rises to 0.85 and this reduces the limit of the achievable array gain to only 8.5 ( $AG = 10 \times \log_{10}(8.5) = 9.3\,dB$ ). This gain degradation is not significant as the rotation speed is slow and the AS is quite limited. However, under harsher multipath conditions, (for instance as illustrated in the second part of Figure 4-18) the same beamforming with only $1\,rad\,/\sec$ angular velocity results in a GD of 0.57, which limits the achievable array gain to about $7.5\,dB$ .

## 4.5 Summary

This chapter began by introducing the practical procedure to estimate the AoA. an in-depth description of array processing implementation and beamforming under multipath conditions was then presented. It was shown mathematically and through simulation-based procedures how phase wrap-up can deteriorate the AOA estimation profile and beamforming algorithms. The third section addressed how the antenna gain pattern affects the estimated AoA profile. It was also shown mathematically how both angular spread and the receiver motion can interact with each other to reduce the array performance.

**Chapter Five: Implementation of Synthetic Array and Experimental Results**

In Chapter 2 and Chapter 3 the GNSS signal structure and processing methods, multipath phenomena and modeling of the fading channel, the synthetic array processing methods, the beamforming and AoA estimation techniques were discussed. In Chapter 4, selected topics related to practical implementation issues of beamforming and AoA estimation such as the effect of the phase wrap-up and the antenna gain pattern were considered. To characterize the GNSS multipath channel, validate the discussed wireless channel models for the GNSS signals and assess the synthetic array performance under different multipath scenarios, live GPS signals were collected in real multipath fading environments. This chapter focuses on the experimental measurements, describing the goals, conditions and technical specifications of the data collection scenarios, as well as the results.

These experiments were designed to capture the signals using active GPS antennas on a rotating lever arm in the indoor environments, along with an outside reference antenna. After collecting the data with both reference and rover, they are simultaneously processed using GSNRx-rr$^{TM}$ (Satyarayana et al 2010), which wipes off any mutual systematic phase instability such as satellite motion and the receiver clock drift. Afterwards, the signal is fed into a series of developed codes to estimate the AoA, calculate angular spread, perform beamforming and measure the desired parameters. The data processing methodology was explained in detail in Section 1.6, and the main idea behind using a reference antenna was described in Section 3.2.

The examined environments include:
- Open sky conditions with no/low multipath

- An urban canyon with specular multipath

- A typical North American house that is associated with mild to severe multipath and fading conditions depending on the geometry of the satellites.

- A concrete office building on the U of C campus, with mild to severe multipath and fading conditions depending on the geometry of the satellites.

Figure 5-1 shows a schematic representation of the data collection layout and equipment.
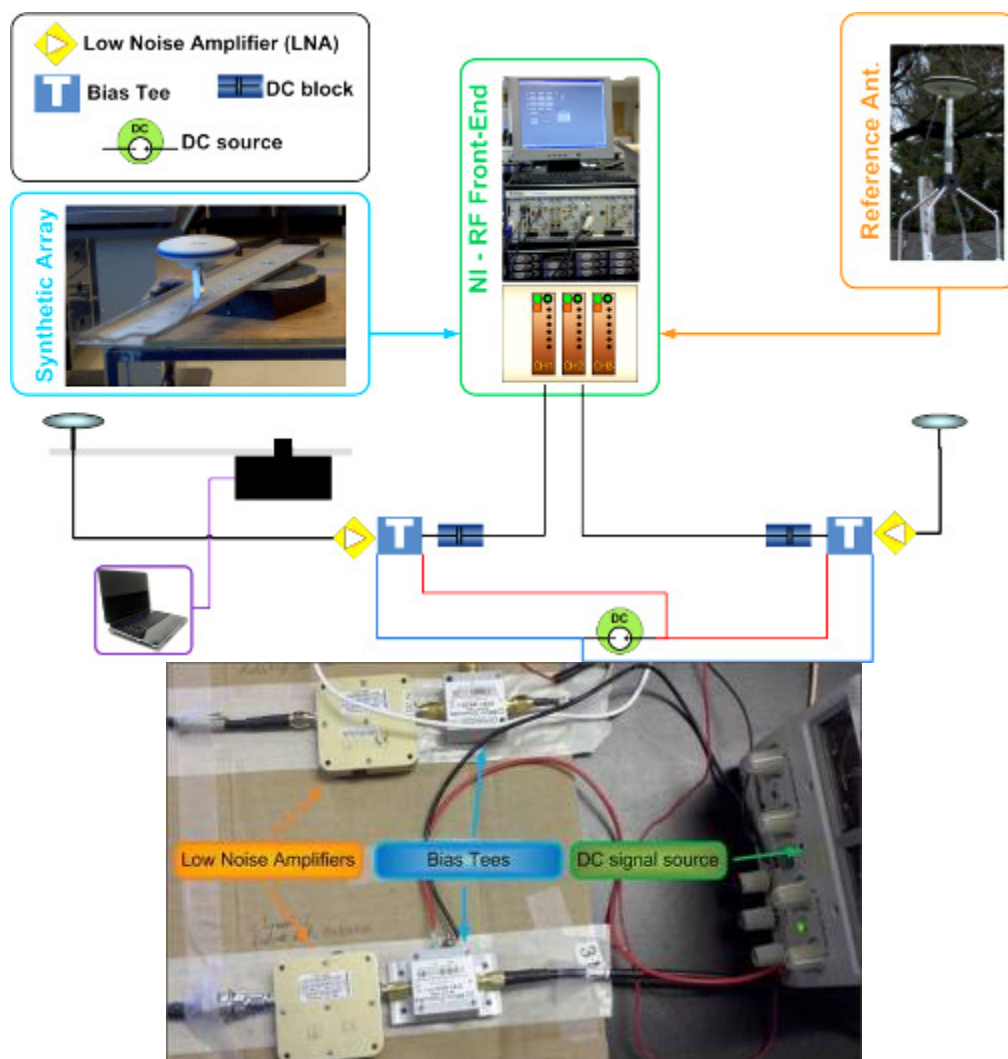


**Figure 5-1: Data collection equipment and layout**

Several sets of data were collected at each location and accurate and in-depth analyses were performed to measure the following parameters at each scenario:

- Channel fading model

- Signal spatial correlation coefficient and signal power level variations

- Angle of arrival and angular spread

- Array gain

A brief discussion of each of these parameters was presented in the previous chapters. The importance of incoming AoA and AoA distribution arises from the fact that the Doppler shift is mainly governed by this parameter, explained in Equation (4-5) as

$$
\begin{aligned}
f_d = f_{wrap-up} + f_{motion} &= \dot{\gamma}(t) + \frac{v}{\lambda}\cos\tilde{\theta}\sin(\phi) \\
&= \dot{\gamma}(t) + \frac{2\pi}{\lambda}R\dot{\gamma}(t)\cos\tilde{\theta}\sin(\phi - \dot{\gamma}(t).t)
\end{aligned}
\tag{5-1}
$$

Therefore, characterizing AoA and its distribution can lead to characterizing the Doppler characteristics, which is one of the main parameters that is to be estimated in the GNSS receivers. Therefore, the output of these measurements and the derived channel model can facilitate signal acquisition and tracking for modern GNSS receivers. Moreover, accurate characterization of AoA can lead to a redesigning of GNSS hardware such as antennas in multipath conditions. On the other hand, the fading model and variations of signal power can be useful to design the arrays and choose the optimal coherent integration time under multipath fading.

It must also be noted that in Chapter 4, the measured array gain was defined as

$$
AG = \frac{SNR_{out}}{SNR_{in}}.
\tag{5-2}
$$

Also, during this process, the signal is integrated coherently, while the noise integration is non-coherent and the output of the beamforming process of each sample is a complex number. Hence, Equation (5-2) can be simplified to

$$\mathrm{A}G = \frac{\left(a_{output}\right)^2}{M\left[\mu\left(a_{input}\right)\right]^2},$$  **(5-3)**

where $a_{output}$ is the value of the beamforming output, $M$ is the number of array elements and $\mu(a_{input})$ is the mean of the input signal amplitude. In fading conditions, other considerations to compute the signal mean are taken into account. However, to remain consistent for both the outdoor and indoor case, the definition in Equation (5-3) is adopted as the AG.

The following sections describe the implementation and analysis output of the collected data in the aforementioned situations. It must be noted that all the channel measurements were performed based on the complex correlator outputs, which hereinafter will be called the "signal" for simplicity.

Also, it must be noted that through this chapter the signal sample collected at each revolution of the synthetic array, or the synthetic array realization, is called the *sample*. Subsequently, each synthetic array realization or sample is made up of array snapshots and is basically a complex vector of signal snapshots, resulting from a coherent integration of signals at different positions. Therefore, each snapshot or element of the realization vector is simply called the *array element*. This is shown in Figure 5-2.
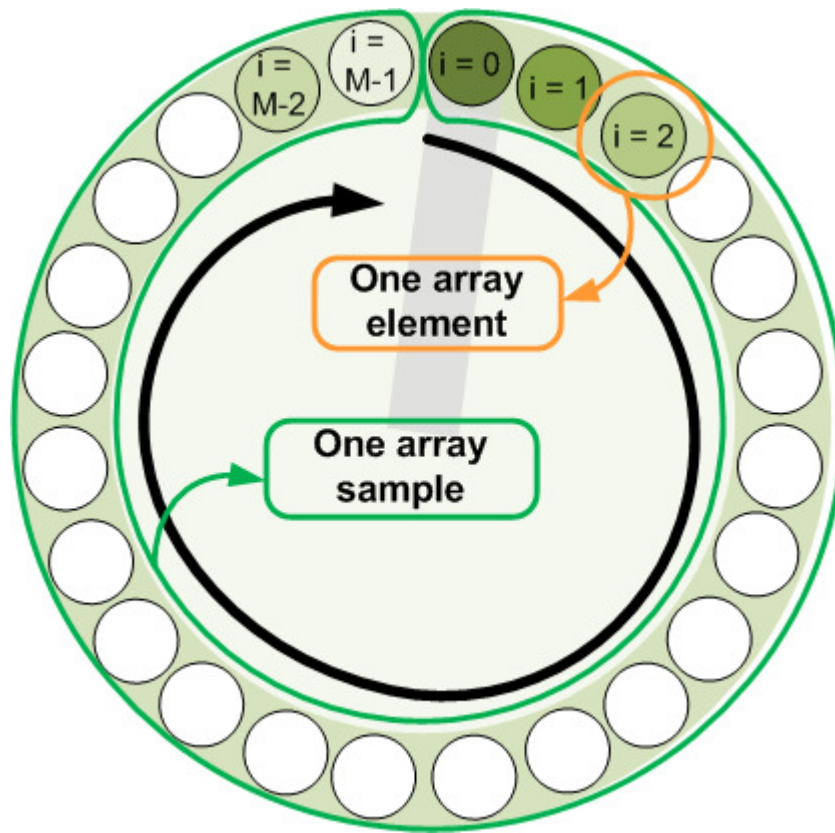
**Figure 5-2**: **Array sample comparing with array element**

## 5.1 Open sky conditions

In this situation, the rooftop of the CCIT building on the University of Calgary campus was chosen to collect the data to minimize the multipath effect. The main reason for collecting data under LoS conditions was to test and verify the designed algorithms and the synthetic array architecture. The data was collected in January 2010, the rotation rate of the synthetic UCA was 6 rpm, the data was processed with the GSNRx-rr with 20 ms of coherent integration time and this resulted in a UCA realization with 500 elements. Figure 5-2 shows the data collection location, corresponding skyplot, signal level of the available satellites along with the technical specification of the data collection and processing.

During this data collection, the observed inconsistencies between the expected AoA estimation and achieved AG and the measured AoA and AG are due to the phase wrap-up effect. The detailed effects of phase wrap-up on the array performance, along with the mathematical foundations to compensate for this effect were discussed in Section 4.2. While in Chapter 4 a simulation based approach was taken to characterize this effect, in Section 5.1.1 the actual effect of the phase wrap-up along with the calibration approaches in practical situations are presented.
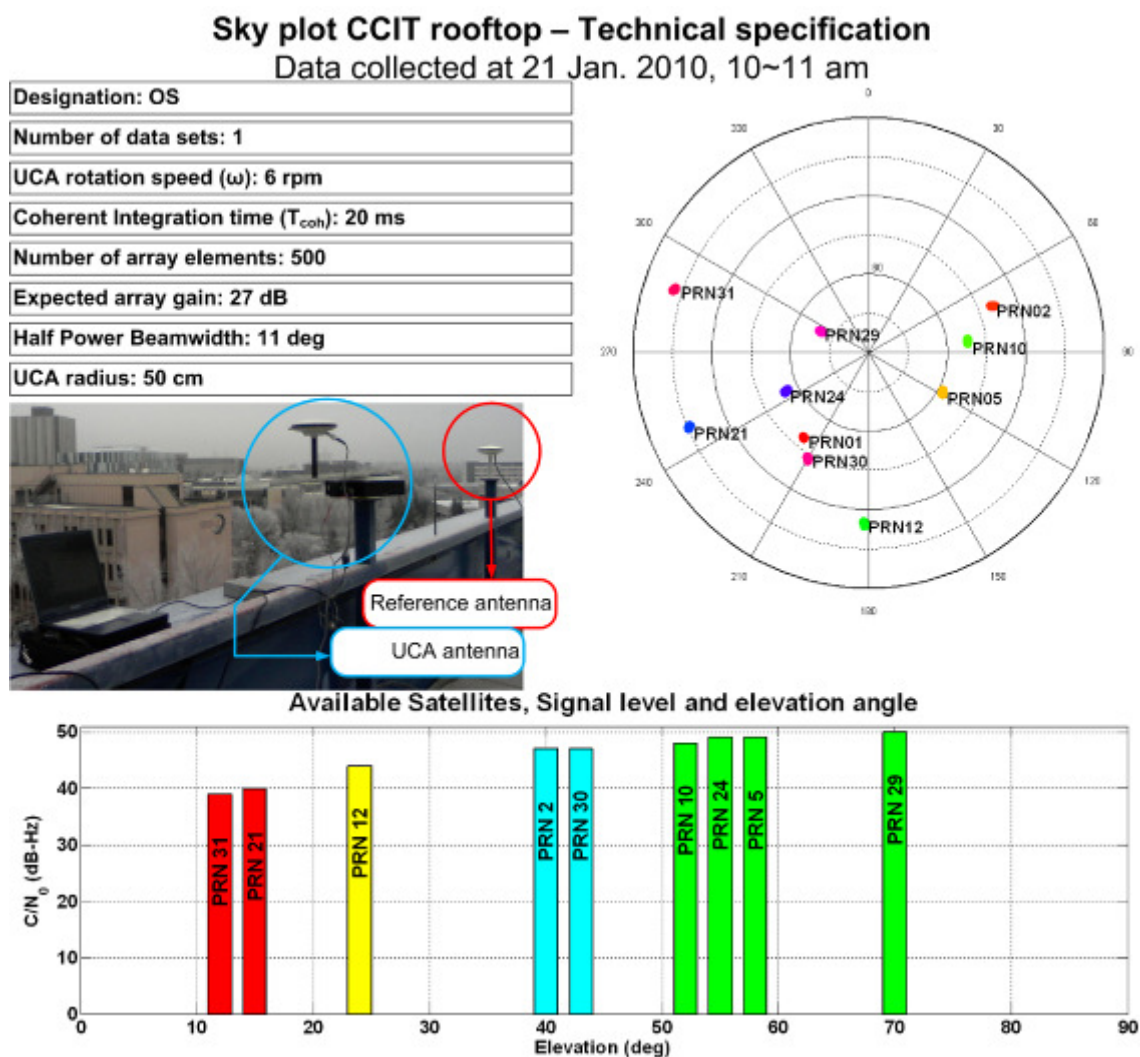


**Figure 5-3: Technical specifications of data collection and analysis under Open Sky**

### 5.1.1 Phase Wrap-Up

Through this data collection, the antenna was completely fixed to the rotating lever arm. Therefore, the antenna also rotated during the rotation of the lever arm, which resulted in the generation of an additional Doppler shift. Figure 5-4 shows the carrier phase of the received signal from several PRNs located at different elevation and azimuth angles. As can be seen, the results completely comply with the theoretical model of Equation (4-4) and Figure 4-9 whereby the carrier phase wrap-up is independent of the satellite's elevation angle and the azimuth angle only impacts the initial received phase. In other words, the experimental results verify that the only key factor in the magnitude of the phase wrap-up (or the slope of the ramp) is the rotation rate of the antenna $\dot{\gamma}$. It can be seen that the phase wrap-up due to a 6 rev/min (= 0.628 rad/s) rotation rate results in almost 63 radian (after 10 cycles, 100 seconds) of shift in the received carrier phase; that is exactly equal to the value that is shown in Figure 4-7 and Figure 4-9.
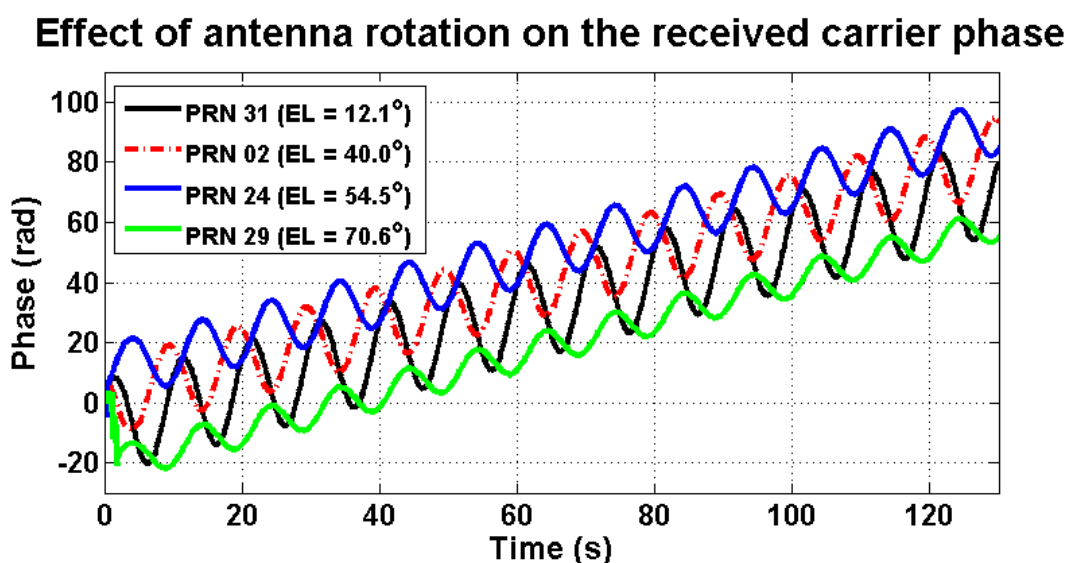


**Figure 5-4: Received phase of a signal corrupted by phase wrap-up (Open Sky)**

Moreover, the effect of the antenna rotation (carrier phase wrap-up) on AoA estimation accuracy is shown in the first part of Figure 5-5 as one of the performance measures of the array. As can be seen, phase wrap-up corrupts the AoA spectrum through an additional Doppler shift that is not accounted for. The resulting effect on AoA profiles is also shown in the first part of Figure 5-6. It is evident that phase wrap-up can lead to extreme errors in the AoA estimation accuracy. However, based on the equations presented in Chapter 4, this effect can be measured and corrected for precisely. The AoA spectrum and distribution for PRN 29 before and after correcting for the phase wrap-up effect are shown in the second part of Figure 5-5 and Figure 5-6 respectively.
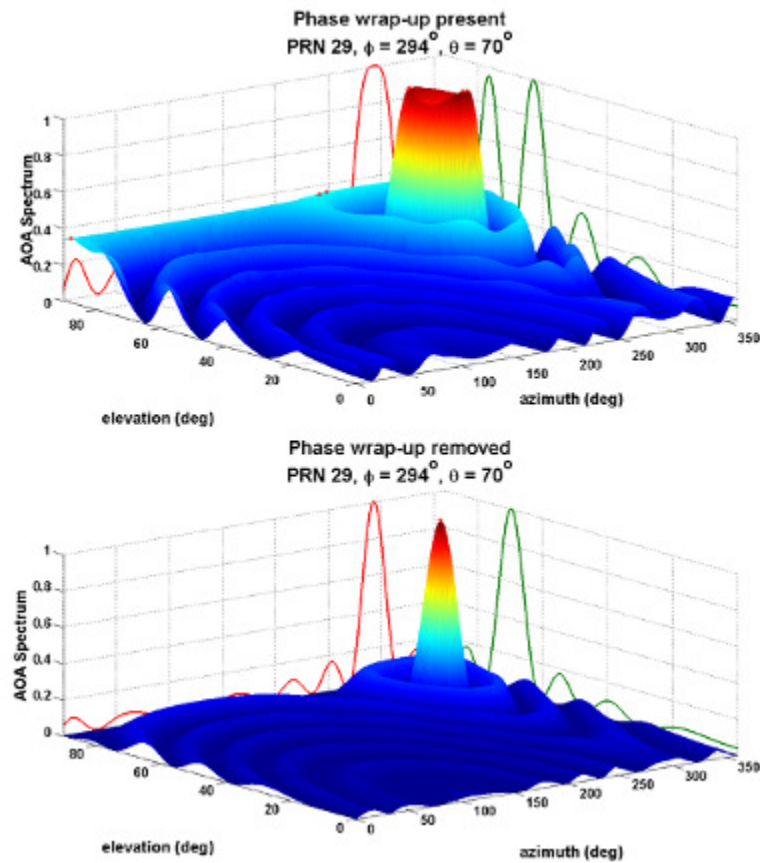


**Figure 5-5: a) AoA spectrum under phase wrap-up, b) AoA spectrum after removing phase wrap-up**

In this case, removing the phase wrap-up is a straight forward procedure due to the constant angular velocity of the array that merely imposes a constant Doppler shift on the received carrier phase. This correction results in the expected array gain and correct AoA estimation.
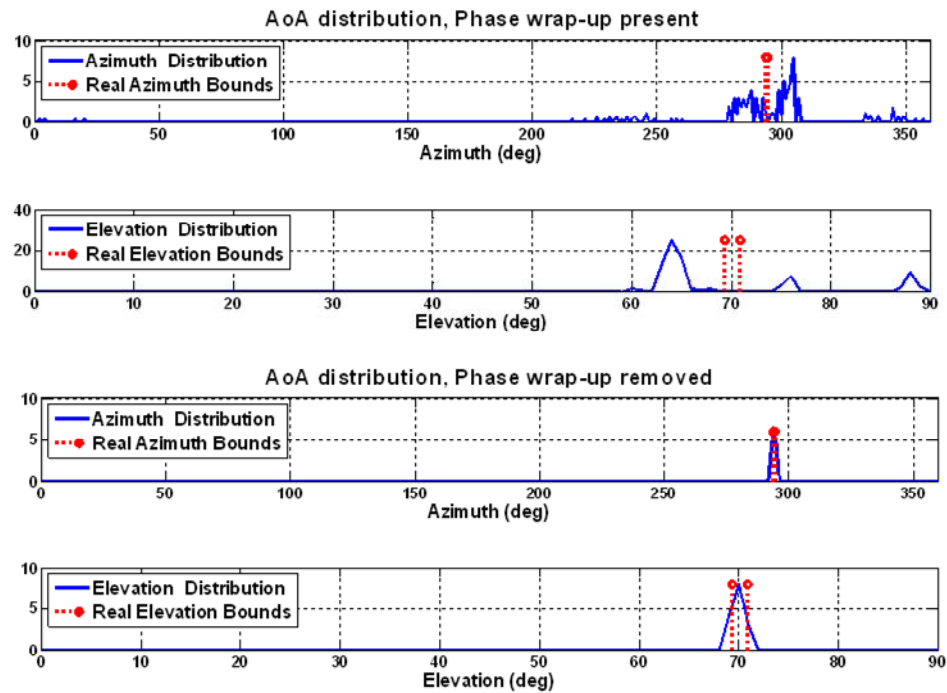


**Figure 5-6: Estimated AoA distribution before and after phase wrap-up removal**

However, for the case of pedestrian, vehicular and aviation applications, the velocity, antenna axial heading changes and rotations are not constant anymore. In such cases, further considerations must be taken into account to measure the unknown phase variations to maintain the desired accuracy. For instance, one possible solution is using gyroscope outputs to measure antenna rotations and aid the GNSS receiver to wipe off the carrier phase using the theoretical findings presented in Section 4.2.. Also, it must be

noted that the measurements and results presented in the sequel are based on signals that are corrected for the carrier phase wrap-up as described above.

### *5.1.2 Channel Model*

A brief discussion of the fading channel distribution models was presented in Sections 2.5 and Section 2.6. As discussed previously, due to the pure LoS conditions, it is expected that the governing channel model be Rician with typically large K-factors in dB. Figure 5-7 shows the normalized signal amplitude distribution for selected PRNs. To generate this figure, all the measured signal amplitudes from all samples are normalized with the maximum value of the signal amplitude of PRN 29 since, due to its very high elevation angle, it possesses the highest signal level.

It must be noted that the signal power is the magnitude of the correlator output and is shown as $a = \sqrt{I^2 + Q^2}$ .
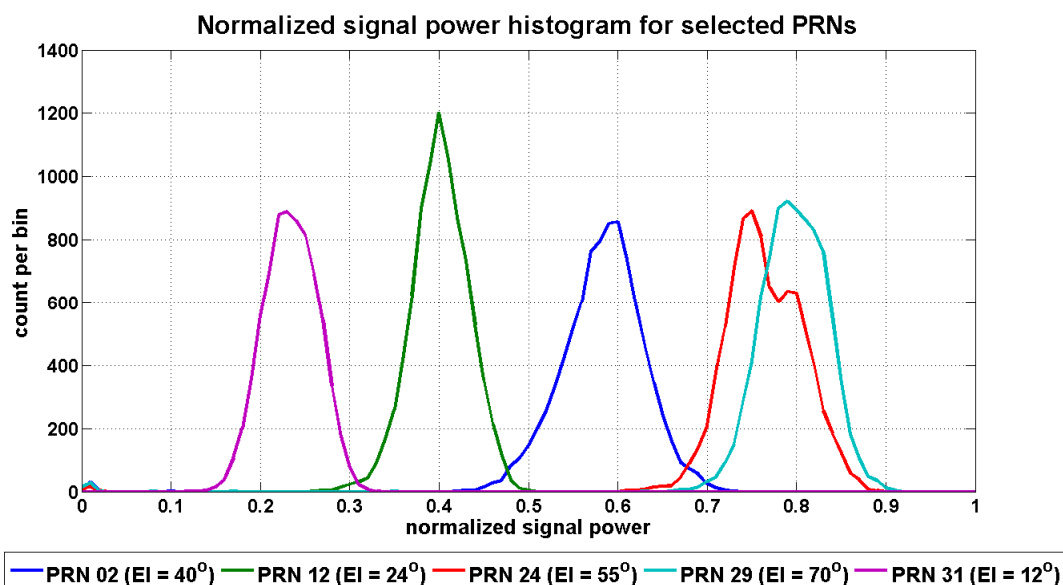


**Figure 5-7: Normalized signal power distribution – Open Sky conditions**

Figure 5-8 shows three different fits to the measured signal amplitude distribution. These fits include the Rician, Normal and Rayleigh distributions. As can be seen, the closest resemblance is that of the Rician distribution (that practically approaches the normal distribution in the LoS conditions, shown here only for comparison). Moreover, Figure 5-9 shows the measured Rician K-factor in this situation. It must be noted that, as can be seen, in the outdoor environments, the dominant channel model is Rician with relatively strong LoS components. It is also noteworthy to remember that the Rician K-factor is explained in Section 2.6.2 as

$$K = \frac{LoS\ signal\ power}{Multipath\ components\ power} = \frac{\mu^2}{2\sigma^2},$$ 

(5-3)

which is the ratio between the LoS component amplitude and the multipath components' amplitude. In the current work, $\mu$ and $\sigma$ are measured using the MATLAB$^®$'s "Distribution Fitting Toolbox".
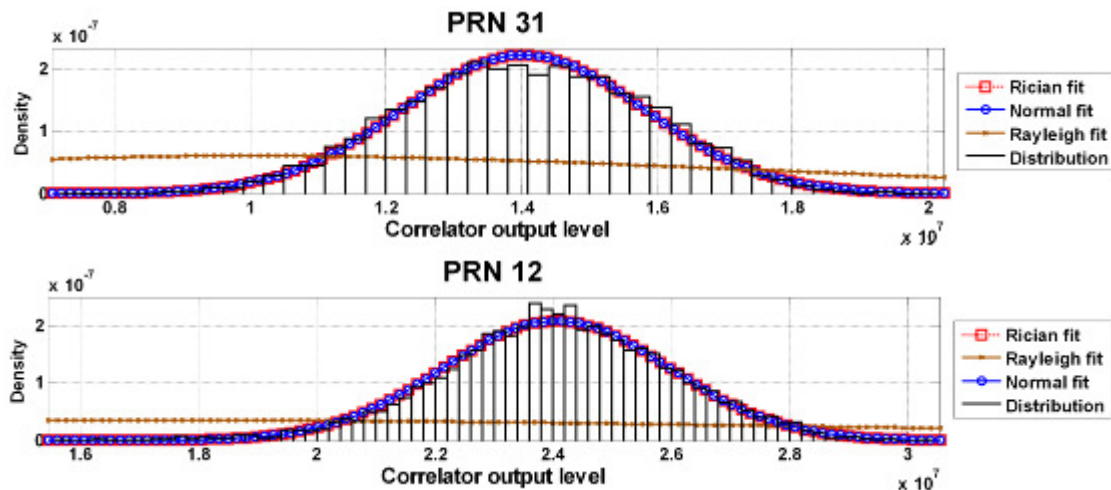


**Figure 5-8: Rician, Normal and Rayleigh fits to the signal envelope of selected PRNs – Open Sky conditions**
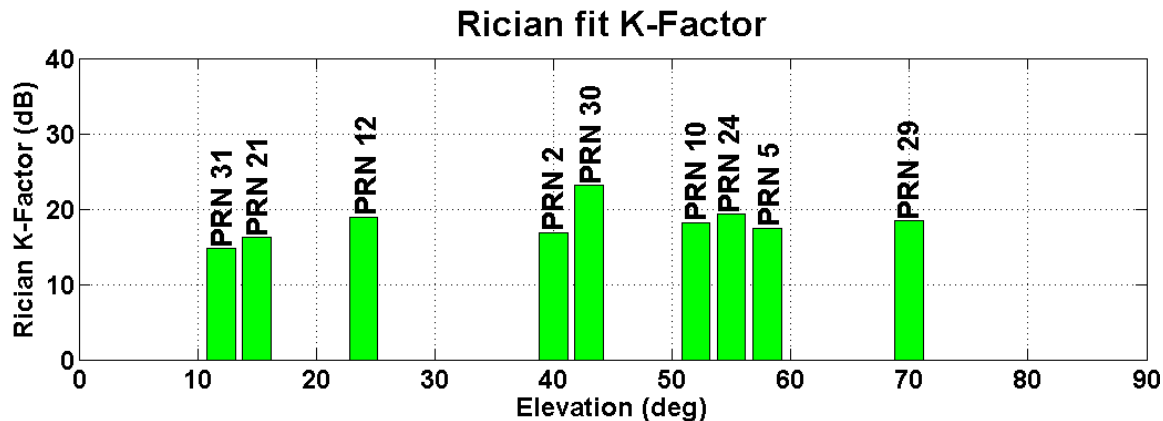
**Figure 5-9: Measured K-factors for open sky, Open Sky conditions**

### 5.1.3 Correlation Coefficient and Signal level variations

The signal correlation coefficient was discussed in Section 2.5 and is an important measure of the propagation channel. Its importance was discussed in Section 3.6, where it was shown that the array gain is directly proportional to this parameter as described by Equation (3-26). Herein, Figure 5-10 shows the signal correlation coefficient of 15 samples, for selected PRNs.
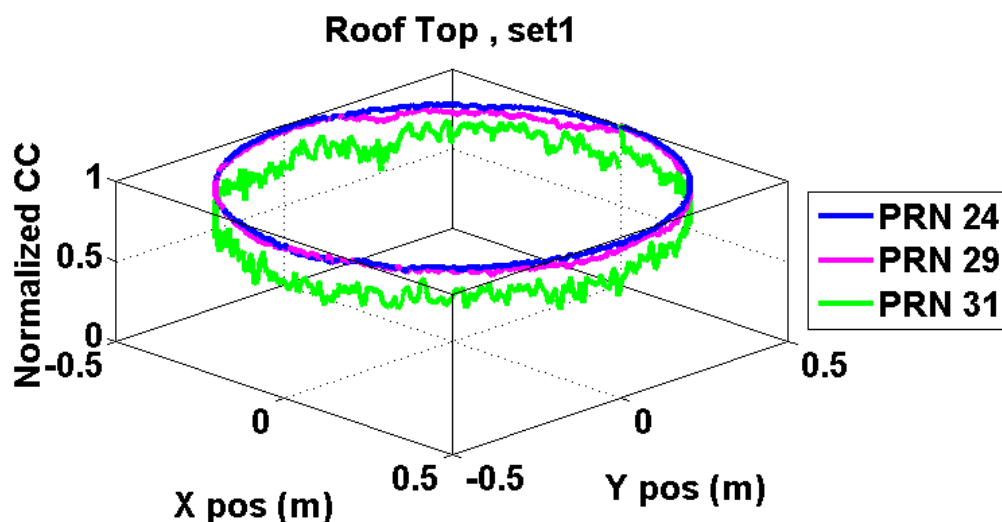


**Figure 5-10: Signal correlation coefficient under Open Sky conditions**
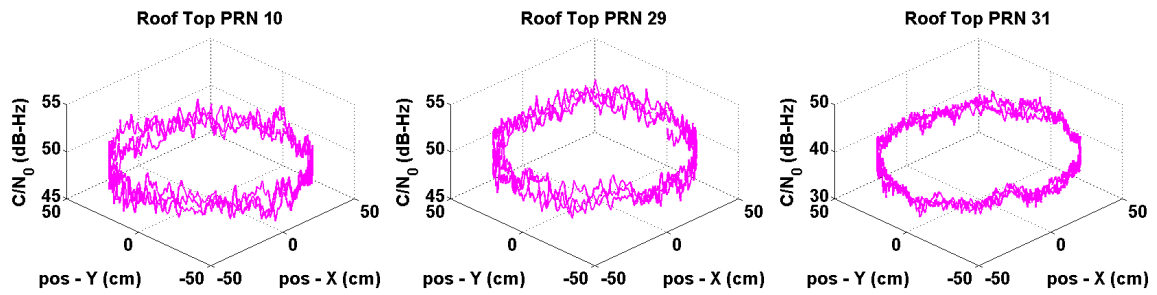
**Figure 5-11: Signal level variations of 3 samples for selected PRNs – Open Sky**

As shown in Figure 5-10, all the signals have high correlation coefficients close to one that is in excellent consistency with high array gains.

Also, as can be seen in Figure 5-11, even for very low elevation satellites (e.g. PRN 31) the signal level maintains its mean value for several successive samples and signal level variations are almost negligible. As Figure 5-11 shows, there is no sign of deep fades; this indicates that the signal is not affected by multipath.

### 5.1.4 AoA distribution and AS modeling

Several models have been proposed for the AoA distribution of the electromagnetic waves in different multipath situations. Unfortunately, none of these models are associated with the GNSS signal frequency and amplitude range. As stated in Chapter 1, one of the main goals of this research is to characterize the AoA distribution of the GNSS signals in a multipath environment. However, open sky conditions, with known array position and known LoS direction provide a reliable tool to ensure the correctness of the algorithms and the developed code. Hence, to ensure that the beamforming and AoA estimation methods are working properly, in this section the AoA estimation outputs for all available PRNs from low to high elevation angles are plotted and compared with the actual angles shown in Figure 5-12. The solid blue lines show the

estimated angle of arrival distribution and the dotted lines represent the elevation and azimuth of the satellite at the beginning and the end of the data collection.

As can be seen, the estimated AoA profile matches very well for most of the cases with the real elevation and azimuth of the satellites within the data collection time. The only considerable difference is for PRN 31, where the inconsistency may arise from the lower accuracy of the estimation method at very low elevation angles. The latter can be further investigated by studying the Cramer-Rao bounds for Beamscan.

### *5.1.5 Array Gain*

An extensive review of the beamforming and array gain concepts was presented in Sections 3.3 to 3.5. It was shown that under LOS conditions, the array gain should reach the number of array elements $M$, which is the number of elements in the array. As described in the introduction of this section, for the current condition, $M = 500$, which means that if the beamforming process is performed correctly, the signal should be amplified 500 times. In other words, the resulting relative AG in dB scale should be equal to $AG|_{dB} = 10\log_{10}(500) = 27\,dB$. Figure 5-13 shows the achieved array gain for several samples of the current data set. As can be seen, the implemented beamforming method achieves the expected array gain.
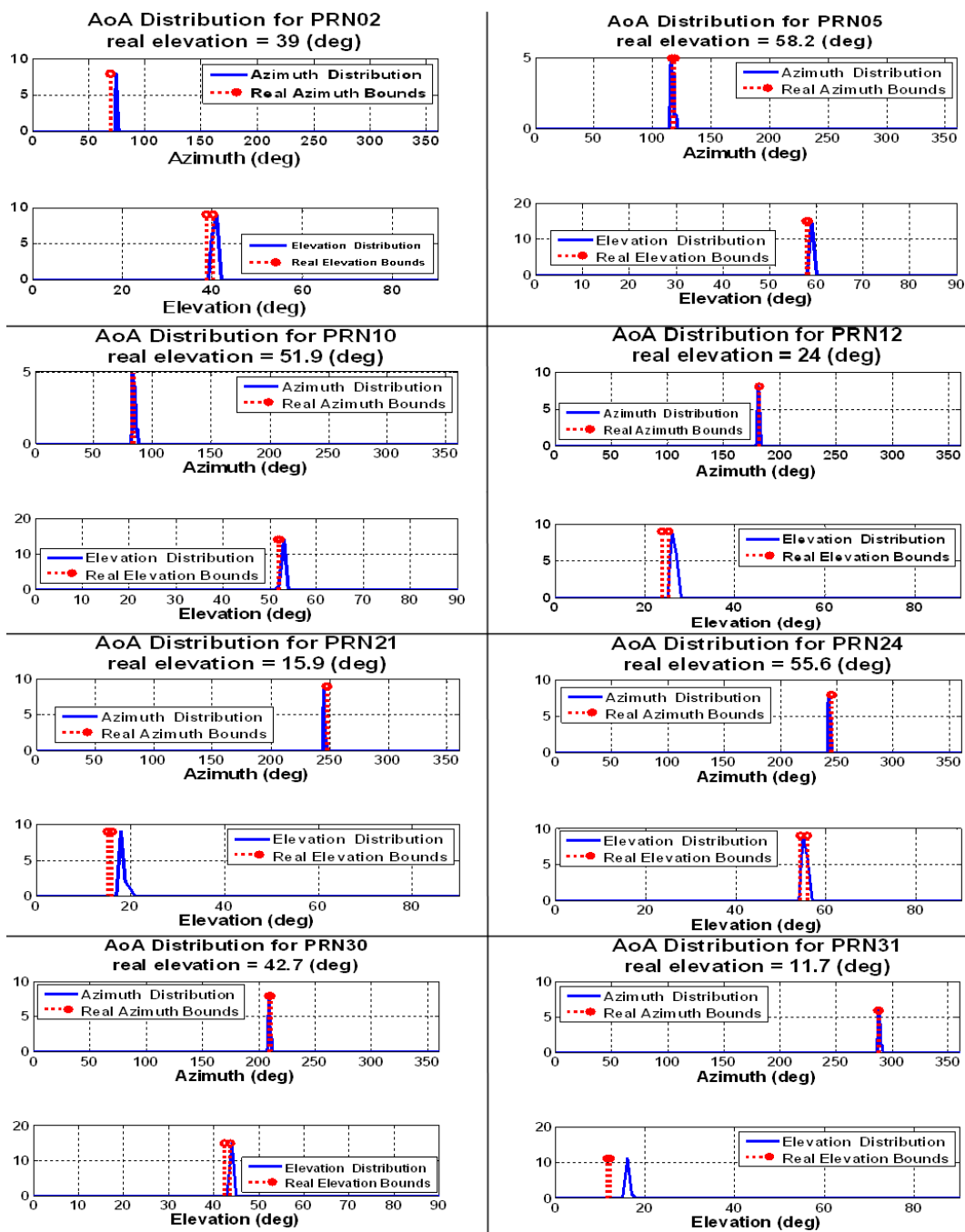
**Figure 5-12: AoA distribution for all PRNs under open sky conditions**
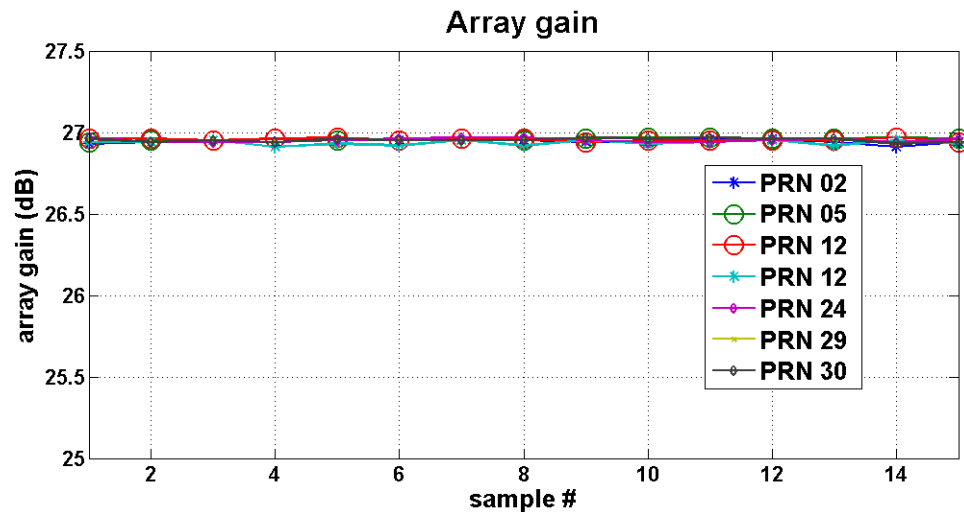
**Figure 5-13: Achieved array gain under Open Sky conditions**

### 5.1.6 Concluding Remarks

The goal of this section was to assess the performance of the utilized technique under known signal parameters (such as the AoA) of the proposed concepts and methodologies. As discussed, after removing the effect of the phase wrap-up, the implemented array processing methods perform correctly and the results perfectly comply with the expected results. Also, it was shown that under open sky conditions the dominant channel model is Rician with high K-factors, signals spatially decorrelate slowly, the $C/N_0$ levels are high and stable spatially, AS is zero and the array gain reaches its nominal value.

## 5.2 Urban Canyon

To assess the urban canyon multipath environment, the data collection equipment was taken outside of the ICT building on the U of C campus on November 4, 2010. Various obstacles surround this particular area, as shown in Figure 5-14. To the north, the Energy Environmental Experimental Learning (EEEL) building is covered with metallic

panels, to the west, the Information and Communications Technologies (ICT) building is covered with metallic panels and reflective windows, to the east, the Earth Science building (ES) is covered with concrete and, finally, the link between the ICT and ES buildings is covered with the same material as the ICT and EEEL buildings. In this particular scenario, the EEEL and ICT buildings reflect signals from the south and southeast respectively, and provide specular multipath. The ES building blocks signals from the east and the link between the ICT and ES buildings blocks low elevation signals from the south. Therefore, this situation incorporates LoS signals that are contaminated with multipath components.

It must be noted that in this data collection, phase wrap-up was avoided by fixing the antenna orientation towards the north during the rotations of the synthetic array. The rotation speed was 6 rpm and the data was pre-processed using the GSRNx-rr software receiver with a coherent integration time of 20 ms that results in the same number of array elements and expected array gain as the previous case. The corresponding skyplot and other technical aspects of the data collection and analysis are shown in Figure 5-14. Also, in this scenario, two sets of data were collected with two different radiuses of 55 and 70 cm, each containing more than 25 samples.

### 5.2.1 Phase measurements

Under LoS conditions, the circular motion of the mobile antenna creates a sinusoidal trend in the received phase (according to Equation (4-3)). However, as mentioned earlier, multipath could have deteriorating effects on the received signal phase. Therefore, to assess the effect of multipath on the received phase, this quantity for the first set of data is shown in Figure 5-15.

## Sky plot Outside ICT Bldg. – Technical specification
### Data collected at 04 Nov. 2010, 10~11 am

| |
|---|
| Designation: IO |
| Number of data sets: 2 |
| UCA rotation speed (ω): 6 rpm |
| Coherent integration time ($T_{coh}$): 20 ms |
| Number of array elements: 500 |
| Expected array gain: 27 dB |
| UCA radius: 55, 70 cm |
| Half Power Beamwidth: 10.5 , 7.7 deg |
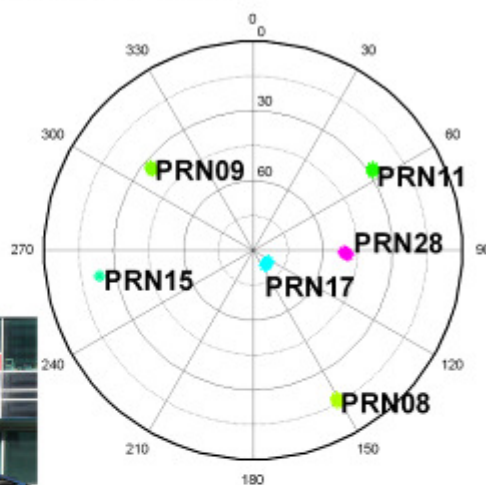


### Selected Satellites, Signal level and elevation angle
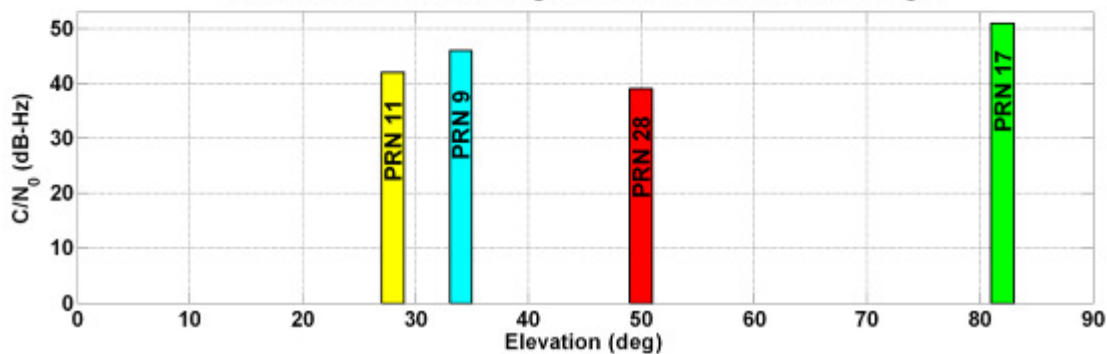


**Figure 5-14: Skyplot, signal level of available satellites and technical specifications of data collection and processing for urban canyon case**
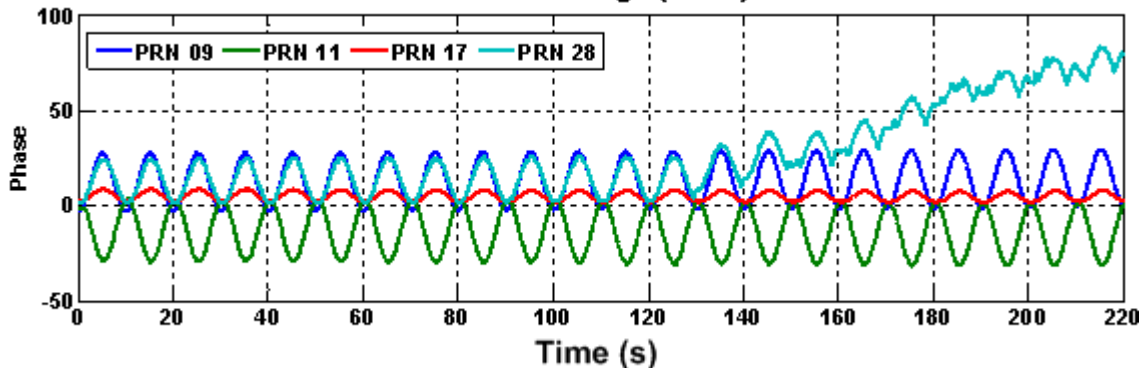


**Figure 5-15: Received signal phase for the Urban Canyon case**

As can be seen, as PRN 28 sets behind the ES building, the received signal phase starts deviating from its mean value and loses its periodic trend.

### 5.2.2 Fading Channel Model

In this situation, the signal broadcasted by PRN 17 has the highest amplitude. Therefore, the signal amplitudes of all PRNs are normalized to the maximum value of PRN 17's amplitude. The output is plotted in Figure 5-16. Based on this figure, PRN 17 and PRN 28 represent two extreme cases of the channel model. PRN 17 has a Rician model with a relatively high K-factor and PRN 28 seems to have a Rayleigh fading model. Figure 5-17 and Figure 5-18 show Rician and Rayleigh fits to the signal level distribution of the corresponding signals and also the calculated Rician K-factor for the two signals, respectively.
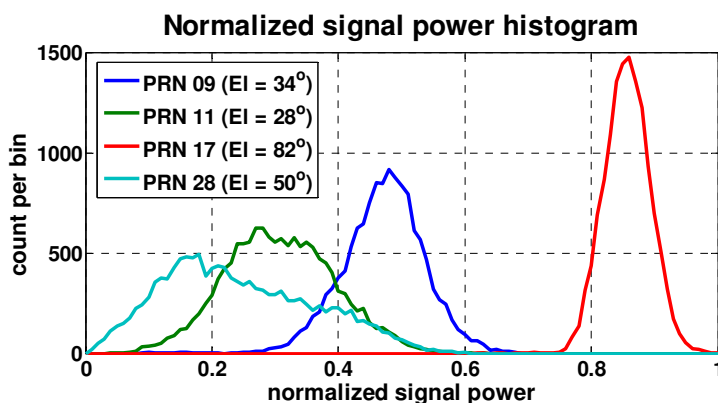


**Figure 5-16: Normalized signal distribution**

### 5.2.3 Correlation Coefficient and Signal Power Variations

The fundamentals of measuring complex correlation coefficients were explained in detail in previous sections. Figure 5-19 shows the correlation coefficient measurement for the first data set (containing 25 samples) in this location.
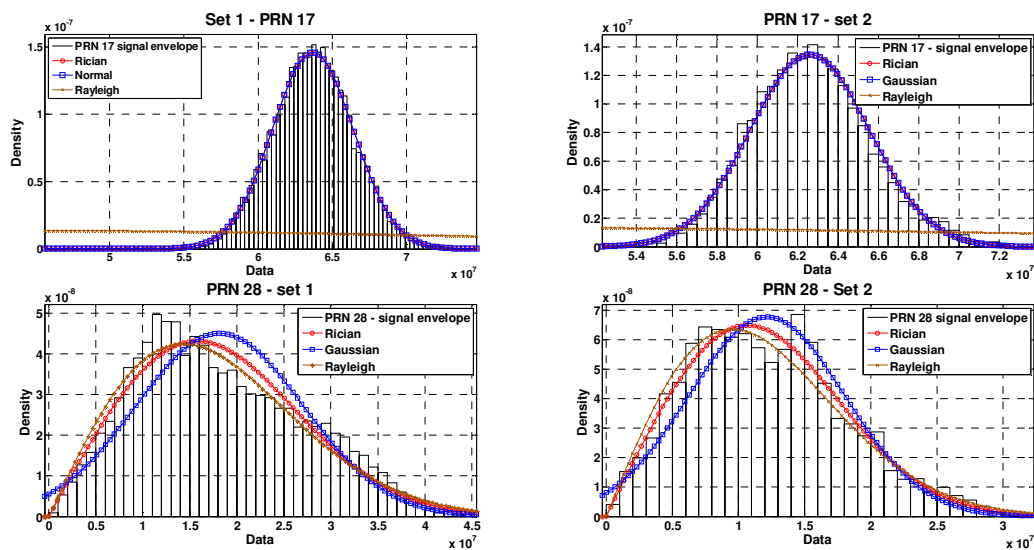
**Figure 5-17: Rician, Normal and Rayleigh fading fits to PRN 28 and PRN 17 – Urban Canyon**
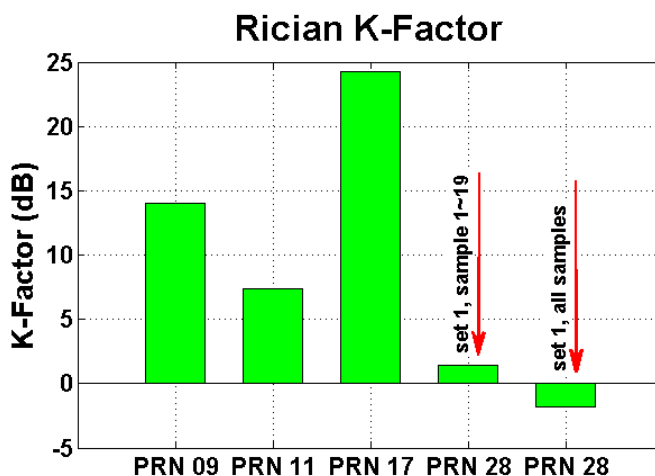


**Figure 5-18: Rician K-factor of PRN 17 and PRN 28 – Urban Canyon**

Figure 5-20 shows the signal level variations of PRN 28 and 17 for the first and the last three samples of data set 1. While it can be seen that through all samples, PRN 17 has maintained its level about a mean value, the signal broadcasted from PRN 28 has undergone fading. This conforms to the results regarding the correlation coefficient. Also, since the signal is getting faded over time, the power level variations get worse and more sections of the trajectory fall in deep fading.
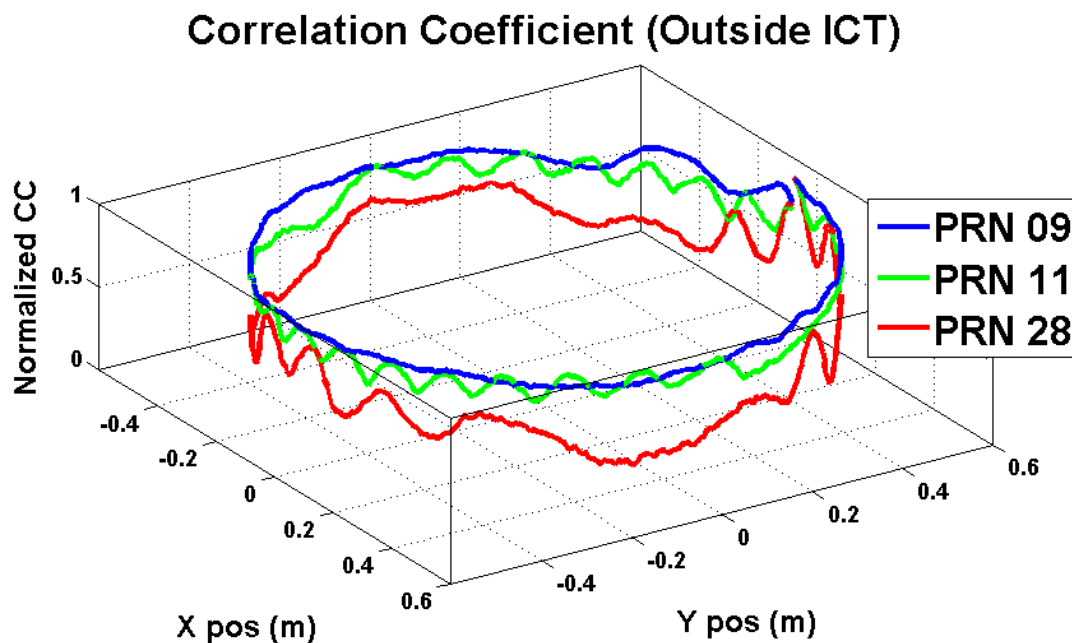
**Figure 5-19: Signal correlation coefficient for PRN 28 – Urban canyon**
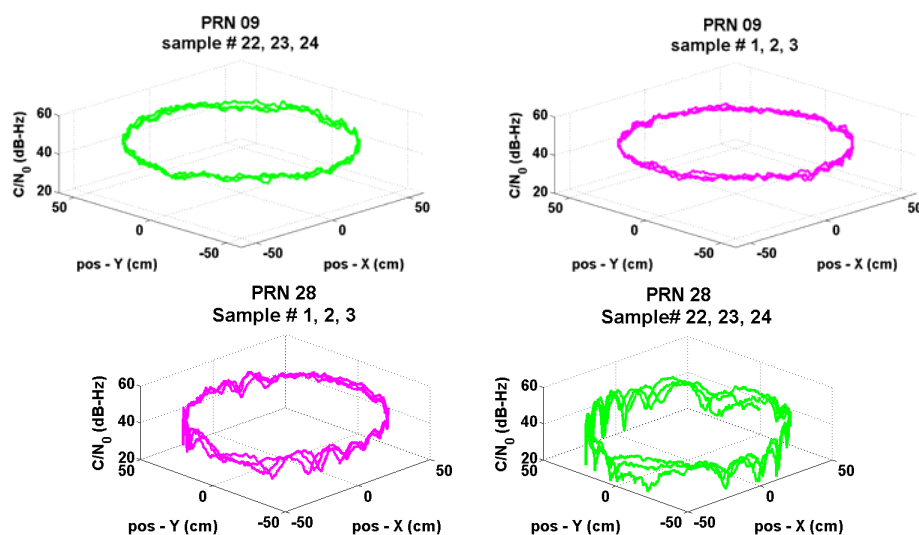


**Figure 5-20: Signal level variations – Urban canyon**

The behaviour of PRN 28, which is under mild multipath interference, shows that the wireless channel of this signal is somewhat invariant in the time domain. Also, minor instabilities observed in the signal level of this PRN for sample 22, 23 and 24 can be

related to changes in the surrounding environment (e.g. passing of a vehicle or a pedestrian).

### 5.2.4 AoA, AS and AG characterization

In these data sets, PRN 17 is located at a very high elevation angle and, by considering the landscape of the surroundings, this guarantees that this signal undergoes minimal multipath fading when compared to the other satellites. Among the rest of the PRNs, the variation of the AoA spectrum for PRN 28 is interesting since, as it is shown in Figure 5-15, at the first section of data the LoS signal is available and then it falls into fading. As it is shown in the first plot of Figure 5-21, for the first several samples of data set 1, the signal has one distinct peak in its AoA spectrum which is aligned with the true LoS direction. Nevertheless, the small peak corresponding to a multipath component can be seen in this plot. However, after almost 20 samples, the LoS signal starts getting weaker and the multipath components start governing the channel and their corresponding peaks start to get higher (compared to the LoS peak) as shown in the second plot of Figure 5-21. Finally, in the last samples of data set 1, as shown in the third plot of Figure 5-21, the multipath components are stronger than the LoS signal and their corresponding peaks possess higher signal levels. The overall estimated AoA distribution for PRN 9, 11 and 17 are presented in Figure 5-22. As it is shown for some cases, multipath has caused significant inconsistencies between the incoming AoA of the signal and the real LoS of the satellite. Also, studying the variations of AG for all PRNs is interesting and is shown in Figure 5-23.
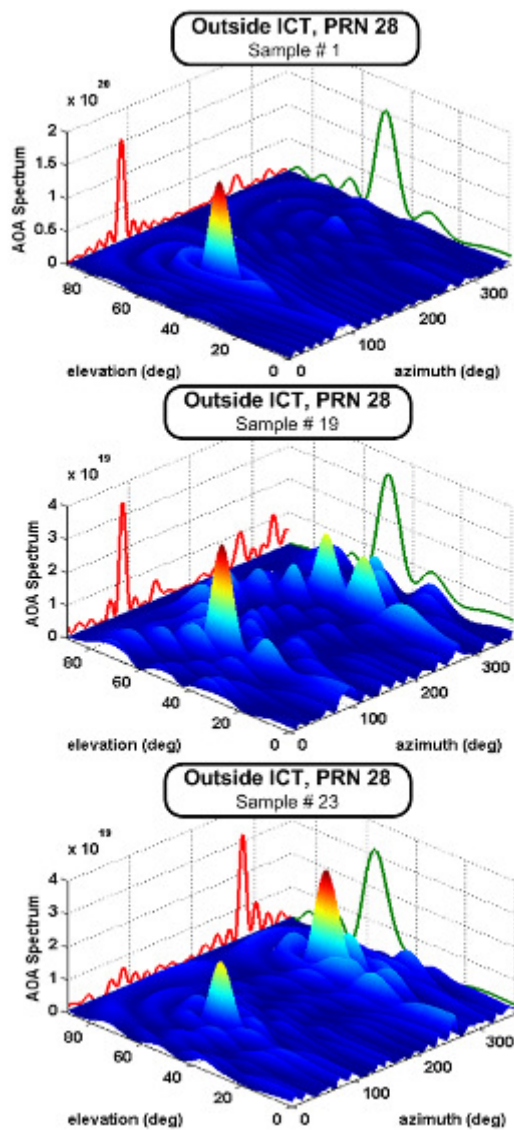
**Figure 5-21: AoA spectrum variations of PRN 28 with time – Urban Canyon**
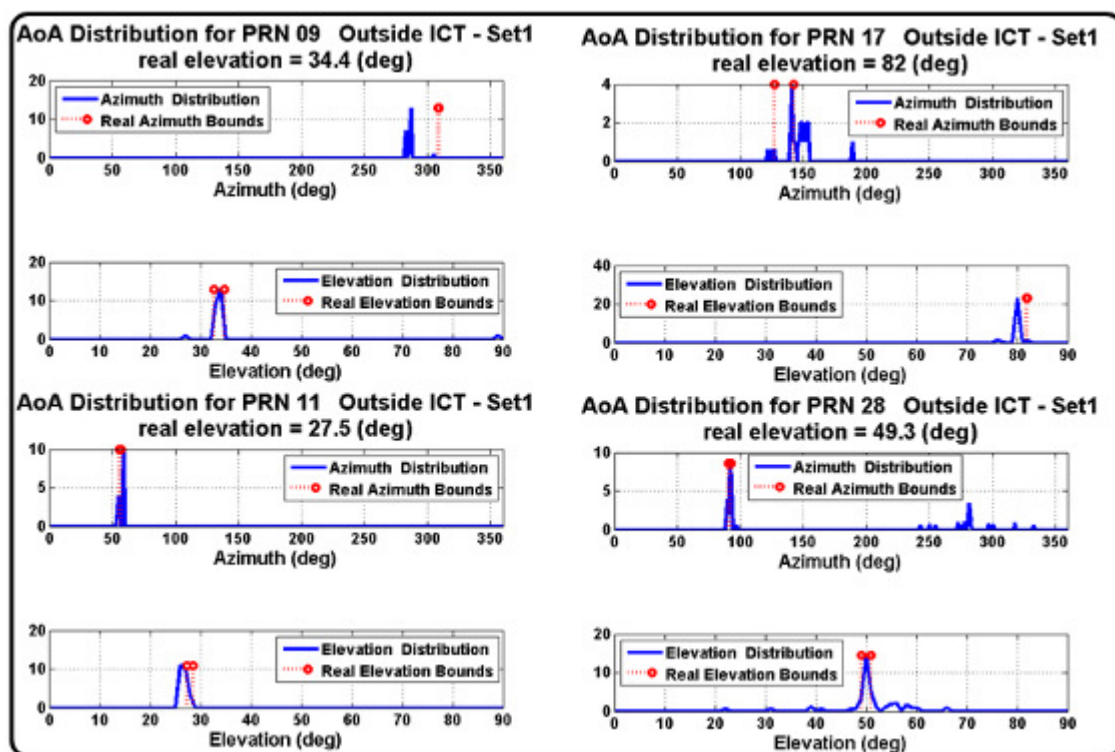
**Figure 5-22: AoA distribution for selected PRN, dataset 1, Urban Canyon.**
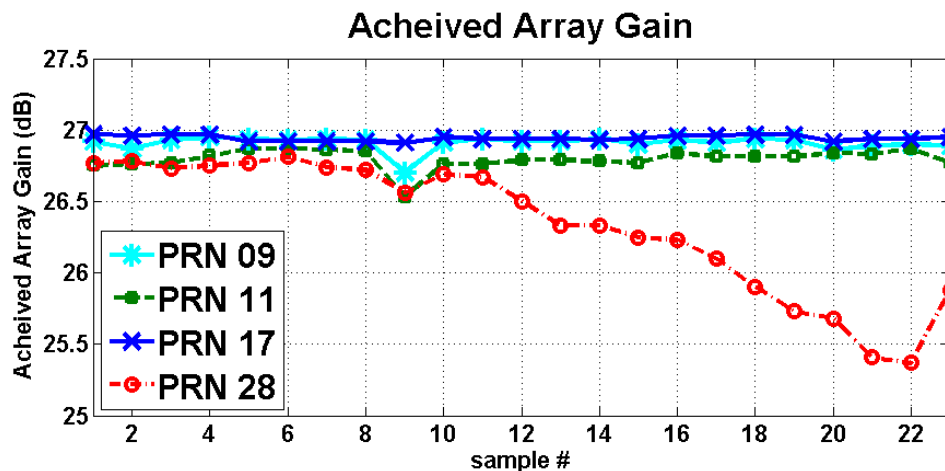


**Figure 5-23: AG variations, all PRNs, set 1 – Urban Canyon**

The decreasing trend of AG for PRN 28 can be tightly related to signal deterioration by multipath as shown in Figure 5-15.

### *5.2.5 Concluding Remarks*

This data collection scenario aimed to characterize the GPS channel under the specular multipath scenario. It was observed that, as the signal of PRN 28 gets more corrupted with multipath components from the ICT building and over time as it falls behind the ES building, the multipath components begin dominating the channel. During this, the AS increases and the signal correlation coefficient decreases gradually. It is also interesting to note that this AG drop occurs at exactly the same time that the phase deteriorations happen. Besides AoA, AS, AG and the signal's phase, changes of signal power and correlation coefficient that led to AG degradation were also investigated.

## 5.3 Residential structures

This data collection was to characterize the GNSS channel in typical North American residential structures, which are mainly made of wood and are covered with various construction materials. Therefore, the data collection equipment was taken to a basement suite of a private home in Calgary. The data collection location, corresponding sky plot and technical characteristics of the data collection and processing are shown in Figure 5-24. Another important aspect of this data collection was to assess the effect of the antenna pattern on the AoA estimation performance and the resulting AS. This effect has been addressed theoretically in Section 3.5 and Section 4.3. For this goal and as mentioned in Section 4.3, two different GPS antennas have been considered, namely the NovAtel 701/702 GGL series and the Ublox M-335 antennas. Two sets of data with over 40 samples were taken in order to have enough samples to construct statistically reliable distributions.

**Figure 5-24: Technical details, skyplot, location and signal level of the wooden house data**

First, the data was collected with the NovAtel antenna and, after completion, adjusting the antenna's operating voltage, fixing the Ublox antenna to the rotating table and other considerations, the second set of data was collected. Therefore, to address the differences between the two data sets, a slight time gap should be considered. The UCA radius for both cases was 36 cm, the rotation speed was the same as previous scenarios (6

rpm) and the coherent integration time was set to 200 ms, which resulted in 50 snapshots

per sample that were each 4.5 cm apart.

### 5.3.1 Fading Channel Model

The measured signal amplitude distributions for both cases for selected PRNs are

shown in Figure 5-25 for both antennas. Also, as for the other data sets, the Rician and

Rayleigh fits to these distributions are shown in Figure 5-26.
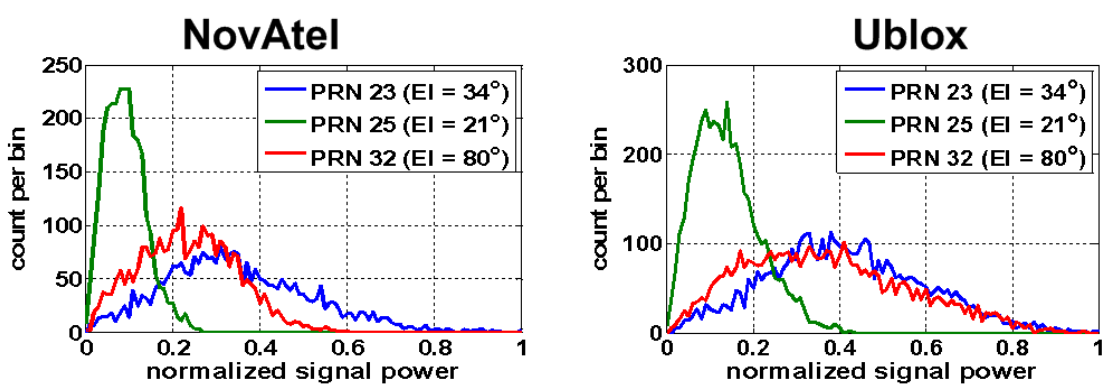


**Figure 5-25: Normalized signal amplitude distribution, select PRNs – Wooden House**

Based on the Rician distribution model, the K-factors of these PRNs are

calculated and shown in Figure 5-27. As expected, since the fading and K-factor are the

channel parameters, the antenna pattern does not have any significant effect on them. The

differences between the outputs for PRN 20, PRN 25 and PRN 30 may be related to the

change in the geometry of the receivers and hence the signal qualities.

As can be seen, in this environment the fading level varies from +1.8 dB to -7.7

dB for the many samples in terms of K-factor. However, there are some cases where, due

to geometry and the surrounding environment, the signal level drops to the range of -50

to -60 dB K-factor.
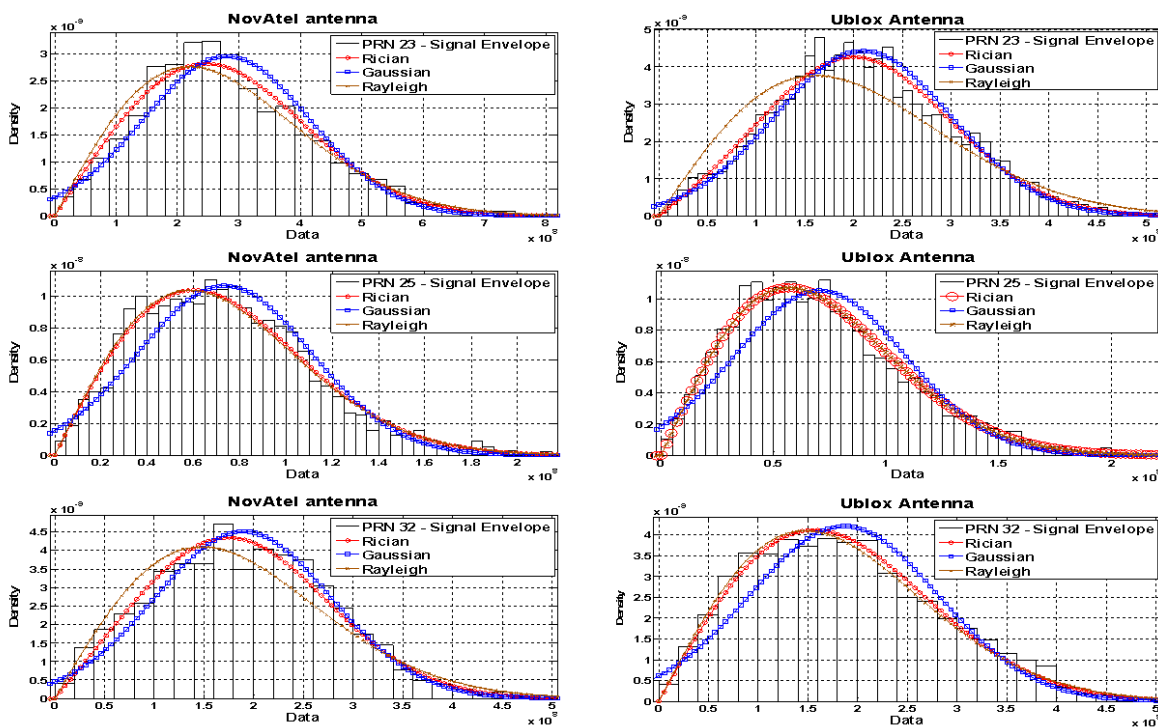
**Figure 5-26: Rician, Normal and Rayleigh fits to signal envelope of select PRNs - Wooden House**
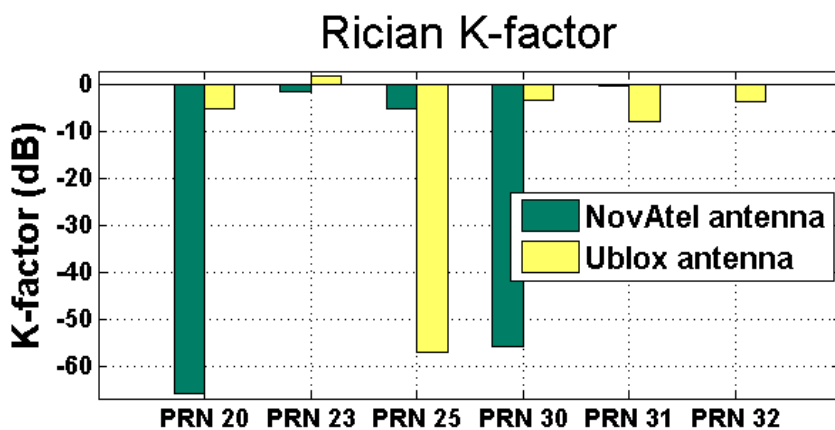


**Figure 5-27: Rician K-factor – Wooden House data**

### 5.3.2 Correlation Coefficient and Signal Level variations

The correlation coefficient of the signal captured by the NovAtel antenna for all PRNs is shown in Figure 5-28. The correlation coefficient at each point is based on 40 samples.
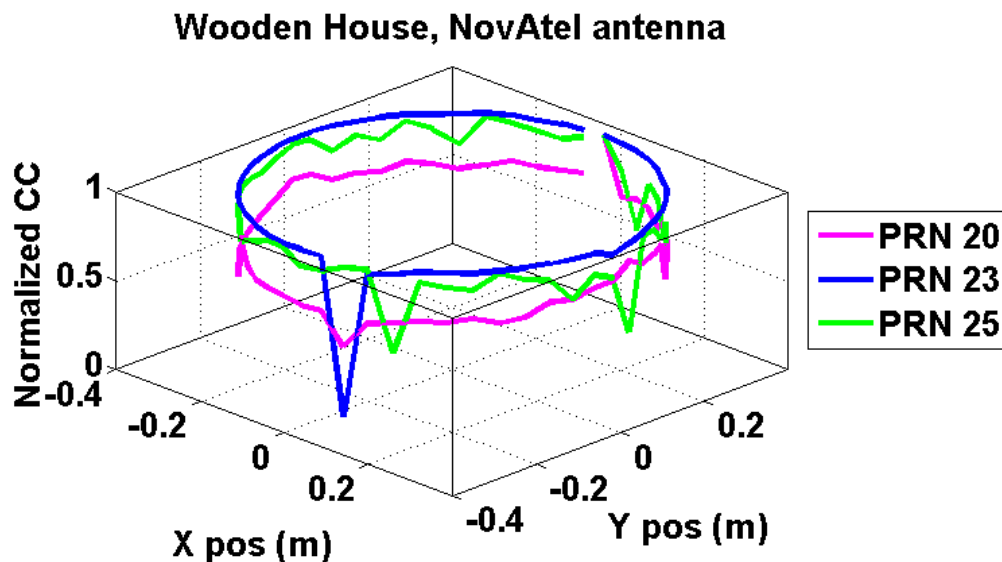


**Figure 5-28: Signal's correlation coefficient – Wooden House**

Also, consideration of the signal level changes in terms of carrier to noise ratio is of interest. This will provide an understanding of how the signal level varies in a certain environment for different signals that have traveled through different paths to reach the array and will also provide a tool with which to study the GNSS channel time dependence. In Figure 5-26 the $C/N_0$ variations for PRNs 23, 25 and 32 are shown. The signal of PRN 25 has a considerably low mean $C/N_0$ of about 20 dB-Hz. This low signal level falls in deep fading very regularly. On the other hand, for the cases of PRNs 23 and 32, the signals have an acceptable mean $C/N_0$ s (shown in Figure 5-24) and are trapped in deep fading less frequently.
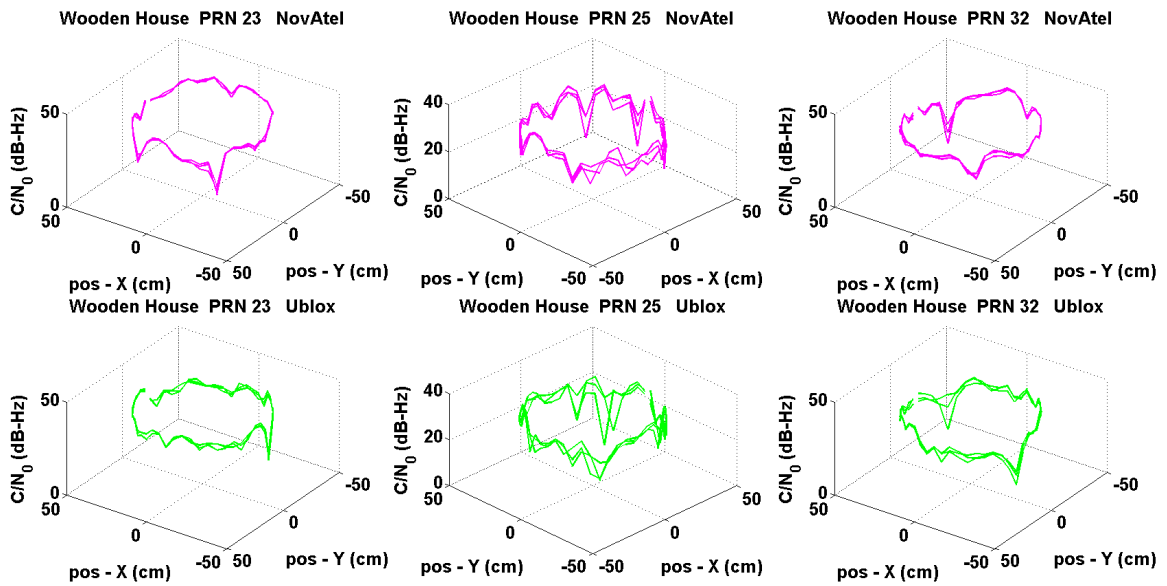
**Figure 5-29:** $C/N_0$ **variations – Wooden House Data**

It can be seen that for all of these samples the signal level variations maintain the same pattern and this can be a sign of the GNSS channel temporal stability. The duration of this sample is three revolutions, each 10 s long, and it must be noted that the surrounding environment did not changed through data collection.

### 5.3.3 AoA, AS and AG characterization

The measured AS plots of selected PRNs for both data sets are shown in Figure 5-30. In this figure solid and dashed blue lines represent AoA distribution and real AoA of the satellites respeas measured by the NovAtel antenna. The purple solid and dashed lines represent the same information measured by the Ublox antenna. As can be observed, in the case of high elevation signals, the Ublox antenna detects the AoA as accurately as the NovAtel. Also, for low to mid elevation satellites, the Ublox antenna detects the AoA relatively more accurately than the NovAtel antenna. Moreover, in some cases both antennas fail to detect the correct angle of arrival. The interesting point, as shown in Figure 5-30, is that the NovAtel antenna amplifies the incoming interference

signals from higher elevation angles and this issue may corrupt the accuracy of AoA estimation.

The achieved array gain is plotted in Figure 5-31, where it is shown that PRN 23 has led to the highest array gain and a maximum array gain degradation of around 1 dB. On the other hand, for the case of PRN 25, the maximum achieved array gain is less than 15 dB. The different signal qualities of PRN 23 and PRN 25 can be compared using Figure 5-30 and Figure 5-29, where signal AoA distribution and level variations are shown. As can be seen in Figure 5-29, PRN 25 falls in deep fading more frequently than PRN 23. Also, the AoA distribution for PRN 23 is more concentrated about the true LoS of the satellite than PRN 25, where its AoA distribution has many peaks that are not necessarily aligned with the LoS direction.

### 5.3.4 Conclusions

This data collection scenario was intended to characterize the GNSS channel in typical North American residential structures and also to assess the effect of the antenna gain pattern on the AoA estimation accuracy and AoA distribution.

For instance, in the case of PRN 25, it was shown that severe changes in the signal level and the intensity of the multipath interference reduce the array gain and cause rapid signal decorrelation. On the other hand, the signal of PRN 23 resulted in a higher array gain, which has a higher K-factor due to less signal interruption by multipath components. Moreover, the results show that in this case, the Ublox antenna results in somehow more accurate AoA estimation. In this case it was seen that the wireless channel is more stable temporally as compared to the case of PRN 28 in the previous dataset.
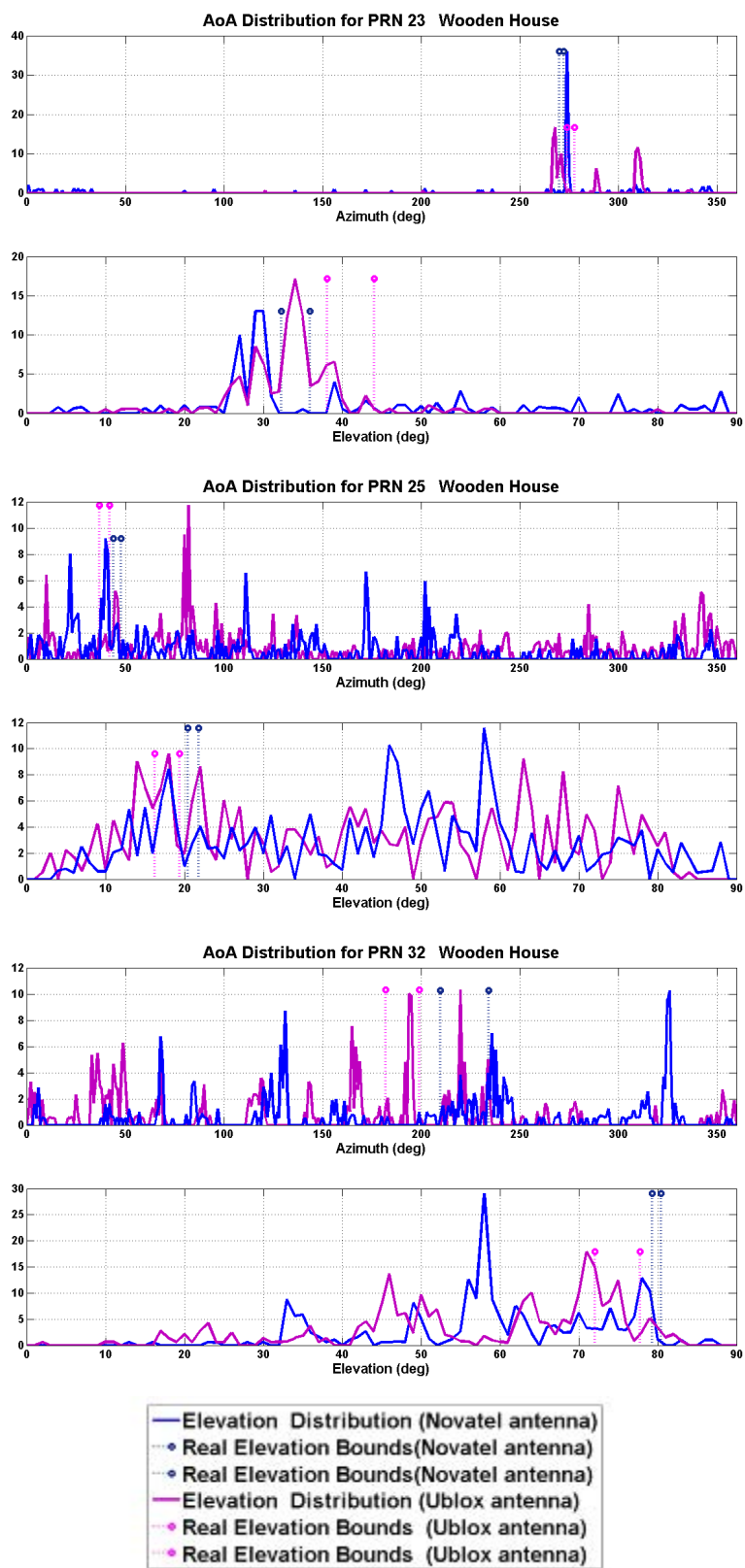
Figure 5-30: Measured AS - Wooden house
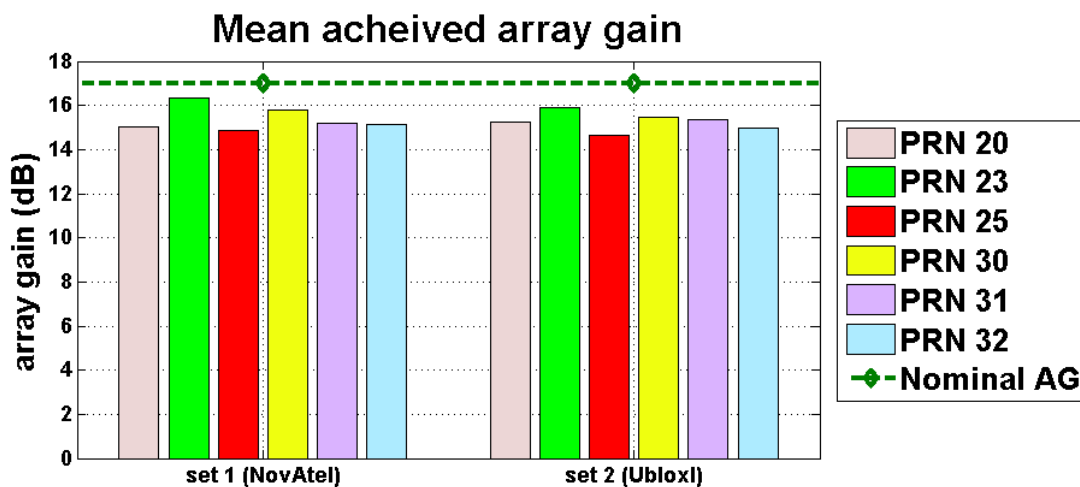
**Figure 5-31: Achieved array gain – Wooden house**

## 5.4 Dense indoor multipath environment, effect of antenna gain pattern

The main goal of this section is to provide further insight into the effect of the antenna gain pattern on AoA distribution. Two sets of data were collected in the NavLab using the same two antenna elements used in previous cases (NovAtel GPS 701/702 GGL and Ublox M-335). A brief review of the data collection scenario is presented in Figure 5-32.

Figure 5-33 shows the Rician K-factor for the two data sets. Also, Figure 5-34 shows the AoA distribution of the signal for selected PRNs. This distribution is based on 40 samples per each data set. As can be concluded by visual comparison of the results of each PRN, in this situation, for low to mid elevation angles, the Ublox antenna estimates the AoA distribution somewhat more accurately than the NovAtel antenna. This can especially be seen in the case of PRN 16 where both signals have almost acceptable K-

factors. In this case, it is evident that the NovAtel antenna amplifies the higher elevation multipath components.



**NavLab sky plot and Technical specification**
Data collected at 12 Apr. 2011, 5 pm ~ 6 pm

| Designation: N1 |
| Number of data sets: 2 |
| UCA rotation speed ($\omega$): 6 rpm |
| Coherent integration time ($T_{coh}$): 200 ms |
| Number of array elements: 50 |
| Expected array gain: 17 dB |
| UCA radius: 36 cm |
| Half Power Beamwidth: 17 deg |
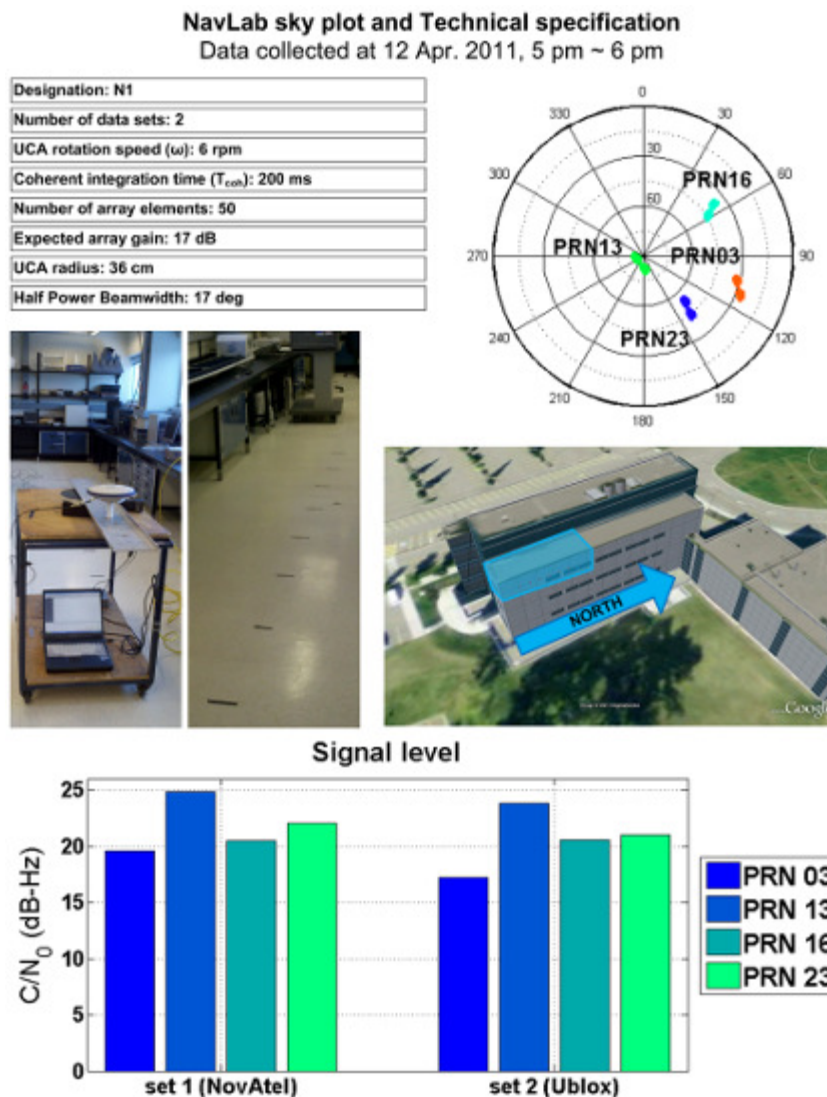
**Figure 5-32**: **Skyplot, signal level and technical specification of the data collection scenario – NavLab**

Also, it can be seen that both antennas perform satisfactorily while dealing with higher elevation signals of PRN 13. However, it must be noted that the Ublox antenna has amplified the incoming multipath interference from lower elevation angles.
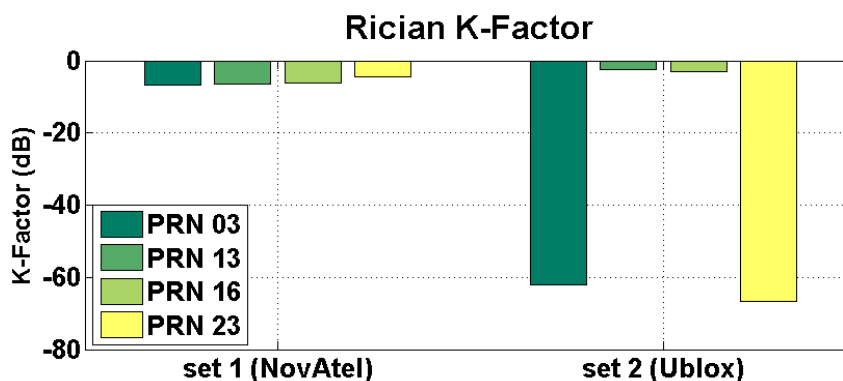
**Figure 5-33: Measured Rician K-factor – NavLab**

## 5.5 Dense multipath environment, Effect of satellite azimuth and elevation

The main motivation for this data collection was, first, to measure the signal parameters inside of a more reinforced commercial type structure in more depth and, second, to assess the effect of the satellite-receiver geometry in dense multipath fading environments. In the previous dataset, it was observed that the signals coming from the ceiling of NavLab have significantly narrower AoA distribution (Lower angular spreads).

The data collection equipment was set up inside of the NavLab located on the third floor of the CCIT building on the U of C campus. The eight sets of data were collected from 10:00 am until 15:30 pm. The data collection location, skyplot and other relevant technical data are shown in Figure 5-31. Each data set contains 40 to 90 samples. As shown in Figure 5-35, the rotating table was mounted on a moving cart to gather samples over a vast region of the NavLab as marked by the points shown in the figure. The distance between marks was 60 cm to ensure that the gathered samples were independent from each other.
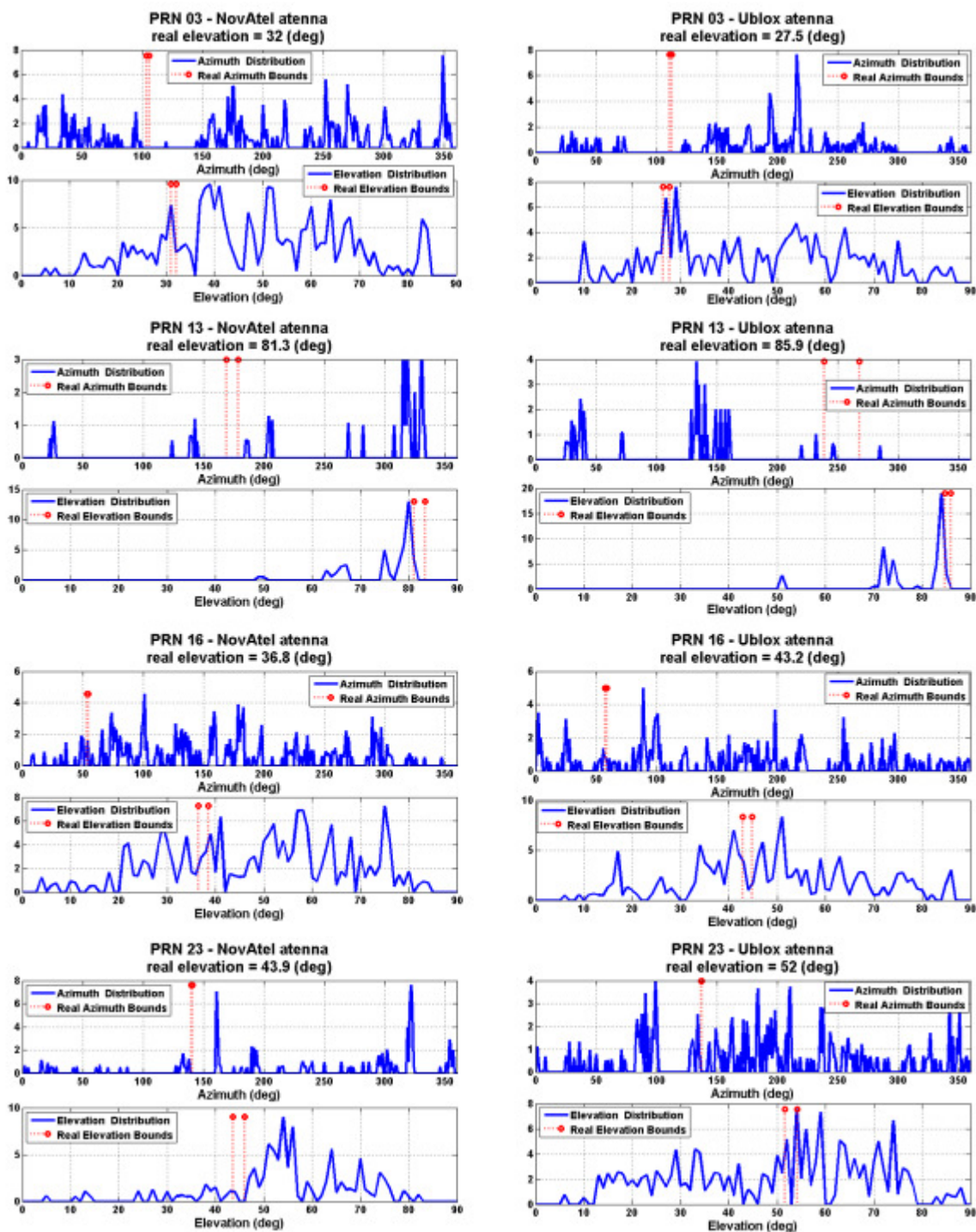
**Figure 5-34: Measured AS in the NavLab with different antennas**

During this data collection, three satellites were present at all data sets; namely PRN 15, PRN 18 and PRN 21. The NavLab walls include windows, concrete and metallic panels on the east and south sides. . The ceiling is the roof of the building and consists of reinforced concrete. Therefore, it is expected that the GNSS signals entering the NavLab face severe blockage and undergo fading. However, it was seen that the NavLab ceiling appears to attenuate signals less than the walls, which is somewhat surprising, given that windows on the eastern wall are expected to permit GNSS signals to penetrate more easily due to lower attenuation.

As can be seen in the skyplot, the path of the selected satellites over this location cover a considerable portion of field of view from high to low elevation angles, from the west side of the building to the east side, and a complete curve from low elevations to the southeast, to mid elevations to the east, and then low elevations to the northeast. This allows full characterization of the effects of the ceiling, walls and windows on GNSS signals.

The radius of the UCA is 36 cm, it is rotated with a speed of 6 rpm and the data is processed with 200 ms of coherent integration time. This results in 50 synthetic antenna elements.

### 5.5.1 Fading Channel Model

Figure 5-36 shows the normalized signal envelope of all PRNs through all eight data sets and the Rician K-factor is shown in Figure 5-37. As can be seen in these plots, for the case of PRN 21, when the satellite is in the North West, the signal is in deep fading. As the satellite appears over the data collection location, the signal K-factor increases, indicating that particular LoS component of the signal is getting stronger than

the interfering multipath signals and is dominating the channel. At the end, the signal goes into fading as the satellite falls. The same is true for PRN 18. However, in the case of PRN 15, as can be seen by comparing the K-factor plot with the skyplots, as long as the satellite is in mid elevation angles to the east and the signal is available from the windows, the K-factor is much higher than that of the other data sets.
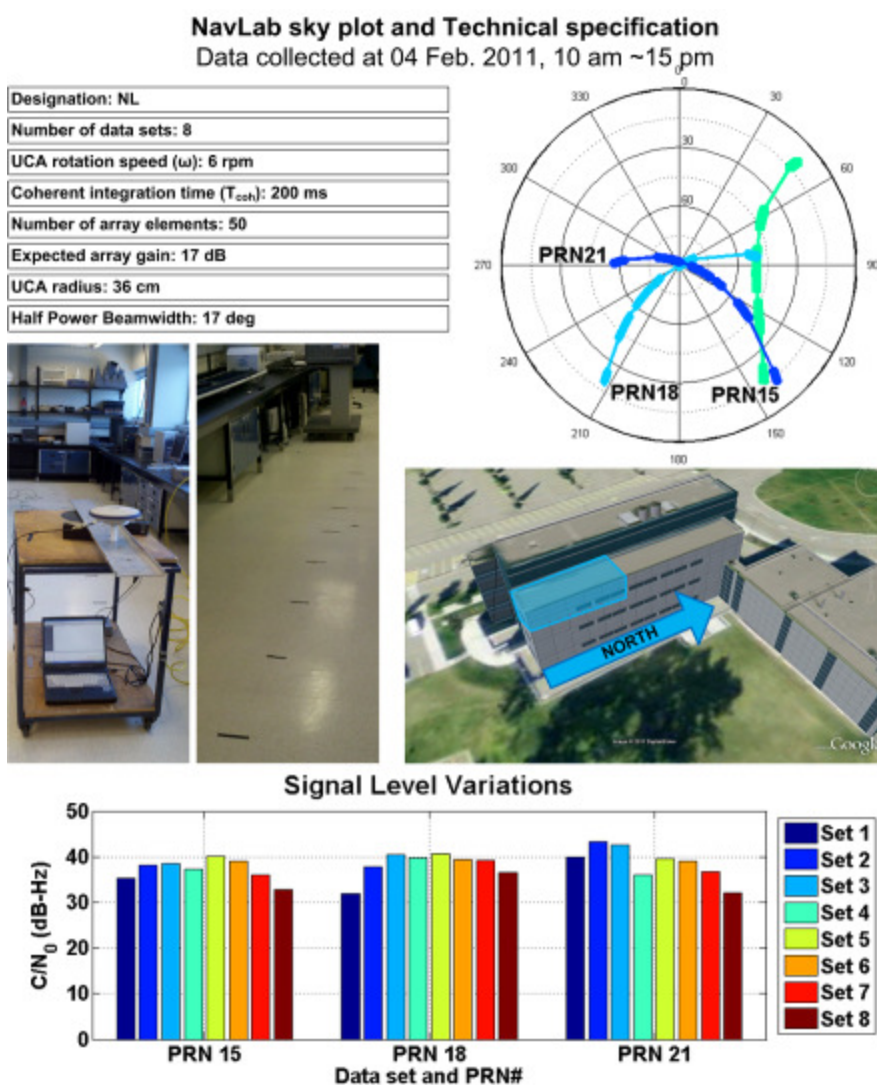


**Figure 5-35: Data collection specification – NavLab**
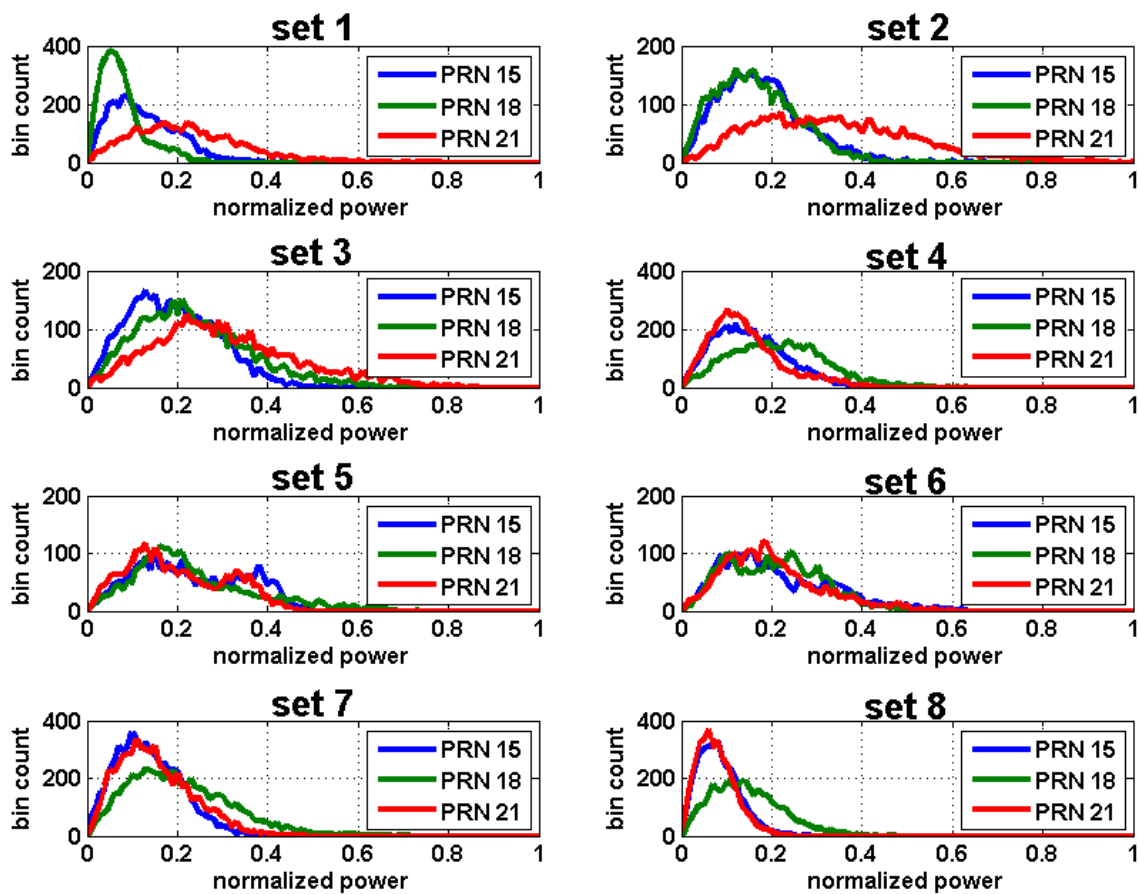
**Figure 5-36: Normalized signal power distribution – NavLab**
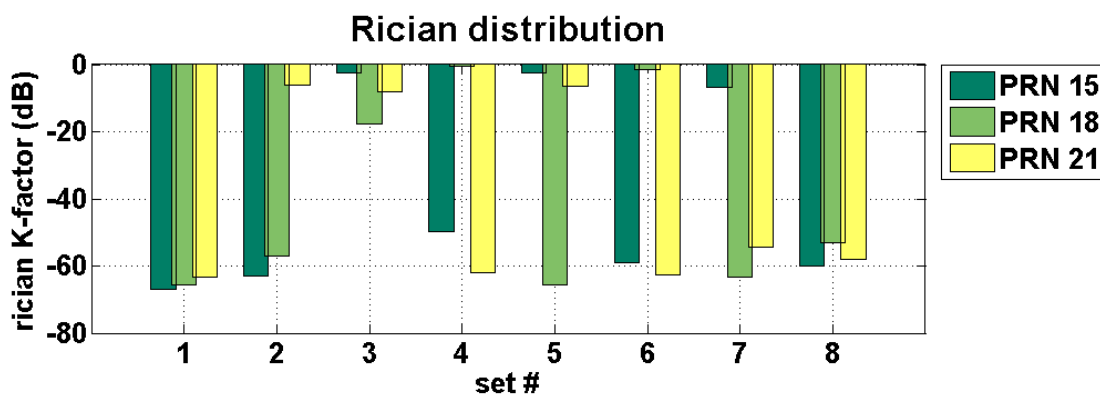


**Figure 5-37: Rician K-factor – NavLab**

### *5.5.2 Correlation Coefficient and Signal Level*

The plots of correlation coefficient are shown in Figure 5-38 for selected sets of PRNs. It must be noted that each data set contains more than 40 samples. Figure 5-39 shows signal level variations in terms of $C / N_0$ for selected sets of three, four and five. The complete sets of $C / N_0$ plots of all data sets are shown in Appendix B. As can be seen for the case of PRN 21, the signal levels for data sets two, three and five are higher. Furthermore, for the case of PRN 15, the signal level is steadier in data sets three, five and six. The desired signal level characteristics for PRN 18 occur at data sets three, four and six. These data sets match accurately with those with higher Rician K-factors.

Another interesting issue is that by comparing the plots in Figure 5-39, the locations at which signals are stronger or are blocked can be identified and show the effect of shadowing. For instance, for the 4th set of data, all PRNs have a lower carrier to noise ratio on the right half of the circle.

Moreover, as stated before, these plots can be used to assess the temporal changes of the wireless channel. As can be seen, while in many cases the channel remains constant for a long time (three complete revolutions), in some cases the channel seems to be time variant from sample to sample. Unlike the case of PRN 28 outside the ICT building, where the channel was changing over only short sections of the UCA trajectory due to the changes in the environment, in the present case the changes are due to very low SNR values.
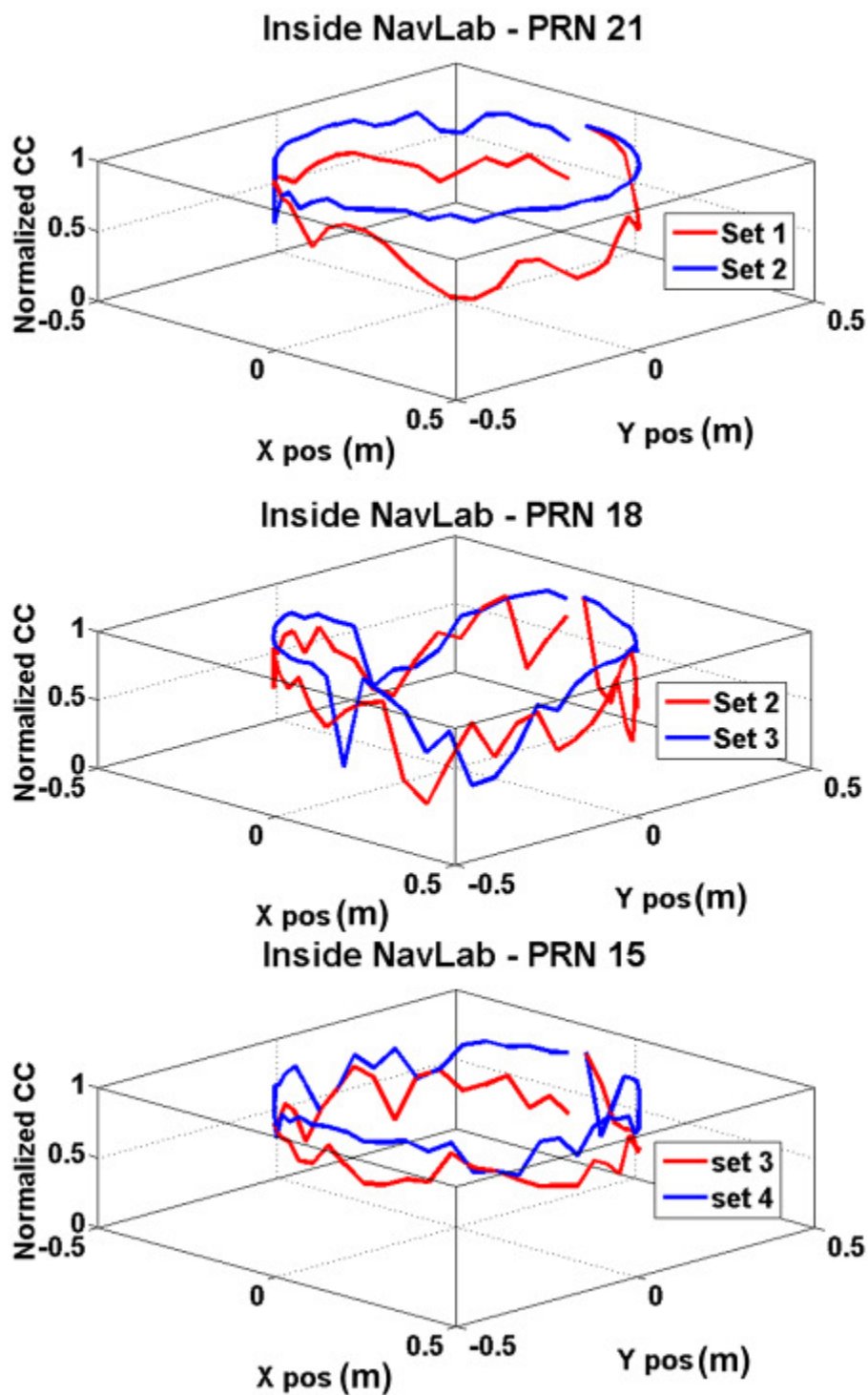
**Figure 5-38: Normalized correlation coefficient – NavLab**
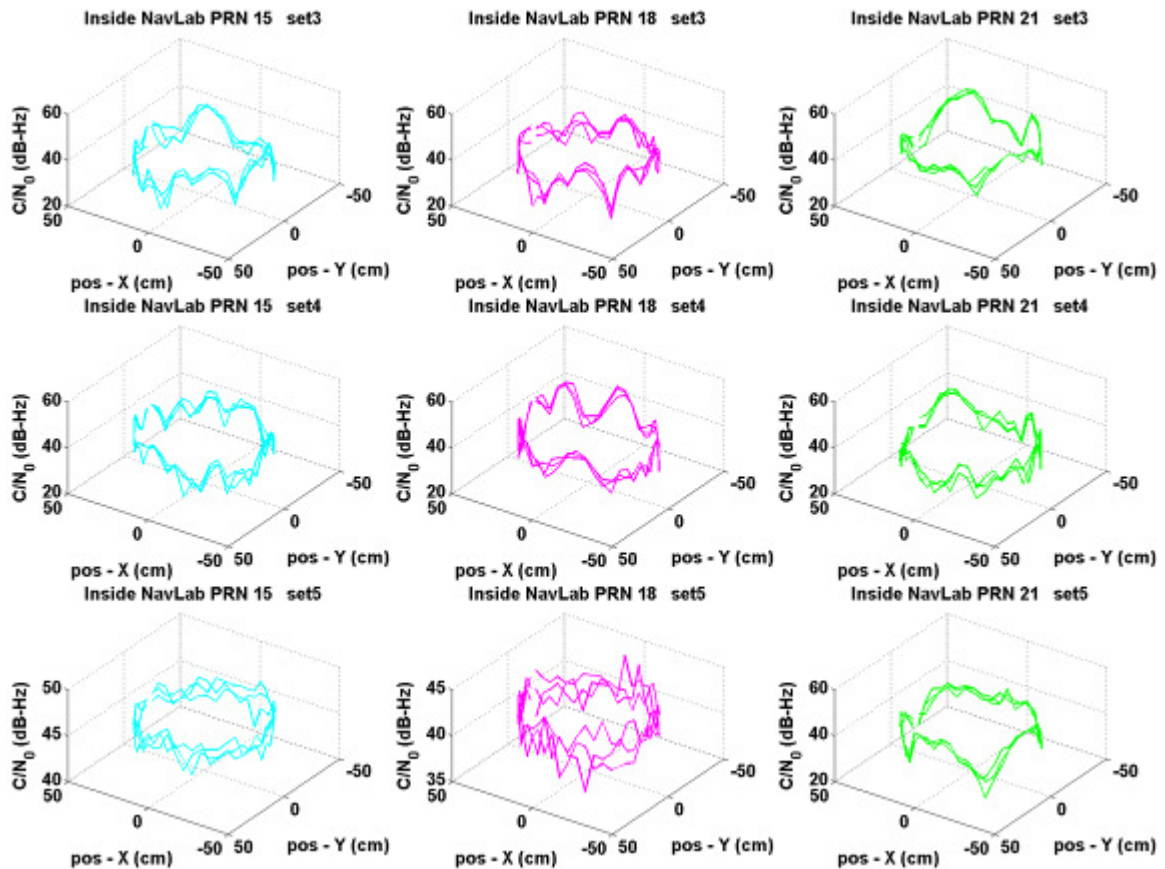
**Figure 5-39: Signal level variations for each PRN and dataset – NavLab**

### 5.5.3 AoA, AS and AG Characterization

One of the main goals of this thesis is to characterize the AoA distribution of the incoming signals, along with assessing the performance of beamforming in multipath environments. As was observed in the results of the previous scenario, the satellites at higher elevation angles provide higher SNR signals with less angular spread. This is shown in Figure 5-40, where the AS of different data sets for PRN 21 is shown. As can be seen, when the satellite have higher elevation angles, the AS decreases and the AoA distribution becomes sharper. The same is true for PRN 18 and somewhat for PRN 15. However it must be noted that both PRN 21 at set four and PRN 18 at set five experience severe signal blockage that can be due to some obstacle in the ceiling of the CCIT

building. This can also be verified by comparing the AoA distribution, AG and K factor plots.
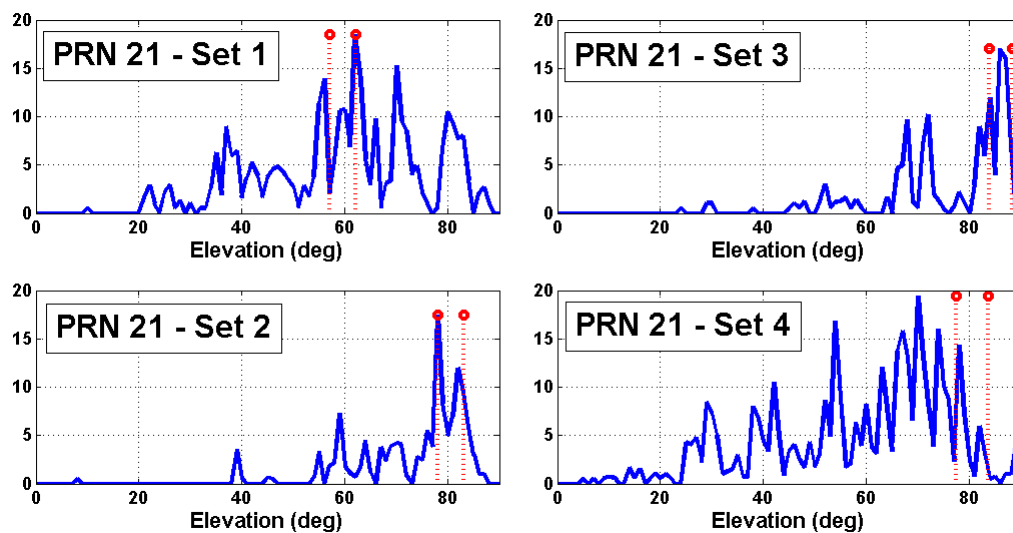


**Figure 5-40: AoA distribution temporal changes, PRN 21 – NavLab**

In the following, the measurements of AG and AoA along the azimuth and elevation are presented in Figure 5-41, Figure 5-42 and Figure 5-43. In these figures, the first plot compares the achieved AG with a nominal array gain of 17 dB. The second and third plots show the true AoA and also the estimated mean AoA values and their $1\sigma$ accuracy boundary as a function of the elevation and azimuth respectively. As can be seen in the first row plots, showing achieved array gain, higher array gains are achieved when the K-factor and/or $C/N_0$ s are high.
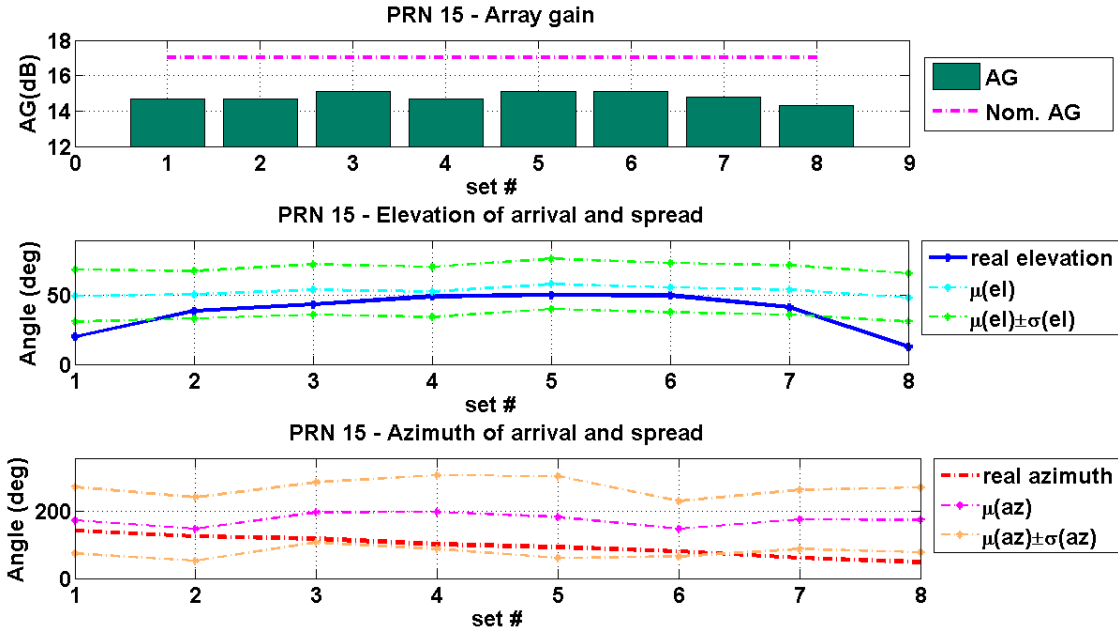
**Figure 5-41: Array gain and angular spread, PRN 15, NavLab, all data sets**

In other words, AG follows the trend for the $C/N_0$ and K-factor. It also should be noted that the array gain in here is measured via the definition in Equation (5-3) that is not accurate in the case of Rayleigh fading. It is adopted to comply with the AG results in outdoor conditions. A part of the achieved array gain in this scenario emerges from diversity gain as explained in more detail by Broumandan et al (2011). Also, looking at the second row of plots shows that the AoA estimation accuracy along elevation is highest when the satellite is located at higher elevation angles.
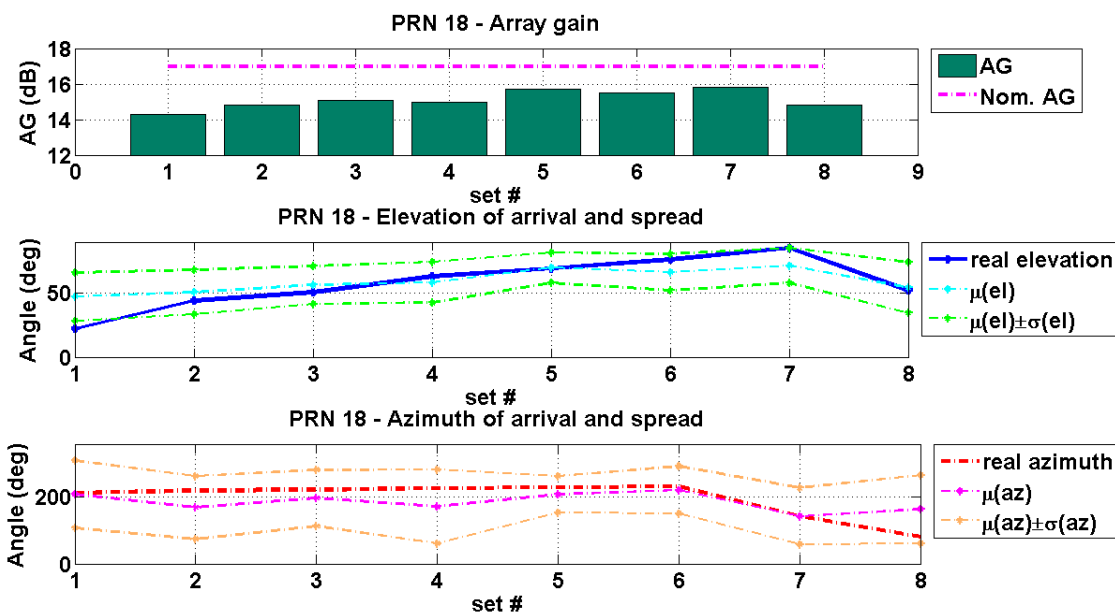
**Figure 5-42: Array gain and angular spread, PRN 18, NavLab, all data sets**
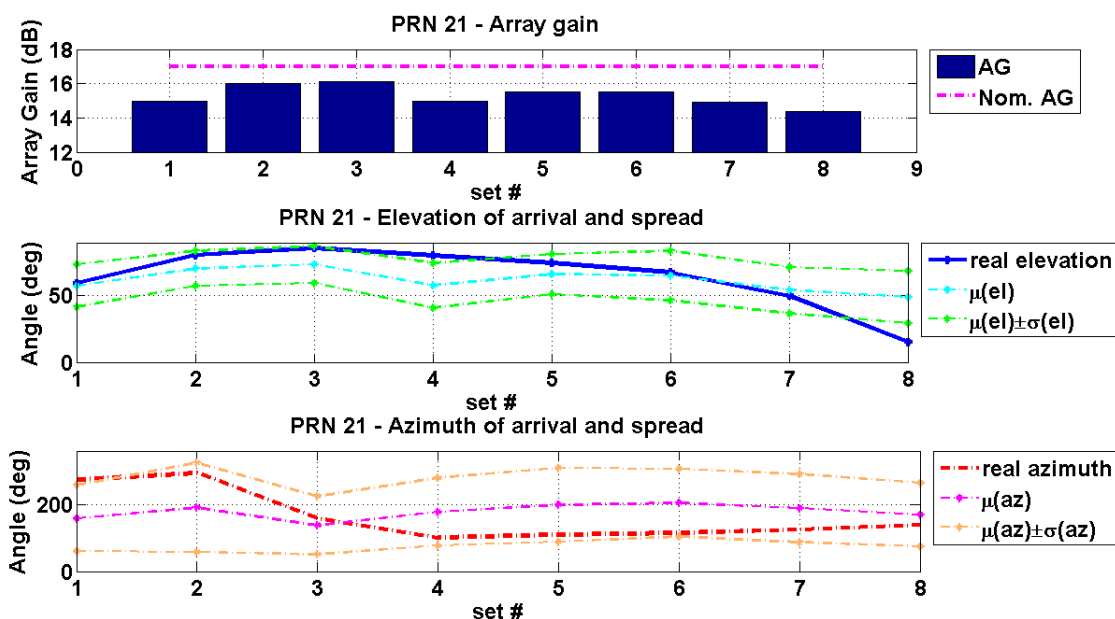


**Figure 5-43: Array gain and angular spread, PRN 21, NavLab, all data sets**

However, it seems that the signal is concentrated along mid-elevation angles. On the other hand, for the case of the azimuth angle, the difference between mean estimated

AoA and real azimuth is higher and the signal is spread over a wider range of azimuths of arrivals.

## 5.6 Comparison of the overall results

In this chapter, in-depth analyses were performed on several sets of data that were collected in a wide range of environments to characterize the GNSS multipath channel. Several parameters of the channel, including the governing fading model, Rician K-factor, correlation coefficient, signal level variations, AoA distribution and AS and array gain were studied. It must be noted that through the following analysis, the standard deviation of the AoA distribution was adopted as a measure of angular spread.

In the first set of data that was collected in a low multipath situation, it was observed that the channel can be modeled mainly by a Rician distribution, the array gain is almost equal to the expected nominal value, signals are highly correlated and the signal level is generically high and stable. The AoA estimation is highly accurate and the AS is less than $1^{o}$ for most of the cases. As mentioned before, the importance of AS is due to its effect on the Doppler spread of the signal. These values are quantified in Table 5-1. In this table, $E\{.\}$ is the mean and $\sigma\{.\}$ is the standard deviation of the measured values.

The second set of data was collected in a low to mid multipath situation, similar to an urban canyon, surrounded by several buildings. It was observed that the channel corresponding to high elevation GNSS satellites, which are largely free from multipath fading, can be modeled mainly by a Rician distribution. For these cases, the array gain is almost equal to the expected nominal value, signals are highly correlated and the signal level is fundamentally high and stable.

**Table 5-1: Quantified measurement results, CCIT rooftop**

| PRN | $\tilde{\theta}_{\text{Real}}$ | $\phi_{\text{Real}}$ | $E\{\tilde{\theta}_{\text{Measure}}\}$ | $\sigma\{\tilde{\theta}_{\text{Measure}}\}$ | $E\{\phi_{\text{Measure}}\}$ | $\sigma\{\phi_{\text{Measure}}\}$ | $AG$ | $\dfrac{C}{N_0}$ | $K$ factor |
|-----|------|------|------|-----|-------|-----|------|------|------|
| 2   | 40 | 69  | 41   | 0.2 | 74.9  | 0.5 | 26.9 | 47.1 | 16.8 |
| 5   | 57 | 119 | 59   | 0.1 | 117.4 | 1.3 | 26.9 | 48.8 | 17.3 |
| 10  | 52 | 84  | 53.2 | 0.1 | 84.6  | 1.1 | 26.9 | 48.3 | 18.2 |
| 12  | 25 | 181 | 27   | 0.4 | 181.3 | 0.7 | 26.9 | 43.9 | 18.9 |
| 21  | 15 | 247 | 18.9 | 0.5 | 246   | 0.6 | 26.9 | 40.3 | 16.3 |
| 24  | 54 | 244 | 55.7 | 0.3 | 243.9 | 0.5 | 26.9 | 49.4 | 19.3 |
| 29  | 69 | 294 | 70.4 | 0.4 | 294.8 | 0.7 | 26.9 | 49.7 | 18.4 |
| 30  | 43 | 210 | 44.3 | 0.2 | 209.9 | 1   | 26.9 | 47.5 | 23.1 |
| 31  | 12 | 288 | 16.5 | 0.3 | 289.1 | 1.1 | 26.9 | 39   | 14.7 |

The AoA estimation is accurate and the AS (along elevation) is within a few degrees for most cases. However, it was observed that for satellites (namely PRN 28 in this case) that are blocked by surrounding obstructions, the AG, the received phase, Rician K-factor and other parameters are impacted severely. The corresponding values are listed in Table 5-2.

A third set of data was collected in a wooden house, utilizing two antenna elements to observe the effect on AoA estimation accuracy. Firstly, it was seen that in this situation the $C/N_0$ is typically low, the Rician K-factor is typically negative, indicating that the dominating channel is Rayleigh instead of Rician and up to 3 dB of array gain degradation was observed.

The AS (along elevation) in this situation is between $10^{\text{o}}$ and $25^{\text{o}}$. Moreover, although the signal level is typically low and its plots show partial shadowing, its behaviour is steady and indicates that the channel does not change much through the measurement time.

**Table 5-2: Quantified measurement results, outside the ICT building**

| PRN | $\tilde{\theta}_{\text{Real}}$ | $\phi_{\text{Real}}$ | $E\{\tilde{\theta}_{\text{Measure}}\}$ | $\sigma\{\tilde{\theta}_{\text{Measure}}\}$ | $E\{\phi_{\text{Measure}}\}$ | $\sigma\{\phi_{\text{Measure}}\}$ | $AG$ | $\dfrac{C}{N_0}$ | $K$ factor |
|---|---|---|---|---|---|---|---|---|---|
| 9 | 32 | 309 | 35.3 | 16.8 | 278.3 | 44.6 | 26.91 | 45.8 | 14 |
| 11 | 28 | 56 | 7.9 | 12.2 | 57.5 | 5.9 | 26.8 | 41.7 | 7.4 |
| 17 | 81 | 142 | 81.2 | 5.2 | 150.8 | 22.6 | 26.94 | 51 | 24.3 |
| 28 | 51 | 91 | 46.7 | 7.5 | 172.2 | 95.6 | 26.3 | 39.3 | -1.9 |

It was also seen that under such multipath conditions, both antennas result in a somehow equal accuracy of AoA estimation. However, the resulting AoA distributions of the two antennas differ slightly. Table 5-3 lists the parameters studied for this situation. To gain more understating of the effect of antenna pattern on AoA estimation and distribution, another set of data was collected in the University of Calgary's NavLab, utilizing the same two antenna elements. Firstly, it was seen that in this situation the $C/N_0$ and the Rician K-factor are typically lower than the previous cases and the AG degradation reaches up to 3 dB. Also, the AS (along elevation for both antennas) varies from $10^\text{o}$ to $20^\text{o}$. The results show that under harsher multipath conditions, the AoA estimation accuracy of the NovAtel antenna is better than the other antenna. This can be linked to the fact that in the NavLab, based on its structure, the signal attenuation from ceiling is typically less than the attenuation from the walls. Table 5-4 lists the parameters studied for this situation.

Finally, the fifth set of data was again collected in the NavLab. The main goal was to assess the effect of satellite-receiver geometry and 8 sets of data were collected over a 7-hour period. The results showed that the $C/N_0$ is typically low, the Rician K-factor is typically negative, indicating that the dominating channel is Rayleigh instead of

Rician and, also, up to 4 dB of array gain degradation was observed for very weak signals. The AS (along elevation) in this situation is between $15^o$ and $20^o$. Moreover, the signal level plots for most of the cases show wide shadowing and in some extreme cases, the high level of the noise causes temporal variation in the signal level from one sample of the signal to the next. Table 5-5 lists the parameters studied for this situation.

**Table 5-3: Quantified measurement results, wooden house**

| PRN | | $\tilde{\theta}_{\text{Real}}$ | $\phi_{\text{Real}}$ | $E\{\tilde{\theta}_{\text{Measure}}\}$ | $\sigma\{\tilde{\theta}_{\text{Measure}}\}$ | $E\{\phi_{\text{Measure}}\}$ | $\sigma\{\phi_{\text{Measure}}\}$ | $AG$ | $\dfrac{C}{N_0}$ | $K$ factor |
|---|---|---|---|---|---|---|---|---|---|---|
| 20 | **Ublox** | 55 | 290 | 55 | 16.3 | 192.3 | 105.7 | 15.4 | 34.9 | -66.2 |
| | **NovAtel** | 60 | 283 | 53.9 | 18 | 139 | 95.9 | 14.9 | 34.9 | -5.2 |
| 23 | **Ublox** | 32 | 270 | 42.2 | 20 | 243.9 | 94 | 16.2 | 39.4 | -1.5 |
| | **NovAtel** | 38 | 274 | 36.5 | 9.6 | 284.8 | 29.1 | 16.1 | 37.9 | 1.8 |
| 25 | **Ublox** | 21 | 47 | 42.2 | 24.5 | 125.8 | 94.5 | 14.7 | 27.6 | -5.1 |
| | **NovAtel** | 19 | 42 | 40.8 | 24.4 | 173.1 | 113.5 | 14.1 | 27.9 | -57.3 |
| 30 | **Ublox** | 18 | 143 | 39.6 | 25.3 | 136.1 | 57.1 | 15.9 | 30.7 | -56.4 |
| | **NovAtel** | 24 | 139 | 35.2 | 16.7 | 134 | 33.6 | 15.7 | 35 | -3.3 |
| 31 | **Ublox** | 66 | 81 | 61.7 | 14.2 | 168.3 | 88.3 | 15.4 | 37.9 | -0.2 |
| | **NovAtel** | 62 | 70 | 62.8 | 12.7 | 172.5 | 116.9 | 14.7 | 35.4 | -7.8 |
| 32 | **Ublox** | 80 | 234 | 63.2 | 12.5 | 192.5 | 101.6 | 15.3 | 35.8 | 0.2 |
| | **NovAtel** | 77 | 199 | 59.9 | 15.9 | 142.6 | 86.6 | 14.9 | 36.2 | -3.5 |

Another interesting issue to point out is that for most of the harsh multipath cases, the AS along the azimuth is so large that in some cases it covers up to $270^o$ of the azimuth field of view, whereas for elevation, the maximum AS is about $25^o$. This is in agreement with Parsons (2000) and Bluantstein & Andersen (2002), both of whom state that for communication channels the AoA distribution in azimuth can be assumed to be a uniform distribution from $0$ to $2\pi$.

**Table 5-4: Quantified measurement results, NavLab set#1**

| PRN 03 | | | | | | | | | |
|---|---|---|---|---|---|---|---|---|---|
| | $\tilde{\theta}_{\text{Real}}$ | $\phi_{\text{Real}}$ | $E\{\tilde{\theta}_{\text{Measure}}\}$ | $\sigma\{\tilde{\theta}_{\text{Measure}}\}$ | $E\{\phi_{\text{Measure}}\}$ | $\sigma\{\phi_{\text{Measure}}\}$ | $AG$ | $\dfrac{C}{N_0}$ | $K\ factor$ |
| **NovAtel** | 31.5 | 104.6 | 48.2 | 17.4 | 193.3 | 103.9 | 14.4 | 19.5 | -6.7 |
| **Ublox** | 27.1 | 111.9 | 47.9 | 18.8 | 189.9 | 76.3 | 14.7 | 17.2 | -62.1 |

| PRN 13 | | | | | | | | | |
|---|---|---|---|---|---|---|---|---|---|
| | $\tilde{\theta}_{\text{Real}}$ | $\phi_{\text{Real}}$ | $E\{\tilde{\theta}_{\text{Measure}}\}$ | $\sigma\{\tilde{\theta}_{\text{Measure}}\}$ | $E\{\phi_{\text{Measure}}\}$ | $\sigma\{\phi_{\text{Measure}}\}$ | $AG$ | $\dfrac{C}{N_0}$ | $K\ factor$ |
| **NovAtel** | 82.1 | 169.7 | 74.4 | 8.1 | 242.4 | 100.9 | 16 | 24.8 | -6.5 |
| **Ublox** | 85.4 | 253.5 | 76.9 | 9.6 | 111.7 | 68.4 | 15.8 | 23.8 | -2.3 |

| PRN 16 | | | | | | | | | |
|---|---|---|---|---|---|---|---|---|---|
| | $\tilde{\theta}_{\text{Real}}$ | $\phi_{\text{Real}}$ | $E\{\tilde{\theta}_{\text{Measure}}\}$ | $\sigma\{\tilde{\theta}_{\text{Measure}}\}$ | $E\{\phi_{\text{Measure}}\}$ | $\sigma\{\phi_{\text{Measure}}\}$ | $AG$ | $\dfrac{C}{N_0}$ | $K\ factor$ |
| **NovAtel** | 37.5 | 53.9 | 49.1 | 18.1 | 168.6 | 82.1 | 14.6 | 20.5 | -6.2 |
| **Ublox** | 43.9 | 58.2 | 49.4 | 17.9 | 163.5 | 100.6 | 14.6 | 20.5 | -3 |

| PRN 23 | | | | | | | | | |
|---|---|---|---|---|---|---|---|---|---|
| | $\tilde{\theta}_{\text{Real}}$ | $\phi_{\text{Real}}$ | $E\{\tilde{\theta}_{\text{Measure}}\}$ | $\sigma\{\tilde{\theta}_{\text{Measure}}\}$ | $E\{\phi_{\text{Measure}}\}$ | $\sigma\{\phi_{\text{Measure}}\}$ | $AG$ | $\dfrac{C}{N_0}$ | $K\ factor$ |
| **NovAtel** | 44.8 | 140.5 | 54.3 | 15 | 226.1 | 99.1 | 15 | 22 | -4.4 |
| **Ublox** | 52.9 | 137.5 | 49.1 | 19.7 | 193.1 | 89.6 | 14.6 | 21 | -66.6 |

Nevertheless, it must be noted that wider distributions along the azimuth are some times associated with wider distributions along the elevation and the AS along elevation is considerably affected by the gain pattern of the antenna. Furthermore, this can be linked to AG degradation where, as expected for wider angular spread, this parameter reaches up to 4 dB. The values presented in Table 5-1 to Table 5-5 are visualized in Figure 5-44, Figure 5-45 and Figure 5-46. In Figure 5-44, the array gain degradation is linked to the AS. To plot these figures, the difference between the nominal AG and the achieved array gain for each scenario was taken as the AG degradation. The horizontal axis represents the AS. Since the AS along elevation and AS along azimuth are not necessarily proportional to each other, to quantify the AS for this plot, the square root of

AoA distribution along elevation times the square root of AoA distribution along azimuth, as

$$AS = \sqrt{\sigma(\tilde{\theta})\sigma(\phi)}\,.$$

<div align="right">(5-4)</div>

**Table 5-5: Quantified measurement results, NavLab set#2**

| | $\tilde{\theta}_{\text{Real}}$ | $\phi_{\text{Real}}$ | $E\{\tilde{\theta}_{\text{Measure}}\}$ | $\sigma\{\tilde{\theta}_{\text{Measure}}\}$ | $E\{\phi_{\text{Measure}}\}$ | $\sigma\{\phi_{\text{Measure}}\}$ | $AG$ | $\dfrac{C}{N_0}$ | $K$ factor |
|---|---|---|---|---|---|---|---|---|---|
| | | | | | **PRN 21** | | | | |
| set 1 | 57 | 271 | 57.6 | 16.1 | 158.9 | 98 | 13.9 | 35.4 | -63.5 |
| set 2 | 78 | 290 | 70.6 | 13.2 | 190.9 | 133.1 | 14.4 | 38.2 | -6.2 |
| set 3 | 83 | 302 | 73.5 | 14 | 137.7 | 86.9 | 14.7 | 38.6 | -8.1 |
| set 4 | 83 | 95 | 57.8 | 16.9 | 178.3 | 101.5 | 14.2 | 37.3 | -61.9 |
| set 5 | 76 | 107 | 66.3 | 15.1 | 199.2 | 110.1 | 14.6 | 40.3 | -6.4 |
| set 6 | 69 | 113 | 65.2 | 18.6 | 204.9 | 101.3 | 14.3 | 39 | -62.8 |
| set 7 | 54 | 122 | 54.2 | 17.5 | 189 | 101.9 | 14.6 | 36 | -54.4 |
| set 8 | 17 | 138 | 48.9 | 19.7 | 169.5 | 95.3 | 14.6 | 32.9 | -58 |
| | | | | | **PRN 18** | | | | |
| set 1 | 19 | 212 | 47.1 | 18.9 | 209.1 | 101.5 | 14.9 | 32 | -65.8 |
| set 2 | 41 | 219 | 50.8 | 17.4 | 169.1 | 95 | 15.1 | 37.8 | -57.2 |
| set 3 | 47 | 221 | 56.4 | 14.7 | 197.4 | 84.8 | 15.1 | 40.5 | -17.7 |
| set 4 | 60 | 226 | 58.5 | 15.9 | 172.2 | 111.6 | 15.1 | 39.8 | -0.5 |
| set 5 | 67 | 229 | 70 | 11.9 | 208.6 | 54.7 | 15.1 | 40.7 | -65.7 |
| set 6 | 74 | 232 | 66.3 | 14.3 | 222.1 | 71.3 | 15.1 | 39.5 | -1.7 |
| set 7 | 89 | 219 | 71.7 | 13.7 | 143 | 85.2 | 14.8 | 39.2 | -63.2 |
| set 8 | 54 | 81 | 54.3 | 19.9 | 164.2 | 102.6 | 14.3 | 36.5 | -53.1 |
| | | | | | **PRN 15** | | | | |
| set 1 | 17 | 143 | 49.7 | 18.9 | 174 | 99.5 | 14.8 | 40 | -67.1 |
| set 2 | 37 | 128 | 50.6 | 17.2 | 148.1 | 94.7 | 14.8 | 43.5 | -62.9 |
| set 3 | 41 | 122 | 54.1 | 18.3 | 197.5 | 90.3 | 15.4 | 42.8 | -2.6 |
| set 4 | 48 | 107 | 52.6 | 18.2 | 198.5 | 110.3 | 14.8 | 36.2 | -49.8 |
| set 5 | 50 | 95 | 58.2 | 18.2 | 183.3 | 122.3 | 15.4 | 39.6 | -2.5 |
| set 6 | 50 | 84 | 55.7 | 17.9 | 147.9 | 83.1 | 15.2 | 39 | -58.9 |
| set 7 | 44 | 64 | 54 | 17.9 | 176.3 | 88.7 | 15 | 36.8 | -6.9 |
| set 8 | 14 | 48 | 48.3 | 17.6 | 174.6 | 97.2 | 14.3 | 32.2 | -60.1 |
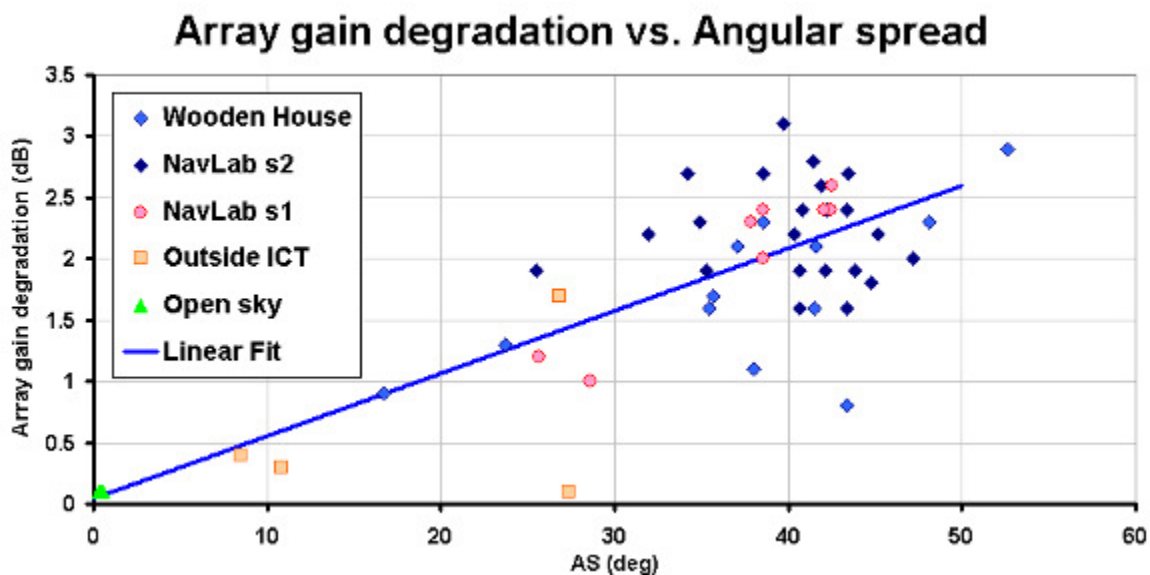
**Figure 5-44: Array gain degradation vs angular spread, all data sets**

As can be seen, the proposed trend perfectly follows the assumption that higher AS results in lower achieved array gain.

Figure 5-45 shows the trend between the array gain degradation and the measured Rician K-factor. It must be noted that to plot this figure, the data sets with extremely low K-factors (less than -45 dB) were ignored.

Again, as can be seen, as the K-factor (or the relative power of the LoS component to the interference level) decreases, the AS generally becomes wider and this leads to severe array gain degradation. It must be reminded that multipath and shadowing cause interfering components that corrupt the LoS signals and increases the AS and noise level (K-factor degradation), decrease the spatial correlation between signal samples and ultimately result in a loss of array gain.
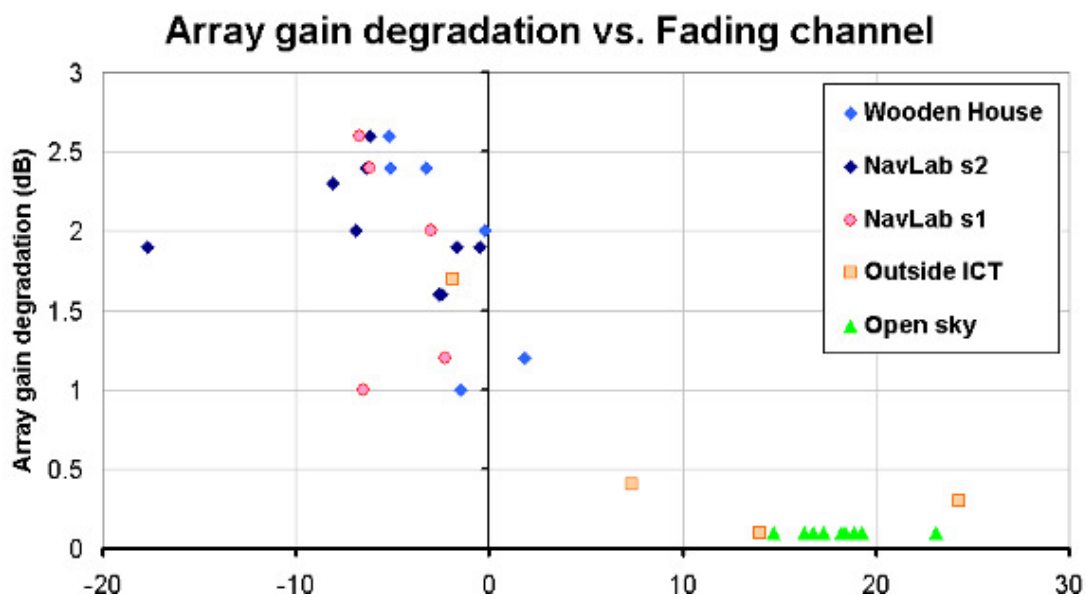
**Figure 5-45: Array gain degradation vs K-factor, All data sets**
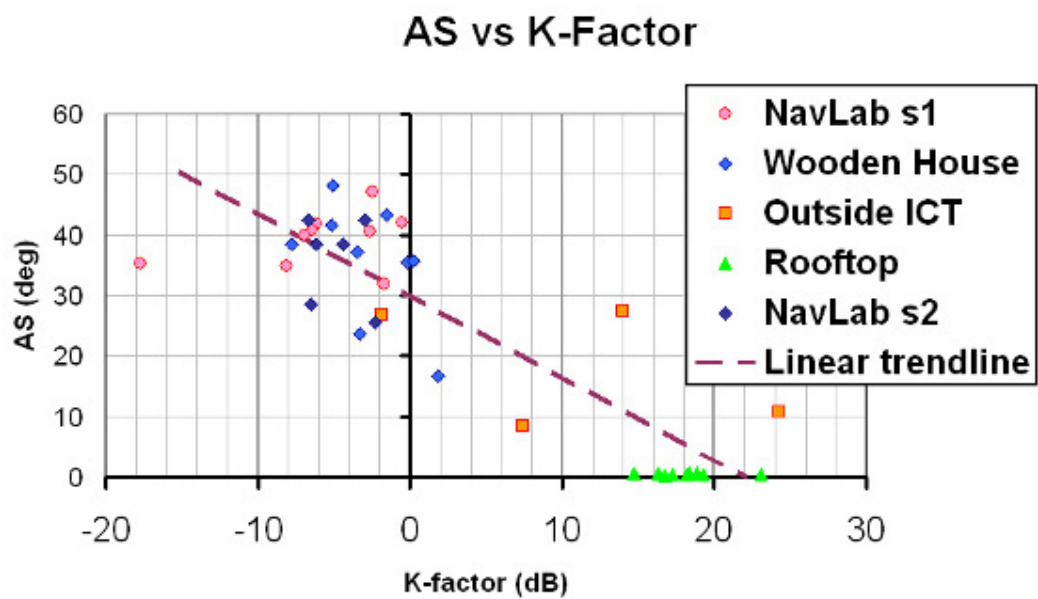


**Figure 5-46: Angular spread vs K-factor, All data sets**

**Chapter Six: Conclusions and Recommendations**

The main goal of this research was to characterize the effects of multipath fading on GNSS signals. Different effects on several signal properties were considered and finally, the results of measuring these effects on the GNSS channel were presented. Another goal was to assess the performance of synthetic array systems as an example of trajectory aided methods to boost the performance of GNSS receivers and indoor wireless navigation. The output of this research can be used to enhance the design of GNSS hardware such as antennas to accommodate multipath, and can be used in context aware receivers to alter signal acquisition and tracking strategies optimally under fading. This chapter summarizes the findings of this research and discusses the connection between the aforementioned effects.

## 6.1 Conclusions

### 6.1.1 Effect of phase wrap-up

The theoretical development of the received phase for the case of rotating antennas showed that this effect solely depends on the rotation rate of the antenna. Therefore, the higher rotation speeds result in more array performance degradation. Further simulation-based analyses showed that the array gain and AoA estimation accuracy drop considerably when this effect is not accounted for. Moreover, the practical measurements confirmed the theoretical findings and simulation results.

In addition, it was shown that this method gives accurate results when used to correct collected data that are contaminated with phase wrap-up. The observations

showed that after correcting for this effect, the array gain reaches its nominal value and the beamscan algorithm gives accurate results.

### 6.1.2 Effect of antenna pattern

As stated before, the antenna pattern has an important effect on the overall estimated AoA distribution through the changes in the peak to side-lobe ratio of the array gain pattern. It must be noted that in the context of this research, to preserve the effect of environment and distinguish it from the effect of antenna gain pattern itself, the use of antenna with an isotropic gain pattern is preferred. Unfortunately, such antenna for GNSS frequency band was not at hand and therefore to investigate this issue through the experimental part of this research, two different antenna elements, namely a NovAtel GPS 701/702 GGL series and a Ublox M-335c antenna were used. In the simulation-based analysis a hypothetical isotropic antenna was also considered.

The simulation analysis was based on two different conditions. Firstly, a mid-elevation LoS signal that was contaminated with several multipath interference from low to high elevation angles was used. In this case, the isotropic antenna yielded the most accurate results and both the NovAtel and Ublox antennas demonstrated the same result with slightly different distributions. The other simulation case considered a high-elevation angle LoS component along with several other lower elevation antennas. In this case, the NovAtel antenna outperformed the other two because of its higher gain at higher elevation angles.

In a wooden house, the Ublox antenna performed more accurately because the signals were more or less arriving from all directions. On the other hand, for the case of

the NavLab, the NovAtel antenna performed better, since the walls' attenuation was found to be generally higher than that of the ceiling.

### 6.1.3 AoA distribution, AS, AG and K-factor

Based on the surrounding environment, it was observed that the angular spread or standard deviation of AoA distribution along the elevation reached up to $30^o$. In the azimuth direction, the AS reached over $130^o$. In other words, in harsh multipath conditions 63% of the signal comes from a span of $260^o$ along the azimuth and $60^o$ along the elevation. Also, in the majority of cases, the wider AS along the azimuth is associated with a wider elevation spread. However, especially in mild multipath conditions, this is not necessarily true and in a few cases AS along the elevation is larger than along the azimuth.

Also, it was observed that there is a close relationship between the fading intensity, angular spread and array gain. A novel parameter to unify the AS along both directions was introduced as an AS criteria, the difference between the achieved array gain and the theoretical array gain was considered as the array gain performance measure and, finally, the K-factor of the Rician fit to the signal amplitude distribution was chosen as the fading channel intensity.

The results showed that these parameters are tightly linked to each other and in wide AS cases, typically smaller K-factors are measured and lower array gains are achieved. The measurements showed that the K-factor varies from more than +20 dB to less than -20 dB and array gain degradation reaches up to 4 dB. The values pertaining to

worst case scenarios are bound with angular spreads of about $60^o$ (AS as defined in Equation (5-4)).

The most important observation of this research was that in indoor environments the signal of satellites located at higher elevation angles typically had the smallest AS and highest K-factors and, therefore, resulted in the highest array gains. The results of a data collection scenario that was designed to test this hypothesis demonstrated this and also showed that in the NavLab, although the signals coming from the window have sometimes acceptable features, the signal penetration through the ceiling is favourable to GNSS navigation. It must be noted this arises from several reasons. The first is that the signal of the higher elevation satellites has undergone less path loss and therefore has higher levels inherently. Another reason is that these signals are amplified by the antenna itself due to higher gain of the antenna at higher elevation angles. The third reason is the signal reflections from these satellites are generally coming from very low or even negative elevation angles and therefore are filtered out by the hemispherical pattern of that the GNSS antennas. These reasons add up to the particular conditions of NavLab that make high-elevation satellites reliable sources of signal for indoor positioning at this location.

### 6.1.4 Signal Level and Correlation Coefficient

Broumandan et al (2011a) showed that the performance of processing gain under multipath is saturated due to channel coherence time and distance limitations. Therefore, the characterization of $C / N_0$ is beneficial to measure the level cross rate and average fade duration (Satyarayana et al 2010) as the second order statistics of the channel to choose the optimal coherent integration time. Also, signal level fluctuations under

multipath completely comply with correlation coefficient spatial variations. In narrow-AS situations, signals spatially decorrelate slowly and the $C/N_0$ levels are high and stable, whereas in wide-AS correlation coefficient and signal level plots show effects of deep fading. In addition, it was observed that the data sets with higher correlation coefficients result in higher array gains and as the fading dominance on the channel increases, the signals spatially decorrelate more rapidly. To sum up, it was observed that the mean achieved array gain in a data set follows the signal level and K-factor trends.

## 6.2 Future Work

1.      It was shown that the satellites located at higher elevation angles have better signal qualities, including narrower angular spreads and higher SNRs. Therefore, the signals coming from such satellites are reliable sources of positioning, provided the satellite geometry remains acceptable. In the scenarios for this research, two GPS satellites provided such signal qualities almost at the same time. Therefore, in the future, by applying the same methodology to the signals of other constellations such as GLONASS, one may improve indoor GNSS based navigation considerably.  Now that GLONASS satellites are available, this should be tested with real data.

2.      To reach this ultimate goal under harsh conditions, GNSS receiver antennas with higher gains at higher elevation angles can provide receivers with higher SNR signals, free of low elevation multipath interference. However, in milder areas, signals coming from mid elevation angles should also increase the positioning

accuracy. This should also be tested with appropriate antennas and under various environments.

3.      Many current receiver architectures are designed for open sky conditions and use satellites' elevation angles to weight their observations. An additional component could be added to estimate the K-factor in order to alter the receiver strategy under multipath conditions. Such information could be used in tuning acquisition search space and bandwidth of different loops within the receiver architecture to accommodate the increased angular and Doppler spread of the signal.

4.      In this research, the circular motion of an antenna was adopted to develop a spatial diversity system to increase the GPS SNR indoors. However, at each snapshot, the array manifold vector can be modified to combine the position information into a beamforming and coherent integration process over any arbitrary trajectory by knowing the precise position of the antenna phase center. This position or position variation can be predefined or can be measured with IMU or other sensors or signals. Also, one may prefer to use gyroscope measurements to compensate for phase wrap-up over any arbitrary and uncertain motion. This issue can be considered an innovative topic for future research for GNSS based navigation to achieve even higher accuracies.

# References

Allen, B. and M. Ghavami (2005) *Adaptive Array Systems*, John Wiley & Sons.

Akgull, F.O. and K.Pahlavan (2010), "A Novel Statistical AoA Model Pertinent to Indoor Geolocation", *Journal of Geographic Information Systems*, 2010, 2 45-48, doi:10.4236/jgis.2010.21009 Published Online January.

Andersen, J.B. and K.I.Pedersen (2002), "Angle of Arrival statistics for Low Resolution Antennas", IEEE Transactions on Antennas and Propagation, VOL. 50, NO. 3, March.

Beyerle, G. (2009), "Carrier Phase Wind-Up in GPS reflectrometry" GPS Solutions, 13, 3, 191-198.

Bisnath, S., Petovelo, M., Lachapelle, G. (2007), "What is carrier phase wind-up? What is its effect on GNSS performance / operation?" *Inside GNSS*, 2(5): 32-35.

Blaunstein, N., and J. B. Andersen (2002) "Multipath Phenomena in Cellular Networks" Artech House, ISBN 1-58053-185-7

Braasch M.S. (2001) "Performance Comparison of Multipath Mitigating Receiver Architectures" in *PROC. of IEEE Aerospace Conference*.

Broumandan, A., T. Lin, A.R.A. Moghaddam, D. Lu, J. Nielsen and G. Lachapelle (2007) "Direction of Arrival Estimation of GNSS Signals Based on Synthetic Antenna Array". *in Proceedings of ION GNSS07* (Forth Worth, 25-28 Sep, Session C2), The Institute of Navigation, 11 pages.

Broumandan, A., J. Nielsen, G. Lachapelle, (2008) "Practical results of high resolution AoA estimation by the synthetic Array" ", *Proc. of IEEE VTC08 Fall Conference,* Calgary, 22-25 Sep. 2008.

Broumandan, A (2009) "Enhanced Narrowband Signal Detection and Estimation with a Synthetic Antenna Array for Location Applications". *PhD Thesis, University of Calgary, Department of Geomatics Engineering, September 2009, UCGE report No.: 20292.*

Broumandan, A., J. Nielsen and G. Lachapelle (2011a) Indoor GNSS Signal Acquisition Performance Using A Synthetic Antenna Array. IEEE Transactions on Aerospace and Electronic Systems, 47, 2, 1337-1350.

Broumandan, A, J.Nielsen, and G. Lachapelle (2011b) "Coherent Integration Time Limit of a Mobile Receiver for Indoor GNSS Applications". *GPS Solutions*, DOI: 10.1007/s10291-011-0215-y.

El-Sheimy, Naser, Haiying Hou, Xiaoji Niu (2008) "Analysis and Modeling of Inertial Sensors Using Allan Variance", *IEEE Transactions on Instrumentation and Measurement, VOL. 57, NO. 1*, January 2008.

Friedlander, B., and S. Scherzer (2004) "Beamforming Versus Transmit Diversity in the Downlink of a Cellular Communications Systems," *IEEE Transaction on Vehicular Technology*, vol.53, no. 4, pp. 1023-1034.

Flenniken, W., Wall, J., Bevly, D.M., "Characterization of Various IMU Error Sources and the Effect on Navigation Performance," *Proceedings of the 2005 ION GNSS*, Long Beach, CA, September 13-16, 2005.

Ganesh, R., K. Pahlavan. (1993), "Statistics of short time and spatial variations measured in wideband indoor radio channels" *IEE proceedings –H, 140(4):297-302*, August 1993.

Gazzah, H., S. Marcos, (2006), "Cramer-Rao bounds for antenna array design", *IEEE transactions on signal processing, VOL. 54, NO. 1, January 2006.*

Jong, Y. L., and M. Herben (1999) "High-resolution Angle of Arrival Measurement of the Mobile Radio Channel," *IEEE Transaction on Antennas Propagations, vol.47, no.11, pp.1677-1687*, November 1999.

Jong, Y. L. C. (2001) "Measurement and Modeling of Radio wave Propagation in Urban Microcells", *PhD Thesis*, Department of Electrical Engineering, University of Technology (EUT), Netherlands.

Kaplan, E. D., C. Hegarty. (2006), *Understanding GPS Principles and Applications*, 2nd ed., Artech House.

Kazemi, P., C. O'Driscoll, G. Lachapelle (2009) "Digital Phase Locked Loop with Frequency Rate FeedBack" *Proc. of ION GNSS 2009,* Savannah, GA, 22-25 September 2009 , 8 pages.

Kazemi, P., C. O'Driscoll, (2008) "Comparison of Assisted and Stand-Alone Methods for Increasing Coherent Integration Time for Weak GNSS Signal Tracking" *Proc. of ION GNSS 2008,* Savannah, GA, 16-19 September 2008 , 11 pages.

Kim , D., L. Serrano and R.B.Langley, (2005) "Compensation of the Effects of Phase Wind-Up for Improving the Performance of GPS-RTK based Vehicle Navigation System*", Proceedings of ION GNSS 08, International Technical Meeting*, 13-16 September, Long Beach, CA.

Klukas, R., O. Julien, L. Dong, M. E. Cannon, and G. Lachapelle (2004) "Effects of Building Materials of UHF Ranging Signals," *GPS Solutions*, Vol. 8, No. 1, pp. 1-8, Springer Verlag, April 2004

Kraus, John D., (1988) "Antennas", 2nd Edition, McGraw Hill.

Lin, T., Boroumandan A., Nielsen, J., O'Driscoll, C., Lachapelle, G., (2009), "Robust Beamforming for GNSS Synthetic Arrays", *Proceedings of ION GNSS 2009*, 22-25 Sep. 2009, Savannah, GA.

Lachapelle, G. (2009), ENGO – 625, Advanced GNSS Theory and Applications, Lecture Notes, Department of Geomatics Engineering, University of Calgary, Fall 2009.

Ma, Changlin (2003) "Integration of GPS and Cellular Networks to Improve Wireless Location Performance" *Proc. of ION GPS/GNSS conference 2003*, Portland, OR, 9-12 September 2003.

Misra P., and P.Enge (2006), "Global Positioning System, Signals, Measurements and Performance" 2nd Edition, Ganga-Jamuna Press, MA.

O'Driscoll, C., A. Izadpanah and G. Lachapelle (2007) "Investigation of the Effect of Antenna Orientation on Indoor GPS Signal Reception" *Proceedings of NAV07 Conference,* Royal Institute of Navigation, London, 30Oct-1Nov, 12 pages.

O'Driscoll, C. and D.Borio (2009) "ENGO.638 – GNSS Receiver Design" Lecture Notes Department of Geomatics Engineering, University of Calgary, Summer 2009.

O'Driscoll, C., D. Borio, M.G. Petovello, T. Williams and G. Lachapelle (2009) "The Soft Approach: A Recipe for a Multi-System, Multi-Frequency GNSS Receiver", *Inside GNSS Magazine, Volume 4, Number 5, pp. 46-51*. (http://www.insidegnss.com/node/1635)

Pany, T., B. Eissfeller (2008) "Demonstration of Synthetic Phased Array Antenna for Carrier/Code Multipath Mitigation". *Proceedings of ION GNSS08*

Papoulis, A., S. U. Pillai (2002), Probability, Random Variables and Stochastic Processes, McGraw-Hill, Fourth edition

Parsons, J. D. (2000) *The Mobile Radio Propagation Channel*, John Wiley & Sons LTD, 2nd ed.

Rappaport, T. S. (2002) "Wireless Communications: Principles and Practice" Prentice Hall PTR, 2nd Edition

Renaudin, Valeri, M. H. Afzal, G. Lachapelle (2010) "New method for magnetometers based orientation estimation"*, Proc. of IEEE/ION PLANS 2010 conference,*4-6 May 2010, Palm Springs, CA.

Roy, R., and T. Kailath (1989) "ESPRIT- Estimation of Signal Parameters Via Rotational Invariance Techniques," *IEEE Transaction on Acoustics, Speech and Signal Processing,* vol.37, no. 7, pp 984-995.

Sadrieh, Seyed Nima, Ali Broumandan and Gerard Lachapelle (2010) "Spatial/Temporal Characterization of the GNSS Multipath Fading Channel" *Proc. of ION GNSS 2010*, Portland OR, 21-24 September 2010.

Saleh A. M. and R. A. Valenzuela (1987), "A statistical model for indoor multipath propagation" *IEEE J. on selected areas of Communication, SAC-5:128-13, February 1987*.

Satyanarayana, S., D. Borio and G. Lachapelle (2010) "Power Levels and Second Order Statistics for Indoor Fading Using a Calibrated A-GPS Software Receiver". *Proceedings of GNSS10* (Portland, OR, 21-24 Sep, Session E1), The Institute of Navigation

Schmidt, R. (1986) "Multiple Emitter Location and Signal Parameter Estimation," *IEEE Transactions on Antennas and Propagation*, vol. AP-34, no.3

Sieskul B. T.,F. Zheng, Thomas Kaiser (2009) "On the effect of shadow fading on the wireless geolocation in the mixed LoS/NLoS environments" *IEEE Transactions on signal processing*, VOL. 57, NO. 11, NOV 2009.

Soloviev, A., F. van Graas, S. Gunawardena, M. Miller (2009) "Synthetic Aperture GPS Signal Processing: Concept and Feasibility Demonstration". *Procedings of ITM09.*

Spencer, Q. (1996) "Modeling the Statistical Time and Angle of Arrival Characteristics of Indoor Multipath Channel", *PhD Thesis, Brigham Young University, February 1996.*

Spencer, Q. (2000) "Modeling the Statistical Time and Angle of Arrival Characteristics of Indoor Multipath Channel" *IEEE J. on selected areas of Communication, VOL 18, No. 3, March 2000.*

Tang, Y. and H. Sobol, (1995) "Measurement of PCS microwave propagation in buildings*" J. of Applied Microwave & Wireless, pp 38-60, Winter 1995*

Tetewsky, A.K, and F.E. Mullen (1997), "Carrier Phase Wrap-Up induced by Rotating GPS Antenna" *GPS World*, 8(2), 51-57.

Todd, S. R., M. S. El-Tannany, S. A. Mahmoud, (1992) "space and frequency diversity measurement of the 1.7 GHz indoor radio channel using a four branch receiver", *IEEE Transactions on Vehicular Technology, 41(3): 312-320, August 1992.*

Turin G. L. et al, (1972) "A statistical model of urban multipath propagation" *IEEE transactions on vehicular technology*, VT-21(1):1-9, February 1972.

Van Dierendonck, A.J., P. Fenton, and T.Ford, (1992) "Theory and Performance of Narrow Correlator Spacing in a GPS Receiver", *Navigation, Journal of Institute of Navigation,* Vol. 39, No. 3, Fall 1992.

Van Trees H. L. (2002), "*Optimum Array Processing*; Detection*, Estimation, and Modulation Theory"*, part IV. John Wiley & Sons, Inc., New York.

Ventura-Travest, J. and Didier Flament, (2006) "EGNOS – A corner stone of Galileo", ESA publications, Noordwjik, Netherlands, 2006.

Ward, P. W., J.W. Betz and C.J. Hegarty (2006a) "GPS Satellite Signal Characteristics" [Chapter 4] in *Understanding GPS, Principles and Applications*, 2nd ed, Kaplan E.D., C.J. Hegarty, Artech House, 2006.

Ward, P. W., J.W. Betz and C.J. Hegarty (2006b) "Satellite Signal Acquisition, Tracking and Data Demodulation" [Chapter 5] in *Understanding GPS, Principles and Applications*, 2$^{nd}$ ed, Kaplan E.D., C.J. Hegarty, Artech House, 2006.

Wong, Carl, Richard Klukas and Geoffrey Messier, (2008) "Using WLAN infrastructure for Angle-of-Arrival indoor user location", *Proc. of IEEE VTC08 Fall Conference,* Calgary, 22-25 Sep. 2008.

Wu, J.T., S.C. Wu, G.A. Hajj, W.I. Bertiger, S.M. Lichten, (1993), "Effect of Antenna Orientation on GPS Carrier Phase", *Manuscripta Geodaetica*, 18:91-98.

Yang Y. and J.A. Farrel, (2003) "Magnetometer and differential carrier-phase GPS aided INS for advanced vehicle control", *IEEE Transactions on Robotics and Automation, VOL. 19:2, pp 269-282*, 8 April 2003.

Yong, S.K. and J.S. Thompson (2005), "Three-Dimensional Spatial Fading Correlation Models for Compact MIMO Receivers*", IEEE Transactions on Wireless Communications*, VOL 4, NO. 6, November.

Zhou, J., K. Ishizawa, S. Sasaki, S, Muramatso, H. Kikuchi, and Y. Onozato (2004), "Generalized Spatial Correlation Equations for Antenna Arrays in Wireless

Diversity Deception: Exact and Approximate Analysis" *IEICE Transactions on Communications*, VOL.E87-B, No.1, January.


Zoltowski M. D. and Mathews C. P. (1993), "Closed-Form 2D Angle Estimation with Uniform Circular Arrays via Phase Mode Excitation and ESPIRIT", *proc. Of IEEE conference on signals, systems and computers*, pp 726-730, vol.1.

## APPENDIX A: CARRIER PHASE WRAP-UP FOR SYNTHETIC UCA

To analyze the effect of carrier phase wrap-up on a synthetic Uniform Circular Array (UCA), firstly, the corresponding geometry must be analyzed that is shown in Figure A-1.

If the antenna is fixed to the rotating lever arm, the vector $\overrightarrow{OA}$ and the angle $\gamma$ change by time, thus affecting the heading of the antenna and satellite-receiver distance simultaneously. The geometry of $\Delta OAS$ triangle is the key to solve this problem; thus denoting the instantaneous corresponding lengths as

$$\overline{OA} = R, \qquad \overline{OS} = \rho, \qquad \overline{AS} = r.$$ 

<div align="right">(A-1)</div>

where $\overline{AS} = r$ changes due to rotations of $\overrightarrow{OA}$. To build the necessary foundation for formulating phase wrap-up when a translational motion is also added to the antenna rotation, Equation (4-3) is revisited. In Equation (4-3), the received phase at the receive antenna due to antenna orientation and the distance between satellite and the receive is described as

$$\Omega = \omega_c t - \left(\phi - \gamma\right) - \kappa r.$$

<div align="right">(A-2)</div>

As mentioned in previous section, the carrier phase shift due to change in the antenna orientation has a linear trend proportional to the rotation rate and described by

$$\gamma(t) = \dot{\gamma} t + \gamma_0.$$

<div align="right">(A-3)</div>

where $\gamma_0$ can be ignored without loss of generality. To consider the phase change due to instantaneous change in $r$, the following vectorial identity

$$\overrightarrow{AS} = \overrightarrow{OA} - \overrightarrow{OS} \Rightarrow r = \sqrt{R^2 + \rho^2 - 2R\rho \cos\alpha}.$$

<div align="right">(A-4)</div>

can be used where $\alpha$ is shown in

**Figure** A-1. $\alpha$ is found from

$$\alpha = \cos^{-1}\left(\widehat{OA} \cdot \widehat{OS}\right) \tag{A-5}$$

where $\widehat{OA}$, $\widehat{OS}$ are unit vectors along antenna position and the satellite position and can

be found from

$$\widehat{OA} = \begin{pmatrix} \cos\gamma & \sin\gamma & 0 \end{pmatrix}$$
$$\widehat{OS} = \begin{pmatrix} \cos\tilde{\theta}\cos\phi & \cos\tilde{\theta}\sin\phi & \sin\tilde{\theta} \end{pmatrix}. \tag{A-6}$$

Therefore

$$\cos\alpha = \cos\tilde{\theta}\cos(\phi - \gamma) \tag{A-7}$$

and

$$r^2 = R^2 + \rho^2 - 2R\rho\cos\tilde{\theta}\cos(\phi - \gamma). \tag{A-8}$$
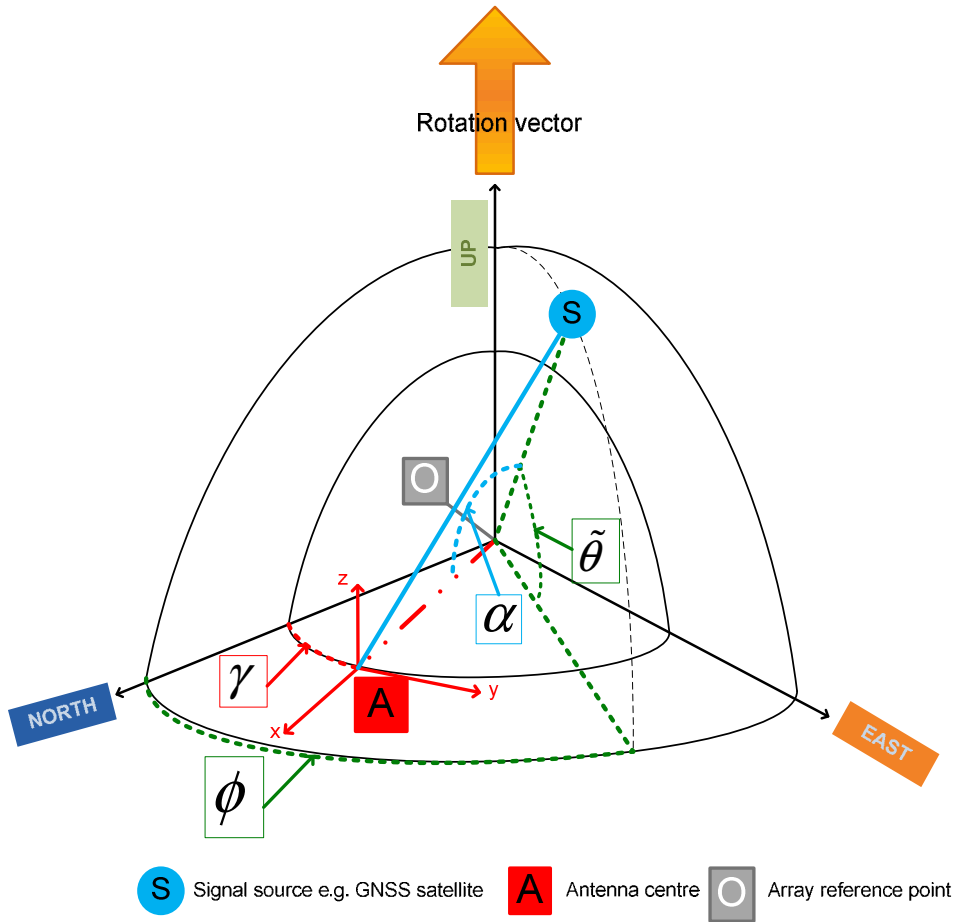
Figure A-1: Scheme of circular synthetic array phase wrap-up

If Equation (A-8) is differentiated with respect to time

$$2r\frac{dr}{dt} = \frac{d}{dt}R^2 + \frac{d}{dt}\rho^2 - \frac{d}{dt}\left(2R\rho\cos\tilde{\theta}\cos(\phi-\gamma)\right)$$

$$= 2R\rho\cos\tilde{\theta}\left(-\frac{d}{dt}\cos(\phi-\gamma)\right) \tag{A-9}$$

where the second line is derived assuming that $\tilde{\theta}$ and the distance between the satellite and the array reference point are constant. Also the radius of the synthetic array does not change with time. Now since the only time dependent term in Equation (A-9) is $\gamma(t) = \dot{\gamma}t$. Replacing $\gamma$ and simplifying Equation (A-9) results in

$$\frac{dr}{dt} = -2\frac{\rho}{2r}R\dot{\gamma}\cos\tilde{\theta}\sin(\phi-\dot{\gamma}\bullet t). \tag{A-10}$$

Also since the satellite is far away from the earth and $R$ is very small comparing to other distances, $\rho$ and $R$ can be considered equal and hence

$$\frac{dr}{dt} = -R\dot{\gamma}\cos\tilde{\theta}\sin(\phi - \dot{\gamma} \cdot t).$$

(A-11)

Therefore by replacing the output of Equation (A-11) and (A-3) into Equation (A-2) the received phase can be modified to

$$
\begin{aligned}
\Omega &= \omega_c t - (\phi - \gamma) - \kappa r \\
&= \omega_c t - (\phi - \dot{\gamma}(t).t) - \kappa r(t) \\
&= \omega_c t - (\phi - \dot{\gamma}(t).t) - \kappa(\bar{r} + \dot{r}(t).t) \\
&= \omega_c t - \phi - \kappa\bar{r} + t\left[\dot{\gamma}(t) + \kappa R\dot{\gamma}(t)\cos\tilde{\theta}\sin(\phi - \dot{r}(t).t)\right]
\end{aligned}
$$

(A-12)

where $\dot{\gamma} \cdot t + \kappa R\dot{\gamma}\cos\tilde{\theta}\sin(\phi - \dot{\gamma} \cdot t)$ represents the apparent shift in the received frequency of an antenna fixed on a rotating lever arm. The other two terms $\phi$ and $\kappa\bar{r}$ are constant terms due to initial heading misalignment between the antenna and the satellite, and the mean distance between the satellite and the mobile antenna.

**APPENDIX B: C/N$_0$ PLOTS, NAVLAB**
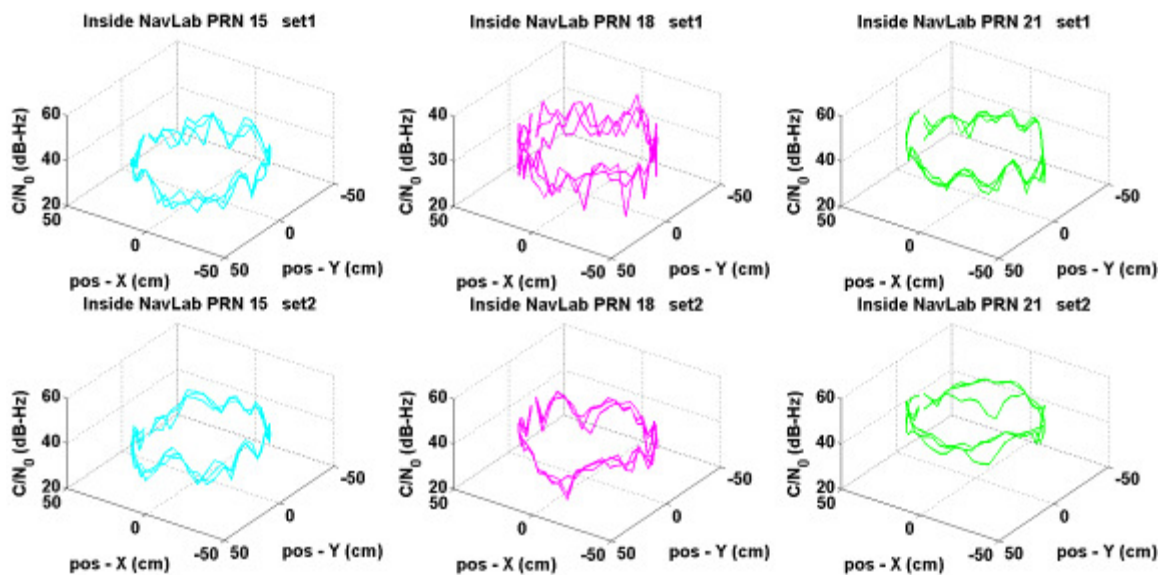


**Figure B-1:** $C / N_0$ **plots, sets 1 and 2, PRN 15, PRN 18 and PRN 21, NavLab**
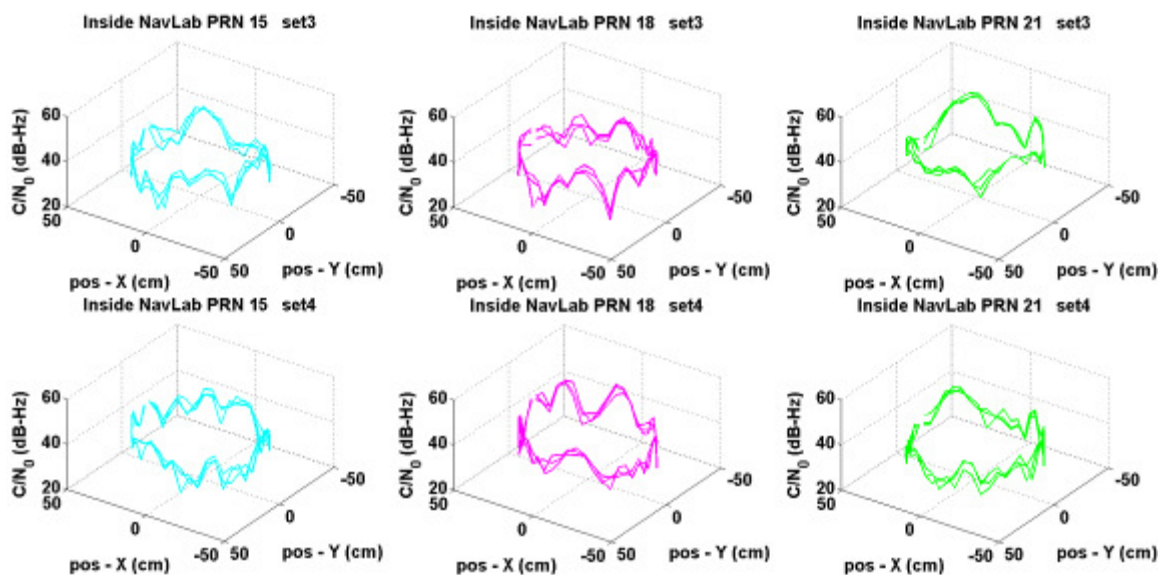


**Figure B-2:** $C / N_0$ **plots, sets 3 and 4, PRN 15, PRN 18 and PRN 21, NavLab**
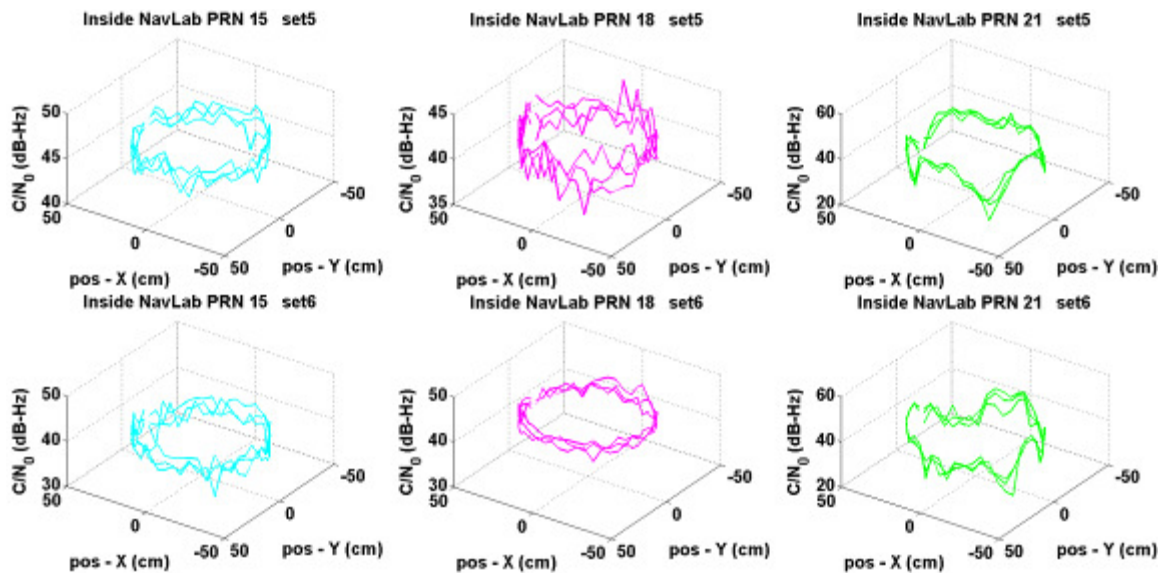
**Figure B-2:** $C / N_0$ **plots, sets 5 and 6, PRN 15, PRN 18 and PRN 21, NavLab**
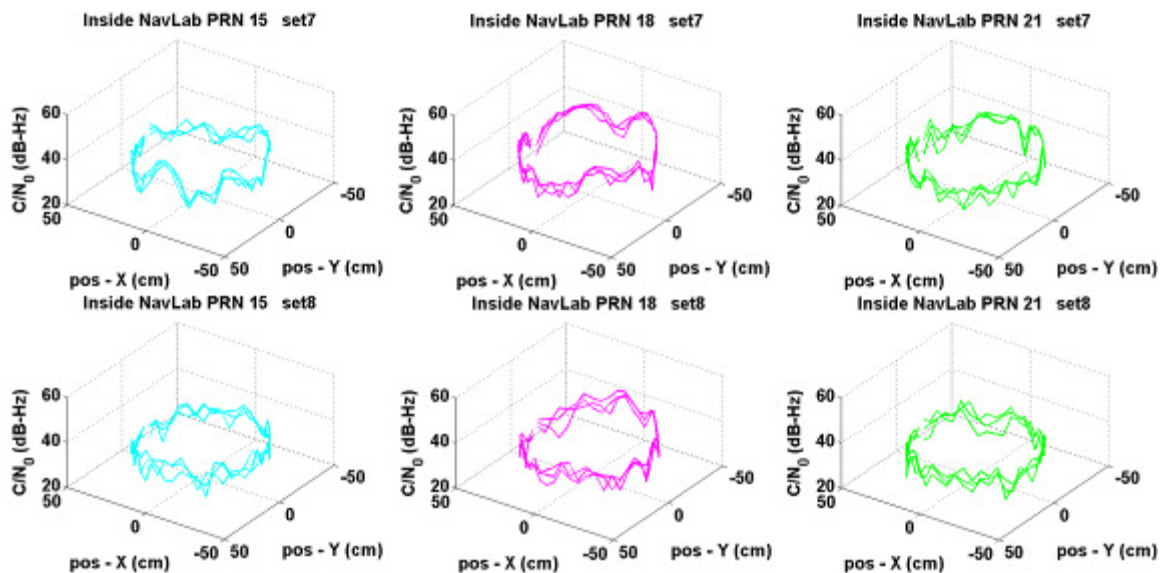


**Figure B-2:** $C / N_0$ **plots, sets 7 and 8, PRN 15, PRN 18 and PRN 21, NavLab**